Chemo-Mechanical Modeling of Polymeric Hydrogels

Von der Fakultät für Maschinenbau
der Gottfried Wilhelm Leibniz Universität Hannover

zur Erlangung des akademischen Grades
Doktor-Ingenieur

genehmigte Dissertation
von

M. Sc. Aidin Hajikhani

2021

Herausgeber:
Prof. Dr.-Ing. habil. Dr. h.c. mult. Dr.-Ing. E. h Peter Wriggers

Verwaltung:
Institut für Kontinuumsmechanik
Gottfried Wilhelm Leibniz Universität Hannover
An der Universität 1
30823 Garbsen

Tel: +49 511 762 2220
Fax: +49 511 762 5496
Web: www.ikm.uni-hannover.de

ISBN 978-3-941302-40-2

1. Referent: Prof. Dr.-Ing. habil. Dr. h.c. mult. Dr.-Ing. E. h Peter Wriggers
2. Referent: Prof. Dr.-Ing. Michele Marino

Tag der Promotion: 26.03.2021

To my family

Zusammenfassung

Hydrogele bestehen aus einem wassergequollenen und selbsttragenden Polymernetzwerk. Sie können extrem großen Verformungen standhalten, ihre mechanischen Eigenschaften können fein abgestimmt werden, und sie ermöglichen die Diffusion und Freisetzung von Molekülen. Daher haben Hydrogele in einer Vielzahl von technischen Bereichen Anwendung gefunden, insbesondere, aber nicht ausschließlich, im biomedizinischen Bereich. Hydrogele werden durch die Einwirkung äußerer Mittel mechanisch stabilisiert, welche durch Quervernetzung im Polymernetzwerk als Folge von Transport- und Reaktionsmechanismen induziert werden. Aufgrund seiner einzigartigen Eigenschaften als Hydrogel ist Natriumalginat ein Substrat mit großem Potenzial, nicht nur in der regenerativen Medizin, sondern auch in vielen verschiedenen aufstrebenden Technologiebereichen wie Bioprinting, Drug-Delivery und Mikrofluidik. Die Vernetzung erhöht die Steifigkeit des Hydrogels, führt zu unelastischen Verformungen im Polymernetzwerk und interagiert mit der Quellfähigkeit der Konstrukte. Die Beherrschung dieses Prozesses ist entscheidend für die Erfüllung von Funktionskriterien in den genannten Technologiefeldern. In dieser Hinsicht kann die Entwicklung neuer Berechnungsmodelle in diesem Bereich den Weg zu neuen Untersuchungswerkzeugen öffnen, die experimentelle Planung fördern und die Abhängigkeit von Trial-and-Error-Tests verringern.

Die vorliegende Forschungsarbeit entwickelt ein Reaktions-Diffusions-Modell, das die Abhängigkeit der Diffusionseigenschaften vom Gelierungsgrad berücksichtigt. Dazu wird die Vernetzungskinetik für die chemische Gelierung von Natriumalginat-Hydrogelen über die Calciumchlorid ($CaCl_2$)-Diffusion analysiert und mit experimentellen Messungen verglichen, was zum Nachweis einer vernetzungsabhängigen Diffusivität führt. Außerdem verändert das Vernetzungsmittel die mechanischen Eigenschaften des Hydrogels. Aus diesem Grund wird in dieser Studie ein thermodynamisch konsistentes chemo-mechanisches Modell für große Verformungen vorgeschlagen, das poroelastische und reaktiv-diffusive Mechanismen koppelt, die während der Vernetzung in Alginathydrogelen auftreten. Das System berücksichtigt Schrumpfungs- und Schwellungseffekte, Flüssigkeitsbewegungen sowie die Reaktionskinetik der Calcium-induzierten Quervernetzung. Darüber hinaus wirken sich, auf der Basis thermodynamischer Überlegungen, innere Spannungen direkt auf die Vernetzungskinetik aus, was eine wechselseitige Kopplung zwischen Mechanik und Chemie offenbart.

Das Modell ist in einem Finite-Elemente-Framework implementiert und berücksichtigt eine monolithische Kopplung zwischen dem chemischen Transport und der Mechanik. Der rechnerische Ansatz ermöglicht die Charakterisierung der (experimentell nicht zugänglichen) heterogenen Verteilung der chemo-mechanische Größen und Eigenschaften im Hydrogel. Es werden verschiedenste numerische Tests vorgestellt, um das Verhalten von Hydrogelen zu untersuchen und die numerischen Ergebnisse mit den verfügbaren experimentellen Daten zu vergleichen.

Schlagwörter: Chemo-mechanische Modellierung, Hydrogele, Poroelastische Effekte, Vernetzungskinetik, Finite-Elemente-Simulationen, Reaktions-Diffusion, Finite Dehnung

Abstract

Hydrogels consist in a water-swollen and self-supporting polymeric network. They can undergo extremely large deformations, their mechanical properties can be tuned finely, and they permit the diffusion and release of molecules. Therefore, hydrogels have found applicability in a wide range of technical applications, especially but not exclusively in the biomedical field. Hydrogels are mechanically stabilized through external agents' action, which induces the formation of crosslinks in the polymer network as a consequence of transport and reactive mechanisms. Due to its unique properties, Sodium alginate is a substrate with great potential as a hydrogel, not only in regenerative medicine but also in many different emerging technological fields like bioprinting, drug-delivery, and microfluidics. Crosslinking increases the hydrogel's stiffness results in inelastic deformations in the polymer network and interacts with constructs' swelling capacity. Controlling this process is crucial for fulfilling functional criteria in several mentioned technological fields. In this regard, the development of new computational models in the field can open the way to novel tools of investigation, boost experimental design, and lessens trial-and-error tests.

This work develops a reaction-diffusion model, accounting for the dependence of diffusive properties on the gelation degree. To this aim, the crosslinking kinetics for the chemical gelation of sodium alginate hydrogels via calcium chloride ($CaCl_2$) diffusion is analyzed and compared with experimental measurements, which results in evidence of crosslink dependent diffusivity. Besides, the crosslinking agent alters mechanical properties in the hydrogel. For this reason, this study proposes a thermodynamically consistent chemo-mechanical model in large deformation coupling poroelastic and reactive-diffusive mechanisms occurring during crosslinking in alginate hydrogels. The system accounts for shrinking and swelling effects, fluid movements, as well as the reaction kinetics of calcium-induced crosslinking. Based on thermodynamic considerations, internal stresses directly affect the crosslinking kinetics, revealing a two-way coupling between mechanics and chemistry.

The model is implemented in a finite element framework, considering a monolithic coupling between chemical transport and mechanics. The computational framework allows characterizing the (experimentally inaccessible) heterogeneous distribution of chemo-mechanical quantities and hydrogel properties. Several numerical tests are presented to investigate hydrogels' behavior and compare numerical outcomes with available experimental evidence.

Keywords: Chemo-mechanical modeling, Hydrogels, Poroelastic effects, Crosslinking kinetics, Finite element simulations, Reaction-diffusion, Finite strain

Contents

1 Introduction **1**
- 1.1 Hydrogel . . . 1
- 1.2 Applications . . . 2
  - 1.2.1 Three-dimensional (3D) bioprinting technology . . . 2
  - 1.2.2 Drug delivery and microfluidics . . . 4
- 1.3 Alginate hydrogels . . . 6
- 1.4 Chemo-mechanical challenges and available models . . . 11
- 1.5 Scope of study . . . 14

2 Mathematical and experimental modeling of hydrogel crosslinking **17**
- 2.1 Experimental tests . . . 17
  - 2.1.1 Hydrogel preparation . . . 17
  - 2.1.2 Experimental set-up . . . 18
- 2.2 Theoretical and computational model . . . 18
  - 2.2.1 Diffusion . . . 20
  - 2.2.2 Chemical reaction . . . 20
  - 2.2.3 Computational strategy . . . 20
- 2.3 Experimental results and model validation . . . 23
- 2.4 Crosslinking effects . . . 24
- 2.5 Parametric study . . . 25
- 2.6 Discussions . . . 26

3 Continuum multi-physics theory **31**
- 3.1 Chemical model . . . 32
- 3.2 Chemo-mechanical kinematical effects . . . 35
- 3.3 Balance of linear and angular momentum . . . 37
- 3.4 Material (mole) balance . . . 37
- 3.5 Second law of thermodynamics . . . 37
- 3.6 Constitutive model . . . 38
- 3.7 Free-Energy definition . . . 40
- 3.8 Resulting chemo-mechanical thermodynamic quantities . . . 42
- 3.9 Reference configuration: as-prepared state . . . 44

4 Numerical treatment **49**
4.1 Spatial discretization 49
4.1.1 Isoparametric mapping 49
4.1.2 Three-dimensional shape function 53
4.2 Temporal discretization 53
4.2.1 First-order finite difference method 54
4.3 Multi-physics computational implementation 54
4.3.1 Backward Euler scheme 55
4.3.2 Local residual 56
4.3.3 Global residual and tangent matrix 57

5 Simulations and results **61**
5.1 Initialization and boundary conditions 61
5.2 Free-swelling of cubic hydrogel 63
5.2.1 Convergence study 65
5.2.2 Chemo-mechanical hydrogel behaviour 66
5.2.3 Effect of external bath composition 68
5.2.4 Parametric analysis 68
5.2.5 Crosslinking kinetics 71
5.2.6 Inelastic rearrangement of the polymer network 75
5.2.7 Effect of mechanical actions 77
5.3 Buckling of hydrogel tubes 82
5.3.1 Impact of calcium chloride $CaCl_2$ solution on buckling 82
5.4 Wrinkling of cuboid 86
5.4.1 Influence of $CaCl_2$ solution on wrinkling 86
5.5 Bending of a polymeric bilayer bar 91
5.5.1 $CaCl_2$ effect on the bending of the bilayer bar 91
5.6 Spherical gel confined swelling 95
5.6.1 Constrained chemo-mechanical effect 95

6 Conclusions and outlook **101**

Bibliography **106**

Chapter 1

Introduction

1.1 Hydrogel

Hydrogels have received great attention in the past 50 years because of their promising role in a wide range of applications such as the food industry and drug delivery, and recently bioprinting (PEPPAS ET AL., 2006; SLAUGHTER ET AL., 2009). A Hydrogel is a colloidal gel where water is the dispersed medium, consisting of polymer networks (e.g., Sodium Alginate) extensively swollen with fluid content (e.g., Phosphate-buffered saline (PBS), water) (PEPPAS ET AL., 2006).

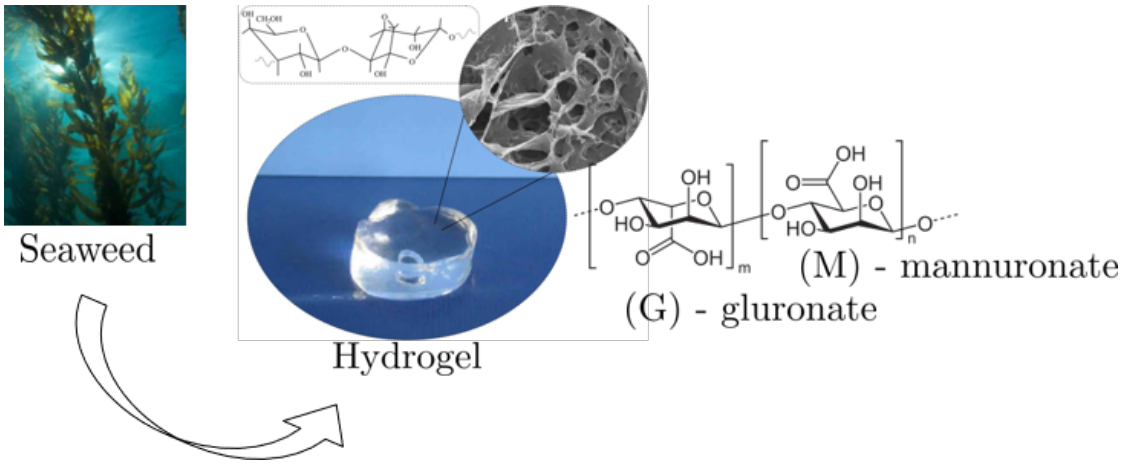

Figure 1.1: SEM image of the cross-sections of a linear copolymer hydrogel (i.e. Sodium Alginate) with homopolymeric blocks of gluronate and mannuronate (CHANG ET AL., 2010; BRACCINI & PÉREZ, 2001).

Scientists have determined hydrogels in several different ways by describing them as a water-swollen and crosslinked polymeric network created by one or more monomers' simple reactions. Further, it is a polymeric material that displays the ability to swell and retain a substantial portion of water within its formation but will not dissolve in water. Hydrogels have received considerable attention in the past 50 years due to their exceptional promise in a wide range of applications (BUCHHOLZ & GRAHAM, 1998; LI ET AL., 2013). They

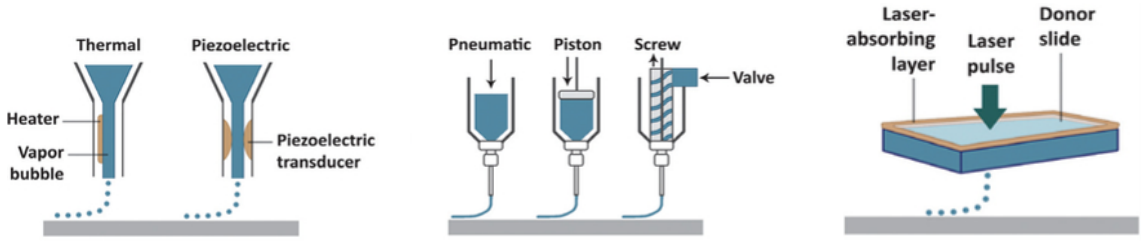

(a) (b) (c)

Figure 1.2: (a) Inkjet bioprinter;(b) Extrusion-based bioprinter; (c) Laser-assisted bioprinter (MURPHY & ATALA, 2014).

also possess a degree of flexibility very similar to natural tissue because of their large water content.
The hydrogels' capacity to absorb water arises from hydrophilic functional groups attached to the polymeric firmness, while their resistance to dissolution emerges from crosslinks between network chains. Numerous materials, including naturally occurring and synthetic, tailor the definition of hydrogels.

1.2 Applications

This section reports a brief overview of the hydrogels' applications in recent emerging technology such as three-dimensional (3D) printing technology, drug delivery, and microfluidics. Moreover, the correlated physical phenomena during bioprinting with the most applicable bioink will be discussed by considering the crosslinking/gelation process's complexity during the bioprinting procedure.

1.2.1 Three-dimensional (3D) bioprinting technology

Additive manufacturing, also known as three-dimensional (3D) printing, creates many pioneering inventions in various fields, such as engineering, manufacturing, and medicine. 3D printing of biocompatible materials, cells, and 3D functional living tissues are enabled due to the recent developments (MURPHY & ATALA, 2014). Compared to conventional non-biological printing, 3D bioprinting technology addresses more complexities, such as the cell types, choice of materials, and technical challenges related to the regenerated tissues and organs' sensitivities. It is required to integrate the technologies from different engineering fields, biomedical science, and cell biology to confront these complexities. 3D bioprinting is being used for regenerating transplantable tissues and organs, such as cornea, bone, multilayered skin, vascular grafts, tracheal splints, and heart tissue. 3D bioprinting technology gives the capability to precisely fabricate 3D structures and has enhanced the quality of the complex reconstructed tissues and organs with high reproducibility thanks to the automated printing procedure (MURPHY & ATALA, 2014). The ultimate 3D bioprinted compositions such as biological materials, biochemicals and living cells are accurately positioned layer-by-layer with pre-programmed structures, geometries and spatial control of locating the func-

tional components. Meanwhile, one of the main challenges is to synchronize the bioink crosslinking rate with the resolution of the 3D bioprinted structure (ZHANG ET AL., 2016, 2017; GUNGOR-OZKERIM ET AL., 2018). Notwithstanding the fact that additive biomanufacturing is in its early progression phases, its adaptability has continued to expand the applications in tissue engineering (ATALA & YOO, 2015). The major 3D bioprinting techniques (see Fig. 1.2) can be categorized as: inkjet bioprinting/droplet bioprinting, extrusion-based bioprinting, and laser-assisted bioprinting (LaBP) (KHALIL & SUN, 2009; WÜST ET AL., 2011; DABABNEH & OZBOLAT, 2014; WANG ET AL., 2015).

A computer-aided design/computer-aided manufacturing (CAD/CAM) system is required in the mentioned methods for programming and consequently fabricating the 3D structures. The crosslinked bioinks (Fig. 1.3) during or immediately after the bioprinting plays a vital role in all of these various bioprinting techniques. The crosslinking behavior in the bioinks is essentially influencing the shape or the mechanical stability of the final intended reconstructed tissue or organ. Currently, many different natural and synthetic biomaterials with specific characteristics have been used as bioink. Meanwhile, defining the optimal cell-laden bioink formulation for successful bioprinting is highly demanded (LEE ET AL., 2016).

The hydrogel is stabilized using post-printing chemical treatments, generally referred to as gelation processes (WILLIAMS ET AL., 2018; ZHANG ET AL., 2015b) to confer suitable mechanical properties to the printed construct. Among different techniques, chemical gelation promotes G-blocks' formation thanks to the diffusion of reactive ions through the gel. Calcium chloride ($CaCl_2$) is one of the most used alginate crosslinking agents since it allows for a rapid and straightforward gelation thanks to the release of Ca^{2+} cations.

At the same time, crosslinking via $CaCl_2$ is not a controlled process due to its high solubility in aqueous solutions (COLOSI ET AL., 2016; LEE & MOONEY, 2012; TALEI FRANZESI ET AL., 2006). The crosslinking degree highly depends on alginate and $CaCl_2$ concentration. It is a critical factor for controlling hydrogel uniformity and strength: a faster gelation rate is better for cell encapsulation, while a slower gelation rate produces more uniform structures with higher mechanical properties (REZENDE ET AL., 2009; LEE ET AL., 2018; KUO & MA, 2001). Moreover, crosslinking processes alter the polymeric network's topology, obstructing diffusive processes (COLOSI ET AL., 2016; POTTER ET AL., 1994; SALAHSHOOR & RAHBAR, 2014). Therefore, the fidelity and effectiveness of bioprinting strategies highly depend on coupled effects given by the interplay of crosslinking mechanisms and diffusive processes (COLOSI ET AL., 2016; LEE & YEONG, 2016; TALEI FRANZESI ET AL., 2006).

Bioprinting protocols and post-printing treatments might be optimized using computer-assisted strategies for virtual testing and design (AZNAR ET AL., 2016; GUNGOR-OZKERIM ET AL., 2018). To this aim, a reliable computational model, adequately validated and calibrated through feasible experimental strategies, would support the development of novel *in silico* tools (CARLIER ET AL., 2016). A highly reliable bioink should contain appropriate physico-chemical properties such as chemical, mechanical, and biological features (LEE ET AL., 2015). The selected bioink should be capable of reconstructing the tissue with adequate mechanical stability and robustness as well as high shape fidelity. Furthermore, 3D-bioprinted materials are being applied in the research fields to benefit from drug delivery, tissue engineering, toxicology, microfluidics, and artificial muscles (JEONG ET AL., 1997; GALAEV & MATTIASSON, 1999; BEEBE ET AL., 2000; QIU & PARK, 2001; DRURY &

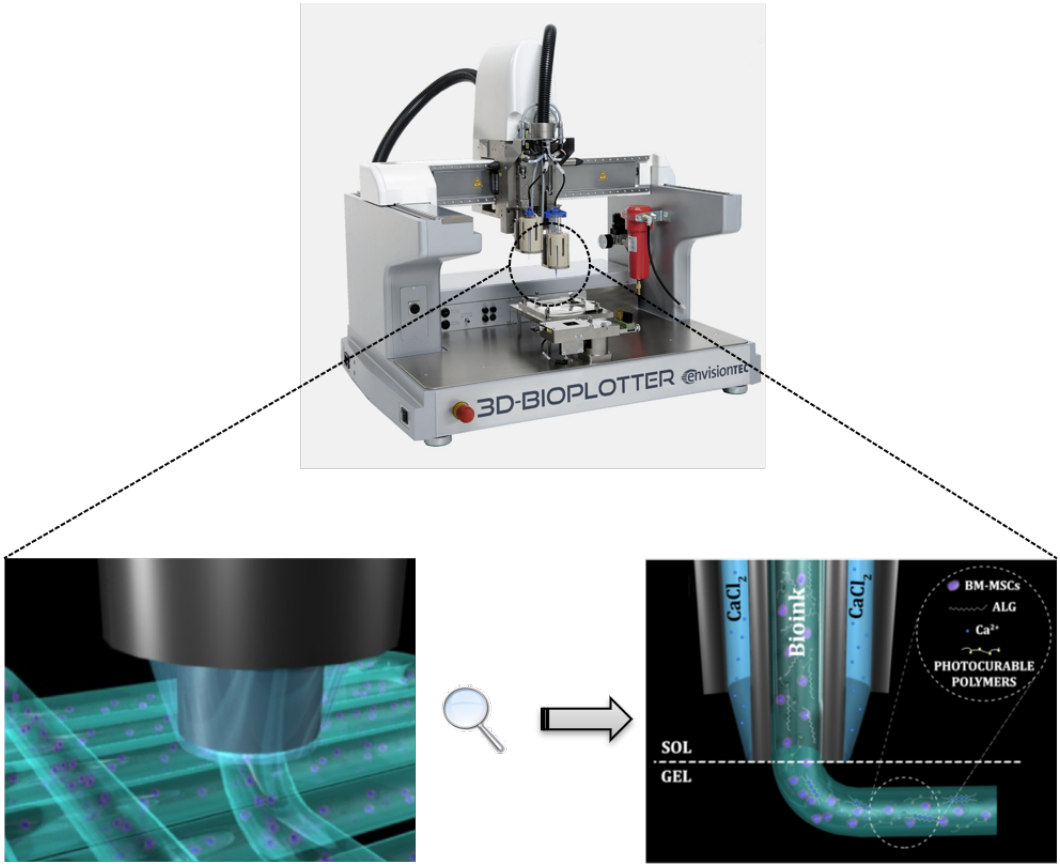

Figure 1.3: 3D representation of sodium alginate hydrogel immersed into calcium chloride via coaxial nozzle on the printing head (COSTANTINI ET AL., 2016).

MOONEY, 2003; SUCIU ET AL., 2004; PEPPAS ET AL., 2006; JAGUR-GRODZINSKI, 2006; TOKAREV ET AL., 2009; ABIDIAN & MARTIN, 2009; LEE ET AL., 2010; ZHANG ET AL., 2020).

1.2.2 Drug delivery and microfluidics

Besides, hydrogels can be employed as a drug transport application (See Fig. 1.5), where the encapsulated drug particles between the hydrogel polymer chains in an initial or unswollen state are released directly at the targeted organ or tissue when the hydrogel starts swelling (PAL ET AL., 2009). Moreover, VOO ET AL. (2016) have conducted research on the calcium alginate hydrogel beads, that presents assuring encapsulation transporter of drugs utilized in controlled delivery applications. Several experiments have been conducted by LEE ET AL. (2012) on demonstrating the controlled pattern transformation of microstructured tubular gels utilizing swelling-induced circumferential buckling (See Fig. 1.7). Particularly, LEE ET AL. (2012) have focused on tubular structure with circumferential wrinkles, which conveys crucial physiological significance in biomedical engineerings such as the wrinkled airway of an asthmatic bronchiole caused by the swollen inner cell layer to understand better the behavior of diseased cells and their influence on the physiological circumstances (JAMES

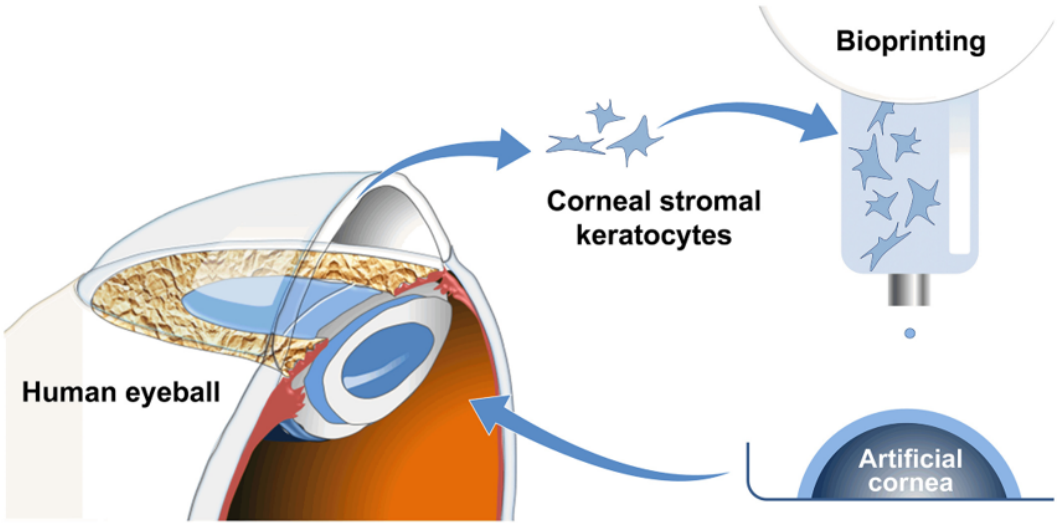

Figure 1.4: Schematic of the 3D bioprinting and biomimetic of the 3D corneal model using hydrogels and cultivated human corneal stromal keratocytes (DUARTE CAMPOS ET AL., 2019).

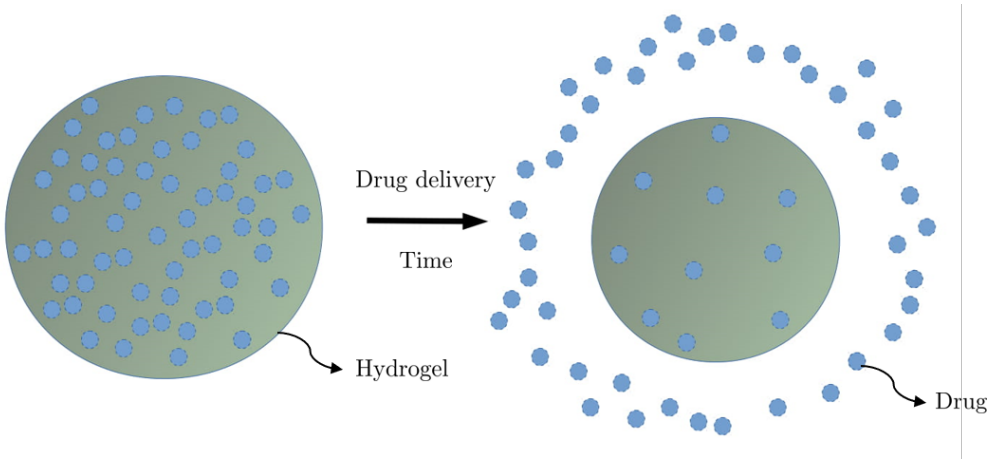

Figure 1.5: Controlled drug delivery from the hydrogel droplet by the swelling mechanism throughout the time.

ET AL., 1989; REDINGTON & HOWARTH, 1997). The kinetics aspects of the hydrogel phase transition are difficult to understand during the swelling process, which results in mechanical instability and wrinkling patterns. TANAKA ET AL. (1987) have illuminated the physical fundamentals causing the formation and evolution of the mentioned pattern. Swelling kinetics of constraint bending gels have been characterized by using an optical microscope to characterize the properties of gel films (YOON ET AL., 2010). Hydrogels have also been used for microfluidics applications (See Fig. 1.8), where swelling/de-swelling of hydrogel pillars by solvent's PH is controlling the channels in two ways, including (a) with two outflows and (b) stopping the middle outflow (BEEBE ET AL., 2000).

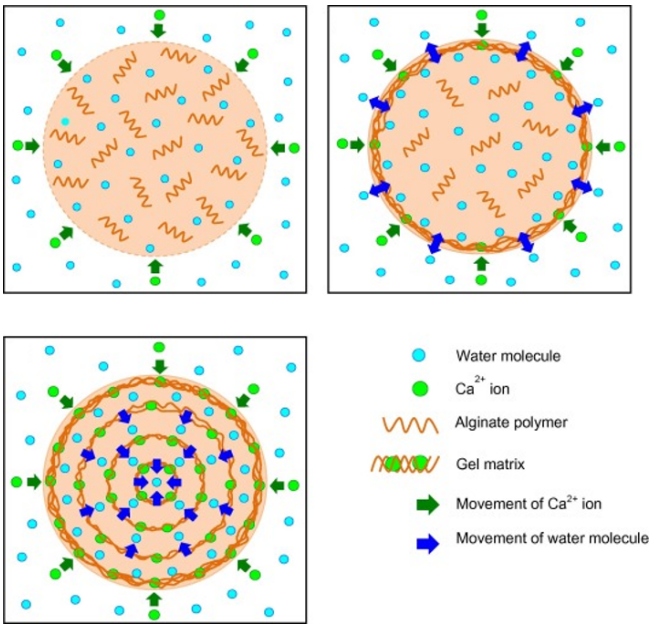

Figure 1.6: Multi-layer evolution of calcium-alginate hydrogel in calcium alginate beads for controlled drug and food delivery applications (VOO ET AL., 2016).

1.3 Alginate hydrogels

Alginate is an anionic copolymer composed of mannuronic (M) blocks and guluronic acid (G) blocks (e.g., see Fig. 1.1). Only the alginate's G-blocks engage in the intermolecular crosslinking with divalent or trivalent cations, e.g., Ca^{2+}, forming intersections in which calcium ions are placed. Such binding zones between the G-blocks are referred to as "egg-boxes" (REZENDE ET AL., 2009). Usually, sodium alginate is combined with copolymers, e.g., gelatin, to improve both printability and cell viability (DUAN ET AL., 2013). Hence, the permanent bonds obtained from the chemical crosslinking process will provide better mechanical properties and fidelity compared to the reversible physical crosslinking, making the hydrogel a suitable platform for various biomedical applications. Alginic acid or alginate is a natural anionic polysaccharide purified from brown seaweed and can be observed in the native ECM of the human body. Alginate is utilized in bioengineering and biomedicine due to its biocompatibility, low cytotoxicity, mild crosslinking or gelation process, and low-cost (LEE & MOONEY, 2012; ZHANG ET AL., 2015a). Particularly, alginate as a bioink has been extensively used due to its prompt crosslinking characteristic with harmless byproducts under physiological conditions (YAN ET AL., 2012; JIA ET AL., 2014). The crosslinking of alginate, also known as gelation, can be induced by divalent cations such as Ca^{2+}, in which eggbox structures are formed, enabling polymer networks to create a physical gelation and solidification (DE QUEIROZ ET AL., 2006; MØRCH ET AL., 2012). There are several alginate-based bioinks, such as alginate alone or alginate mixed with other biomaterials, mostly used in bioprinting due to its fast gelation, which results in good printability (YU ET AL., 2013). Alginate is a linear polysaccharide copolymer (See in Fig. 1.9) accommodating the two (1→4)-linked monosaccharides α-L-monossaccharides

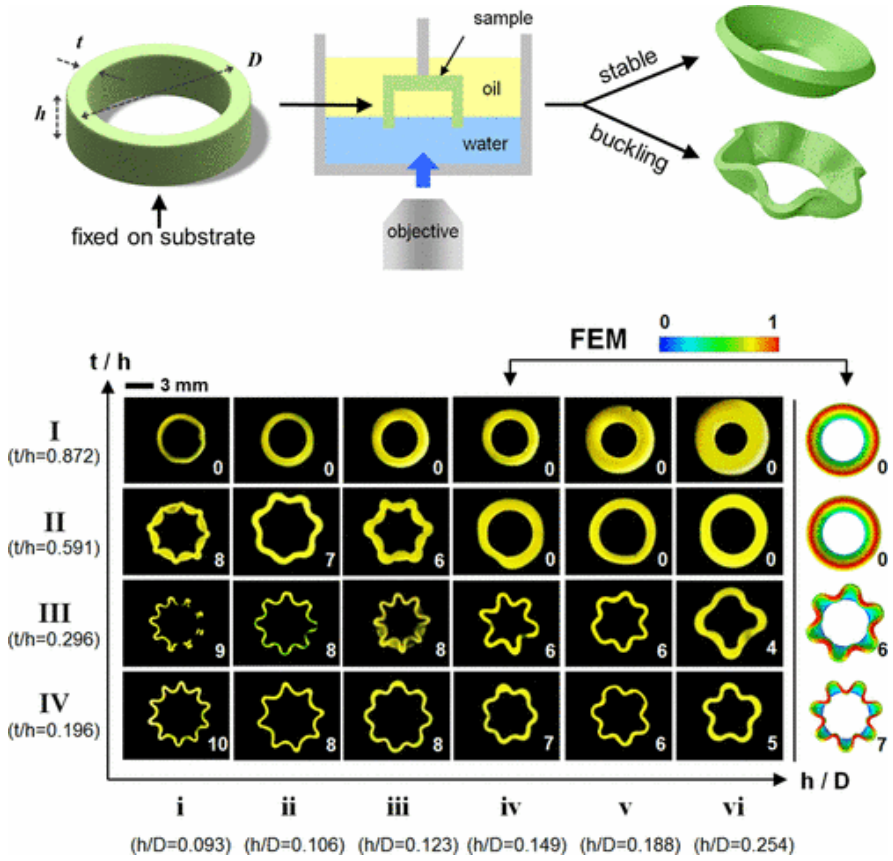

Figure 1.7: Circumferential buckling of gel tube with the various pattern formations and characteristic dimensions of tubular gel with its experimental setup (LEE ET AL., 2012).

(G) and β-L-mannuronic acid (M) (SMIDSROD ET AL., 1972; MIKKELSEN & ELGSAETER, 1995). The monomers are categorized into three different types of blocks (See Fig. 1.10): M blocks, G blocks, and MG blocks, where the relative content of M, G, and MG blocks lean on the harvested alginate source from the seaweed. Furthermore, the alginate's physical, chemical, biological and immunological characteristics are associated with the relative content of M, G, and MG blocks. The most well-known commercial alginate is a worm-like chain with a Kuhn length of about 34 nm at I $\approx$ 0.1 M an ionic strength (SMIDSRØD & HAUG, 1968). The stiffness of the alginate molecule in a solution with a pH higher than about five will be significantly increased when the ionic strength is decreased due to the polyelectrolytic nature of alginate (SMIDSRØD & HAUG, 1971). Calcium ions (i.e., Ca^{2+}) as divalent cations strengthen the G-blocks binding by salt bridges and pairwise alignment of the involved G-blocks (See Fig.1.11). Since the quantity of alginate concentration is above a certain minimum value, the Ca^{2+} conciliated binding of G blocks enhance the formation of extended alginate networks where the G blocks form stiff junctions. The division of alginate, including M and MG blocks, are not involved in network intersection formation and are semi-flexible (See Fig.1.11). Alginate-Ca^{2+} gels composing of alginate molecules abounding in G-blocks are generally quite hard and relatively brittle. While alginate-Ca^{2+} gels comprising alginate with a high relative content of M and MG blocks are more elastic

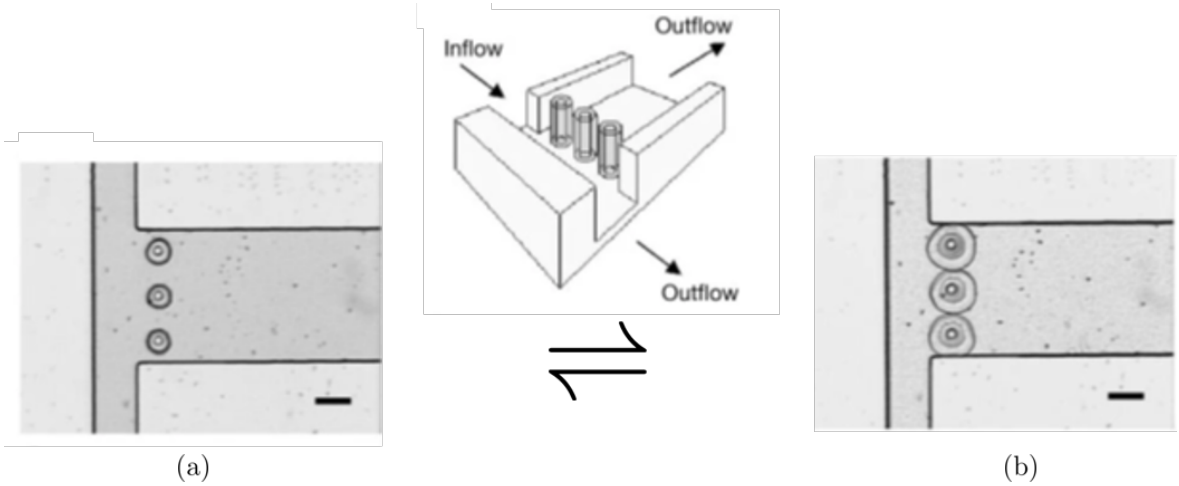

Figure 1.8: Controlling the outflow in microfluidic channels (BEEBE ET AL., 2000).

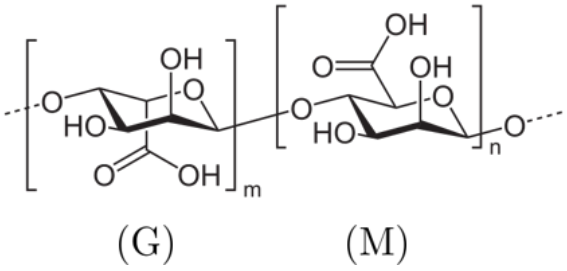

Figure 1.9: The two monosaccharide inside the alginate are α-L-guluronic (G) and β-D-mannuronic acid (M) (MIKKELSEN & ELGSAETER, 1995).

and can undergo much larger respective deformations. Alginate-Ca^{2+} gels can particularity be considered as non-equilibrium gels since the inceptive contact between two G blocks has been made; hence one Ca^{2+} salt bridge has been formed, and the residue of the G block through a combined effect rapidly positions to form a dimer structure frequently allude to as an eggbox structure, including 3 to 15 Ca^{2+} ions (SMIDSROD, 1972; SKJÁK-BRÆK ET AL., 1986; OTTERLEI ET AL., 1991; ANTHONSEN ET AL., 1993). The eggbox structure does not necessarily associate with the energetically most stable configuration; however, because of its high activation energy of recommencing, the structure is kinetically confined, and the initial binding can generally be considered irreversible (SMIDSROD, 1972). The gel point for the sol-gel transition relies on both the alginate and the calcium ion (i.e., Ca^{2+}) concentrations. The higher the alginate concentration, the lower the Ca^{2+} concentration is needed to reach the gel point (WANG ET AL., 1993). Moreover, the crosslinking duration supplies an indicator of the optimum time for gelation to complete and obtain the ultimate gel strength. Most early studies conducted on gelation mechanics of alginate have not satisfactory issued the effects of crosslinking duration on gel strength (DOUMECHE ET AL., 2004; AGARWAL ET AL., 2015; LOZANO-VAZQUEZ ET AL., 2015). Different gelation time influences on alginate gels' swelling performance by immersing the gels for different durations in $CaCl_2$ has been studied. As a result, the produced gels were shrunken with an increase of gelation

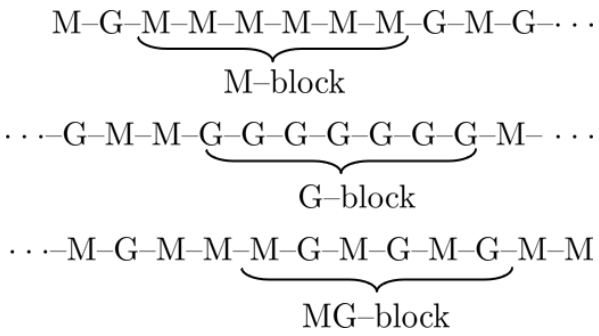

Figure 1.10: Schematic diagram of the principal monosaccharide block forms of alginate.

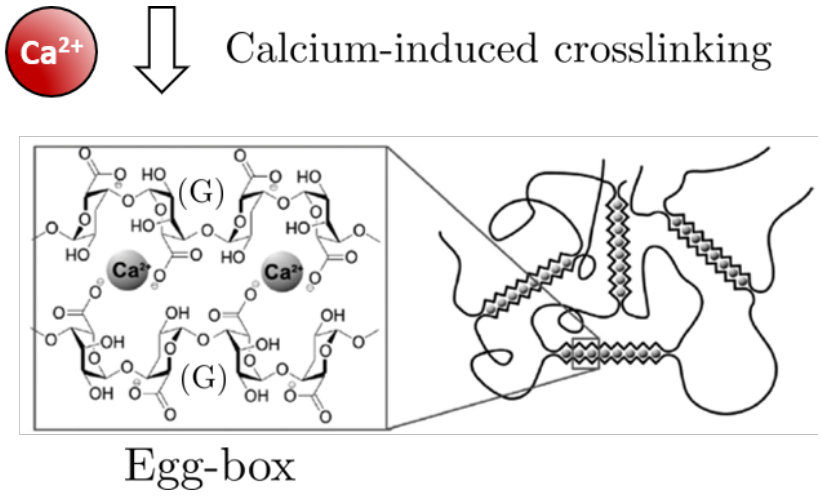

Figure 1.11: Schematic demonstration of the egg-box model for Ca^{2+} binding of G blocks.(MIKKELSEN & ELGSAETER, 1995)

time because of the increased degree of crosslinking between the calcium ions (i.e., Ca^{2+}) and alginate (SAARAI ET AL., 2013). Notwithstanding, the conducted research did not study gel deformation behavior and strength during the crosslinking process. Studies on alginate gels conducted on using excessive gelation solution ($CaCl_2$) vary from 2 times to 40 times more than the volume of alginate solution (GUPTA ET AL., 2010; BELLICH ET AL., 2011; LOZANO-VAZQUEZ ET AL., 2015). To the best of the author's knowledge, there has been no research study in detail about the formation of alginate gel on a limited amount of calcium ions. For that reason, conducting a comprehensive research study on the effect of the proportion of alginate and calcium ions on the gel property (See Figs.1.12 and 1.13) by varying the quantity (finite to surplus) of calcium ions is considered great significance (RAMDHAN ET AL., 2019). Further, the effect of various calcium chloride solutions on microstructures of sodium alginate is shown in Fig. 1.14 by ZHAO ET AL. (2019). In the course of the gelation process, sodium alginate with its negatively charged carboxylate groups (COO^-) interacts with cations (Ca^{2+}), causing the shrinkage of the gel because of their electrostatic attraction, in which the weight of the formed gel decreased due to the water extrusion from the gel networks syneresis (DASHEVSKY, 1998; MAI ET AL., 2013; RAMDHAN ET AL., 2019). Furthermore, as shown in Fig. 1.15, the change of weight ratio of alginate gel construct

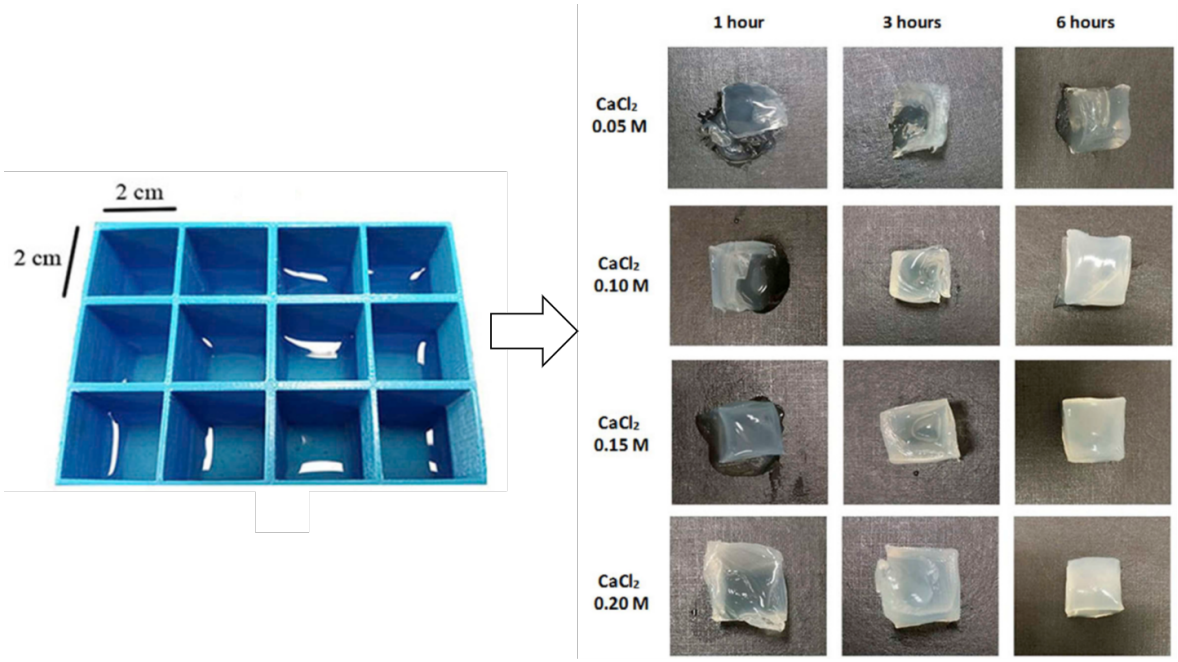

Figure 1.12: Alginate gel formation in a cuboid mold as a function of time (1–6 h) immersed in different $CaCl_2$ solutions, ranging from 0.05 M to 0.20 M (RAMDHAN ET AL., 2019).

during the crosslinking process is reduced as a consequence of the syneresis phenomenon, and afterward, the gel reached a steady weight VELINGS & MESTDAGH (1995); PUGUAN ET AL. (2014). One of the main challenges is understanding the syneresis phenomenon during the gelation process since it may decrease the efficacy of water-soluble constituents such as protein and water-soluble drugs (DASHEVSKY, 1998; MAI ET AL., 2013). In several bioengineering applications, comprehension of the gel's mechanical and structural properties plays an important role (GOMES ET AL., 2002; MARIJNISSEN ET AL., 2002; LAROBINA & CIPELLETTI, 2013). For example, a change in the gel's mechanical and swelling characteristics in tissue engineering applications can lead to intensified cartilage tissue properties(NUNAMAKER ET AL., 2007; KONG ET AL., 2004). Correspondingly, the release mechanism of drugs is a considerable amount of exerted influence on how the gel stress evolves during the pharmaceutical applications (GOMBOTZ & WEE, 1998). Alginate gels' mechanical behavior has been widely studied by MITCHELL & BLANSHARD (1974, 1976); LEE ET AL. (2000b) by considering their relevance for several applications. Alginate gels have different mechanical properties such as the shear modulus values in the range of 0.02–40 kPa (LEE ET AL., 2000a; ROWLEY & MOONEY, 2002) and stability because of a wide spectrum of ionic crosslinks, which are defined by alginate concentration, the ratio between G and M blocks, and the divalent ion concentration (LEROUX ET AL., 1999; STOKKE ET AL., 2000). Eventually, internal stress is created when the gel front in the alginate-Ca^{2+} during the crosslinking process is propagated (SECCHI ET AL., 2013).

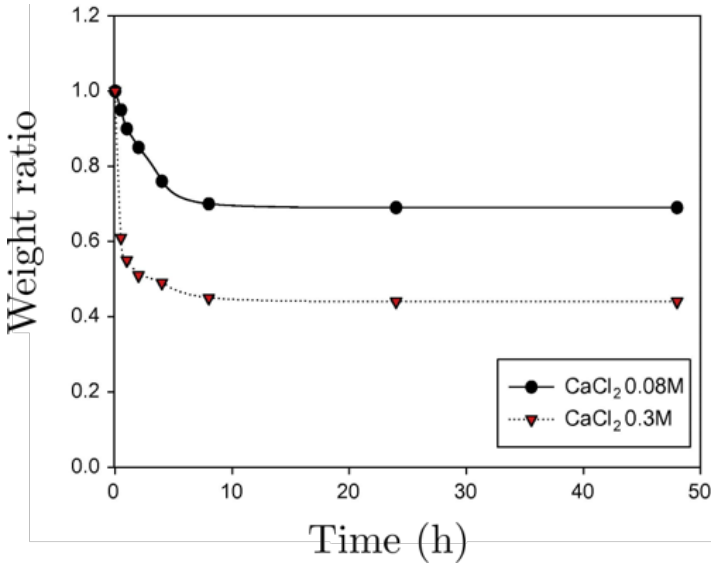

Figure 1.13: Syneresis of the formed gels with the ratio of alginate:$CaCl_2$ in 1:4 (RAMDHAN ET AL., 2019).

1.4 Chemo-mechanical challenges and available models

The design of hydrogel-based structures requires a deep understanding and precise control of chemo-mechanical mechanisms in the hydrogel. The focus of this work is on the coupling between mechanics and crosslinking reaction kinetics. First of all, crosslinking alters the topology of the polymer network, in turn affecting hydrogels' elasticity moduli and diffusivity properties, and thus crosslinker transport mechanisms and fluid-induced swelling (AMSDEN, 1998; CACOPARDO ET AL., 2019; COLOSI ET AL., 2016; DAVIDOVICH-PINHAS & BIANCO-PELED, 2010; HAJIKHANI ET AL., 2019; MAGNENET ET AL., 2012; NAGHIEH ET AL., 2018a; POTTER ET AL., 1994; SALAHSHOOR & RAHBAR, 2014; WU ET AL., 2009). Moreover, scientists have found a directly proportional relationship between the degree of crosslinking and reduced swelling capacities or even syneresis (i.e., shrinking of the hydrogel and exudation of the fluid content). This evidence demonstrates that crosslinking affects inelastic deformations of the polymer network (MARTINSEN ET AL., 1989; STOKKE ET AL., 2000; DRAGET ET AL., 2001; DAVIDOVICH-PINHAS & BIANCO-PELED, 2010; GÓMEZ, 2015; RAMDHAN ET AL., 2019). In this regards, a model for the curing of glassy polymer has been developed by SAIN ET AL. (2018) for estimating shrinking effects during the process, but other examples could not be found by authors. Moreover, it is well known that an external load alters the crosslinking reaction rate in polymers, and this evidence is used, for instance, for the industrial production of rubber (ANNABI ET AL., 2009; BELLANDER ET AL., 1998; MA ET AL., 2015; MAITRA & SHUKLA, 2014; TONPHENG & ANDERSSON, 2008). For instance, hydrostatic pressure accelerates the crosslinking reaction since it decreases the polymer chains' segmental mobility, preventing long-range motions of the polymer chains and promoting the formation of bonds between polymer chains and/or crosslinkers. This effect might play a significant role between gels since the coupling with swelling (i.e., fluid movements) induces highly heterogeneous local pressure fields. Compu-

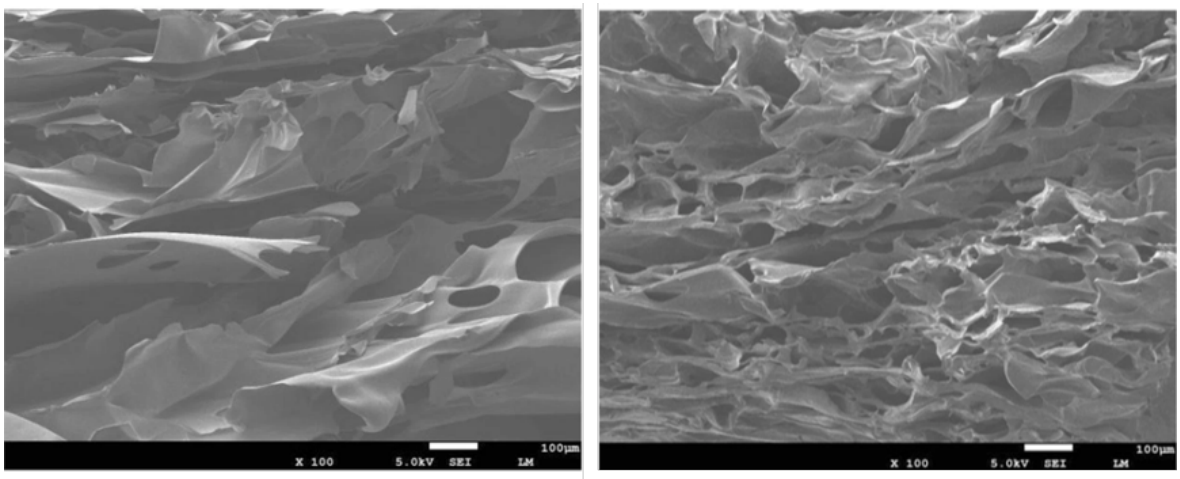

Figure 1.14: Microstructure of the sodium alginate prepared with different $CaCl_2$ concentrations: 0% (w/v) (a) 5% (w/v) (b) (ZHAO ET AL., 2019).

tational models are special tools for characterizing the heterogeneous distribution of chemo-mechanical quantities and properties in hydrogels. To date, the detailed measurement of these properties is experimentally unfeasible, but their distribution is essential for estimating the functionalities of constructs in advanced applications, such as smart drug delivery or bioprinting. Several authors have addressed the theoretical and computational modeling of hydrogels' chemo-mechanics since the past few decades, such as TANAKA & FILLMORE (1979); ZHAO & EICHINGER (1992); BOYCE & ARRUDA (2001); DOLBOW ET AL. (2004); LOEFFEL & ANAND (2011); CHESTER ET AL. (2015); ANAND (2017). Comparative computational strategies have been utilized to model the diffusion-driven swelling/growth of soft tissues. For instance, see HIMPEL ET AL. (2005); CYRON & HUMPHREY (2017); SOLEIMANI (2019). An accurate and robust computational model can assist the experimentalists in obtaining a better understanding of geometrical, mechanical and chemical effects, and in optimizing process variables for meeting design criteria during the production of hydrogel-based constructs.

Most studies on alginate gels mainly covered problems, including chemical aspects (biocompatibility, biodegradability). Meanwhile, the literature engaging with alginate gels' mechanical behavior seems not to cover coupling aspects (OERTHER ET AL., 1999; DRURY ET AL., 2004; WANG ET AL., 2015; MORESI & BRUNO, 2007). In recent years, much research has been conducted to model the equilibrium state of swelling hydrogels. In polymeric hydrogels, concurrent processes are occurring, including deformation of the solvent's network and transport. Polymeric gels are competent for large deformations that require a nonlinear theory to analyze the phenomenon. Since the small solvent molecules can freely enter or leave the gel (solution) and the long polymer chains are unable to leave the gel, consequently, the solvent will diffuse across the chains until the solution creates a pressure known as the pore pressure. In the work of CHESTER & ANAND (2011), a mean normal pressure term is defined, which is correlated to the fluid chemical potential, but this term can be elaborated

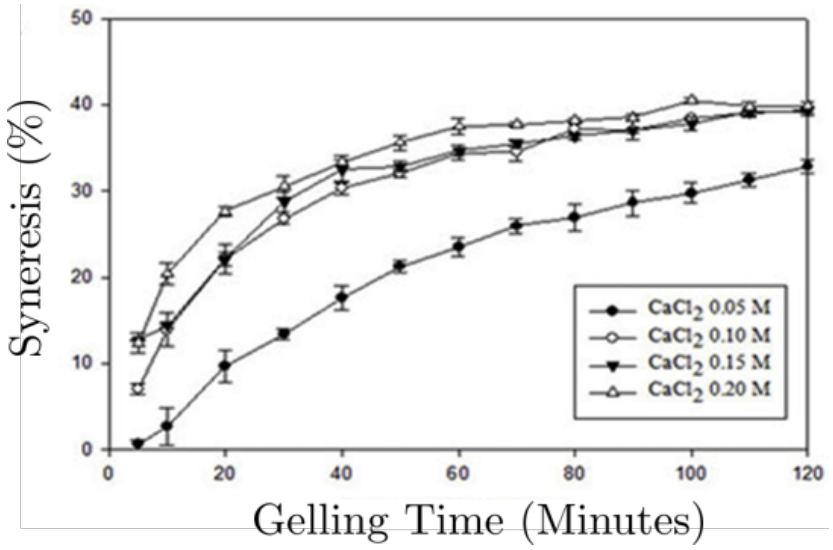

Figure 1.15: Syneresis of the formed gels immersed in 0.08 M and 0.3 M $CaCl_2$ solutions (PUGUAN ET AL., 2014).

by considering the coupled effects of the chemical reaction and the fluid chemical potential for the polymer-fluid mixing solution. The work of HONG ET AL. (2008, 2009) represent a research study with the basic intention from the works of GIBBS (1978), Biot's theory of poroelasticity (BIOT, 1941), Flory-Huggins (FLORY, 1942; HUGGINS, 1942), and Flory-Rehner (FLORY & REHNER JR, 1943). In their work, for obtaining the equilibrium solution, the stretch of a free-swollen hydrogel was calculated following mechanical constraints and forces applied on the swollen hydrogel. This problem was modeled as a compressive hyperelastic material to obtain the final deformation and solvent distribution. According to the Flory–Huggins theory, the well-known free energy of polymer-fluid mixing per segment for a general binary system is defined by,

$$\Psi_{mixing}(\phi_p) = \frac{RT}{\Lambda\phi_p}\big((1-\phi_p)\ln(1-\phi_p) + \chi\phi_p(1-\phi_p)\big)\,, \tag{1.1}$$

where, ϕ_p represents the polymer volume fraction with respect to the existing fluid content[1], χ is defined as the dimensionless interaction parameter, R is the universal gas constant, T describes the room temperature, Λ is expressed as the fluid molar volume. The described mixing free energy of polymer-fluid in Eq. (1.1), is commonly utilized by HONG ET AL. (2008, 2009); LOEFFEL & ANAND (2011); CHESTER ET AL. (2015); ANAND (2017). Meanwhile, Eq. (1.1) is only associated with the polymer-fluid interaction, without considering

[1]The changes in the fluid content inside the polymer network cause the swelling stretch λ_f or the swelling deformation $\mathbf{F}_f$ (here is assumed an isotropic deformation). The important swelling constraint in volume per unit reference volume can be described by,

$$J_f = \det\mathbf{F}_f = (\lambda_f)^3 = 1 + \Lambda c_f = 1/\phi_p, \quad 0 < \phi_p \leq 1$$

where, c_f describes the fluid content. Meanwhile, the polymer volume fraction ϕ_p is less than (swollen state) or equal to one (dry state).

the chemical mixing resulting in the chemical reaction. The final goal of this study on the theoretical and computational models is to predict the gel's mechanical behavior by considering the proportions of the constituents and external agents (concentration of Ca^{2+} among others). For instance, this would allow to correlate the mechanical properties of the obtained to sodium alginate the quantity of Ca^{2+} employed in the design of the hydrogel. This predictive perspective would describe the first step toward a complete and precise mastership of the scaffold preparation.
Unfortunately, most available models allow to effectively and consistently account for swelling mechanisms associated with fluid movements but do not include the complex combination of chemo-mechanical effects associated with the diffusion and reaction kinetics of a crosslinking agent, which affect couple poroelastic mechanisms with the chemical reaction kinetics of a crosslinking agent. Moreover, to the best of the authors' knowledge, modeling frameworks accounting for the influence of internal stresses on crosslinking rates in hydrogels are not available. Thus, if this coupling effect has a relevant impact in final applications cannot be evaluated. In general, limitations in the chemo-mechanical description of crosslinking reaction kinetics in hydrogels decreases the predictive capabilities of existing modeling frameworks in capturing the cascade of events occurring during the production of hydrogel-based constructs. The present work aims to contribute in this direction.
This dissertation is specialized to applications of alginate hydrogels, although most equations find general applicability. One of the most viable physical-crosslinkers (e.g., ionic) for alginate is calcium chloride solutions ($CaCl_2$). Physical-crosslinking with calcium ions is a highly uncontrolled process because of its high degree of solubility in aqueous solutions (COLOSI ET AL., 2016; LEE & MOONEY, 2012; TALEI FRANZESI ET AL., 2006). The crosslinking rate depends on alginate and $CaCl_2$ concentration, which controls hydrogel homogeneity and mechanical strength. The crosslinking process changes the polymeric network's topology, resulting in syneresis and stiffening the hydrogel structure. Moreover, diffusive processes are affected by changes in the polymer mesh size, inducing possible obstruction of fluid permeation (COLOSI ET AL., 2016; POTTER ET AL., 1994; SALAHSHOOR & RAHBAR, 2014). Therefore, a suitable *in silico* model for predicting the strongly coupled chemo-mechanical behavior of alginate hydrogels during physical-crosslinking is highly required. A proper computational multiphysics model can help experimentalists better understand geometrical, mechanical, and chemical effects and optimize the crosslinking procedure for meeting design criteria.

1.5 Scope of study

This work's primary purpose is to develop and implement a chemo-mechanical theory under finite strains of coupled diffusion, reaction, and deformation mechanisms in hydrogels. The diffusion and reaction kinetics of a crosslinking agent (e.g., calcium) are explicitly accounted for and explicitly related to shrinking effects that counteract fluid-induced swelling. The final concentration of crosslinks within the hydrogel affects both mechanical and diffusive properties. Apart from alginate composition and calcium concentration, the crosslinking reaction rate result also directly depending on internal mechanical actions from thermodynamic arguments. Thermodynamic arguments will show that the crosslinking reaction rate is affected

not only by alginate composition and calcium concentration but also by internal mechanical actions. It results in a two-way coupling between chemistry and mechanics (i.e., between reactions with swelling mechanisms and external loads). The proposed theory has been implemented in a finite element framework based on a chemo-mechanical monolithic coupling, and several numerical tests are presented and discussed in view of available experimental evidence.

Five chapters follow this introduction.

Chapter 2 addresses reaction-diffusion mechanisms that occur during crosslinking of alginate hydrogels via $CaCl_2$, investigating them both experimentally and theoretically. A mathematical model is developed and calibrated using standard experimental procedures, easily reproducible, and low-cost. In particular, the effects of crosslinking dependent mechanisms on hydrogel diffusivity properties are primarily investigated.

The reaction-diffusion model, coupled with a continuum-based constitutive mechanical theory within a unified and thermodynamically consistent modeling framework, will be presented in Chapter 3. The governing balance laws will be described and implemented in a finite-element based numerical scheme. The proposed study addresses a novel chemo-mechanical model for alginate hydrogels' swelling behavior under a crosslinking agent's influence, such as calcium chloride $CaCl_2$ solution. The system considers the shrinking and swelling effects, fluid movements, as well as the reaction kinetics of calcium-induced crosslinking. Crosslinks change mechanical and diffusive properties inside the hydrogel. The model is developed in large strain/deformation theory under isothermal conditions. The proposed theory is based on strong/solid thermodynamic considerations that reveal the influence of internal stresses on the crosslinking kinetics. Hence, it recognizes a two-way coupling between mechanics and chemistry.

The implemented numerical methods and algorithms for solving the nonlinear partial differential equations (i.e., PDEs) obtained from the multiphysical continuum mechanical framework are introduced in Chapter 4. Further, a summary of the implemented Finite Element Method (FEM) fundamentals will be described.

Chapter 5 introduces the representative numerical simulations that are shown on the chemo-mechanical response of several examples such as a cubic (three-dimensional) hydrogel specimen, hydrogel tubes, cuboid gels, spherical gel under mechanical constraint, and a polymeric bilayer bar, which all the mentioned study cases are undergoing crosslinking agent to demonstrate the robustness of the developed element. The current analysis focuses on demonstrating the proposed model's capability to elucidate complex coupled multiphysics phenomenon and mechanism, showing the developed numerical implementation's effectiveness. Finally, this is followed by the conclusion and outlooks in Chapter 6.

Chapter 2

Mathematical and experimental modeling of hydrogel crosslinking

As discussed in Chapter 1, currently, there is still a lack of knowledge and computational tools for predicting the heterogeneous gelation pattern induced by Calcium driven crosslinking in sodium alginate hydrogels (GUNGOR-OZKERIM ET AL., 2018). For instance, crosslinking effects on the diffusion of gelation agents are generally not considered in the available computational models. Nonetheless, this mechanism affects the evolution of the solidified gel's front in the final bioprinted structure. For these reasons, this chapter aims to develop a mathematical model that describes reaction-diffusion mechanisms occurring during alginate hydrogel crosslinking in $CaCl_2$ and calibrate this model using standard experimental procedures, easily reproducible, and low-cost. In particular, the effects of crosslinking dependent mechanisms on hydrogel diffusivity properties are primarily investigated.

2.1 Experimental tests

Experiments presented here have been conducted by Franca Scocozza and Michele Conti from the University of Pavia. The experimental protocol is described for the sake of completeness and the understanding of the presented results.

2.1.1 Hydrogel preparation

Commercial sodium alginate (SA), gelatin (Gel), and calcium chloride ($CaCl_2$) are used (Sigma-Aldrich, Gillingham, UK). The gel was dissolved into 72°C PBS solution and mixed at 60°C. SA was added to the gel and blended for 5 min at 60°C with magnetic stirring. Then, SA-Gel hydrogel was centrifuged at 2000 rpm for 5 minutes (Heraeus Megafuge 16R Centrifuge, Thermo Scientific, Waltham, MA, USA) to eliminate air bubbles. The hydrogel was loaded into a syringe and stored in a fridge at 4°C overnight. After 24 hours, the syringe was immersed in a water bath at 25°C for 1 hour. Finally, the culture medium was added to SA-Gel hydrogel to reach the final concentration of 8%(w/v) SA and 4%(w/v) Gel. The solution was swapped repeatedly among two syringes through a Luer connector until the blend was homogenized. The crosslinking agent consists of 1%(w/v) $CaCl_2$ solution, and it

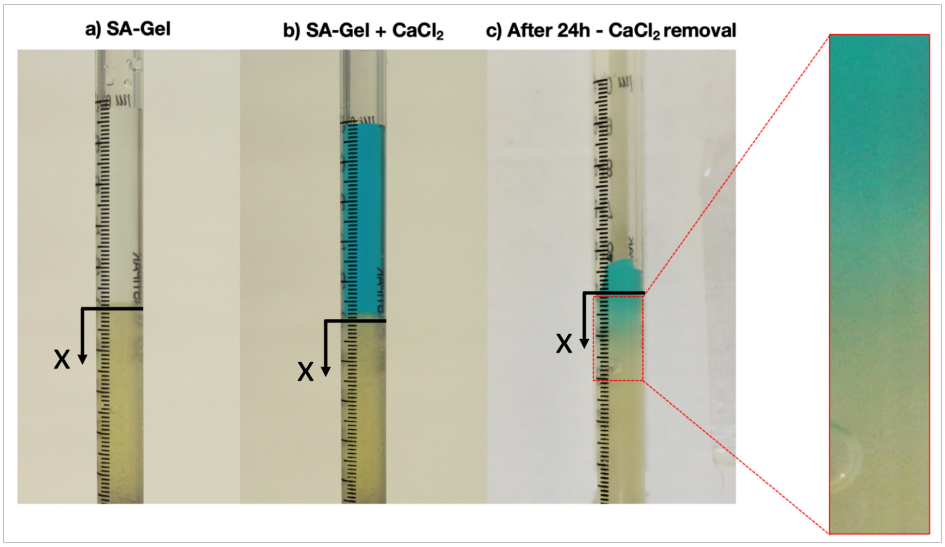

Figure 2.1: Experiment set-up: a) 0.5 ml of 8%(w/v)SA-4%(w/v)Gel was loaded in a syringe and weighted; b) 0.5 ml of 1%(w/v) $CaCl_2$ was added to the syringe for crosslinking the 0.5 ml of 8%SA-4%Gel hydrogel. c) After a given time t_{ca}, the excess calcium chloride was removed and weighted again. The amount of absorbed $CaCl_2$ was calculated doing the difference between the two measures. The focus shows the diffusion of the colored solution within the gel. Experiments have been conducted for $t_{ca} = 2, 5, 10, 15, 20$ minutes, as well as for 2, 24 and 48 hours. The case $t_{ca} = 24$ hours is shown in the image (By courtesy of University of Pavia).

is prepared using colored deionized water: 0.5 ml of blue food dye was added to 20 ml of deionized water.

2.1.2 Experimental set-up

0.5 ml of 8%(w/v)SA-4%(w/v)Gel hydrogel was transferred into eight different 1 ml syringes and weighted using a precision balance (Fig. 2.1a). 0.5 ml of 1%(w/v) $CaCl_2$ was added to the syringe for crosslinking the SA-Gel hydrogel (Fig. 2.1b). The excess calcium chloride was removed after 2, 5, 10, 15, 20 minutes, 2, 24, and 48 hours and the syringe was weighed again (Fig. 2.1c). The amount of $CaCl_2$ absorbed by SA-Gel hydrogel was calculated from the difference between the consecutive measures, converting it into a volume unit. Tests were repeated three times.

2.2 Theoretical and computational model

In agreement with experimental conditions, diffusive mechanisms in the hydrogel specimen can be described as a one-dimensional problem. Therefore, the geometry of the hydrogel is defined employing the scalar coordinate variable $x \in [0, L]$ (Fig. 2.1), where L is the length of the gel inside the syringe. For describing crosslinking dynamics, the time variable $t > 0$ is also introduced. Two internal variables define the chemical system,

1. gelation degree $\alpha = \alpha(x,t)$;
2. calcium concentration $c_c = c_c(x,t)$.

The gelation degree α represents the ratio between the solid gel concentration c_g of the chemically cross-linked polymer chains and the initial concentration of free-alginate c_A (before crosslinking), here equal to c_A= 0.08 mg μl^{-1} from hydrogel preparation (8%(w/v)SA). Neglecting the free-alginate diffusivity in comparison to the calcium diffusivity, it always results $c_g \leq c_A$, and thus

$$\alpha = \frac{c_g}{c_A} \in [0,1]\,. \tag{2.1}$$

As schematically depicted in Fig. 2.2, when $\alpha = 0$, polymer chains are non-cross-linked, and the gel exhibits a liquid-like behavior; when $\alpha = 1$, all polymer chains in the gel are crosslinked, and the gel can be considered as fully solid. The intermediate case $0 \leq \alpha \leq 1$ corresponds to a partially crosslinked network. The physical properties of the gel (e.g., stiffness, permeability, etc) smoothly vary from fully-liquid (at $\alpha = 0$) to fully-solid (at $\alpha = 1$) values. A characteristic gelation point $\alpha_{\text{gel}} \in (0,1)$ can be identified as the gelation degree over which the gel exhibits a solid-like response although not being fully crosslinked. Calcium concentration c_c and the gelation degree α are described through the Mikkelsen-Elgsaeter model, here considered in its reduced form under the assumption of negligible free-alginate diffusion (MIKKELSEN & ELGSAETER, 1995). The gelation degree is considered to affect the diffusion coefficient D governing calcium transport. Therefore, a coupled system arises, where the transport and the gelation-reaction affect each other. In particular, D is postulated as a function of α, here chosen as:

$$D(\alpha) = D_0 + (D_1 - D_0)\frac{\exp(-n\alpha/\alpha_{\text{gel}}) - 1}{\exp(-n/\alpha_{\text{gel}}) - 1}\,. \tag{2.2}$$

where D_0 represents the diffusion coefficient of the gel in its liquid-like phase (i.e., $\alpha = 0$), D_1 is associated with a fully solid state (i.e., $\alpha = 1$) and $n \in (0,5)$ is a model parameter governing the rate of diffusivity change.

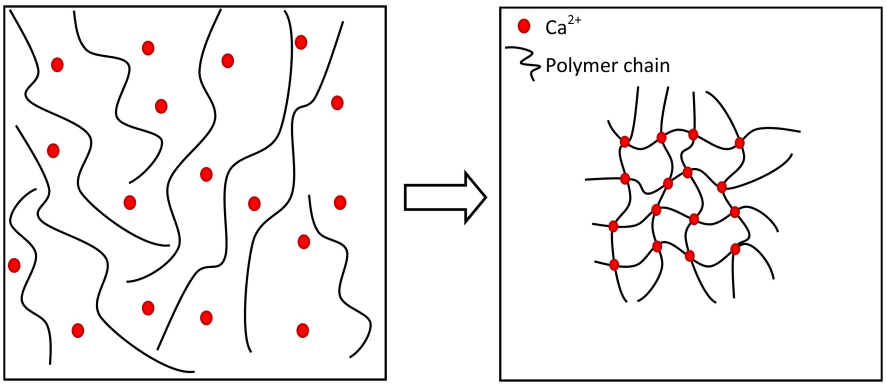

Figure 2.2: Chemical crosslinking during the gelation process: from a fully non-cross-linked network ($\alpha = 0$, left) to a fully cross-linked gel ($\alpha = 1$, right). The red dots and black chains represent calcium ions and polymer chain, respectively.

2.2.1 Diffusion

Diffusion of the calcium in the specimen is described by the strong form of a reaction diffusion equation:

$$\frac{\partial c_c}{\partial t} - \frac{\partial}{\partial x}\left(D\frac{\partial c_c}{\partial x}\right) = r = N_c c_A \frac{\partial \alpha}{\partial t}\,, \tag{2.3}$$

where ∂ denotes partial derivatives, r is a consumption term due to the chemical reaction and N_c is the stoichiometric coefficient, namely the average number of Ca^{2+} ions per alginate-alginate formation (MIKKELSEN & ELGSAETER, 1995). Note that diffusivity D is a function of the crosslinking degree α and that, in general, the latter can depend on the coordinate x. Therefore, D in Eq. (2.3) is an implicit function of space. The weak formulation can be obtained by applying an arbitrary test (or shape) function η to Eq. 2.3,

$$\int_L -\frac{\partial \eta}{\partial x}\left(D\frac{\partial c_c}{\partial x}\right) dL + \int_L \left(\frac{\partial c_c}{\partial t} - N_c c_A \frac{\partial \alpha}{\partial t}\right)\eta\, dL + \left[\eta D \frac{\partial c_c}{\partial x}\right]\Bigg|_0^L = 0\,. \tag{2.4}$$

2.2.2 Chemical reaction

The gelation degree evolves with the ordinary differential equation,

$$\frac{\partial \alpha}{\partial t} = K\,\frac{c_c}{c_A}\,(1-\alpha), \tag{2.5}$$

where K is a model parameter governing the reaction rate. It is noteworthy to mention that Eqs. (2.3) and (2.5) can be derived rigorously from the gelation degree model as shown in Chapter 3(Section 3.1).

2.2.3 Computational strategy

Hydrogel crosslinking is described using the partial differential problem represented by the coupling of the transport equation Eq. (2.3) and the reaction equation (2.5). An additional source of coupling is given by Eq. (2.2). The diffusion coefficient D depends indeed on the gelation degree α, given by the reaction equation's solution. The latter depends on calcium concentration c_c, obtained from the transport problem solution, which is affected by the diffusion coefficient.

The diffusion equation (2.3) is solved by discretizing the unknown function $c_c(x,t)$ by means of a backward-Euler difference scheme in time and a finite element discretization in space. The overall time interval $t \in [0, t_{\text{end}}]$ is split in n_t time intervals with constant time increments $\Delta t = t_n - t_{n-1}$ (with $n = 1,\ldots,n_t$). Moreover, N finite elements in the spatial domain $x \in [0, L]$ are introduced, together with a set of linear shape functions (also known as a test function η) $N_i(x)$[1] (with $i = 1,\ldots,N+1$). Accordingly, the calcium concentration function

[1]The linear shape function is described by $0 \le x \le L$ along each element as,

$$N_i(x) = \frac{L-x}{L}\,, N_{i+1}(x) = \frac{x}{L}.$$

Time	2 min	5 min	10 min	15 min	20 min	2 h	24 h	48 h
mean (μl)	2.97	5.13	6.01	7.77	8.95	18.25	53.38	78.65
s.d. (μl)	0.90	0.79	0.82	0.63	1.37	5.01	8.17	8.00

Table 2.1: Experimental data: absorbed $CaCl_2$ solution volume at different times.

is discretized through:

$$c_c(x,t) = \sum_{i=1}^{N+1} N_i(x) c_{ci}(t)\,, \tag{2.6}$$

where $c_{ci}(t)$ represent nodal unknowns, whose time derivatives at time $t = t_n$ are ($n = 2,\ldots,n_t$):

$$\left.\frac{\partial c_{ci}}{\partial t}\right|_{t=t_n} = \frac{c_{ci,n} - c_{ci,n-1}}{\Delta t}\,, \tag{2.7}$$

with $c_{ci,n} = c_{ci}(t_n)$ being the value of nodal unknown at time t_n. Therefore, neglecting boundary terms, the discretized weak form at time $t = t_n$ reads:

$$\sum_{i=1}^{N+1} \mathbb{K}_{ji,n} c_{ci,n} = f_{j,n} \tag{2.8}$$

where the stiffness term $\mathbb{K}_{ji,n}$ is:

$$\mathbb{K}_{ji,n} = \int_0^L \left[D(\alpha_n) \frac{\partial N_i}{\partial x}\frac{\partial N_j}{\partial x} + \frac{1}{\Delta t} N_i N_j \right] dx\,, \tag{2.9}$$

and the source term $f_{j,n}$ results:

$$f_{j,n} = \sum_{i=1}^{N+1} \left(\int_0^L (\frac{1}{\Delta t} N_i N_j + r N_j) dx \right) c_{ci,n-1}\,. \tag{2.10}$$

In Eq. (2.9) the diffusion coefficient D is computed on the basis of the gelation degree $\alpha_n = \alpha(x,t_n)$ at time t_n, which is in general inhomogeneous in space, i.e., $\alpha_n = \alpha_n(x)$. A two-point Gauss quadrature rule is employed for spatial integration. Therefore, the value of diffusion, and hence of gelation, is required at integration points. The value α_n^g from Eq. (2.5) at time t_n in the integration point x_g explicitly is given by:

$$\alpha_n^g = \alpha_{n-1}^g + K \frac{c_{cn-1}^g}{c_A} (1 - \alpha_{n-1}^g) \Delta t\,, \tag{2.11}$$

where $c_{cn-1}^g = c_c(x_g, t_{n-1})$ is calcium concentration in Gauss point x_g at time t_{n-1} and K is the reaction rate.

In order to reproduce experimental conditions, the following set of boundary (B.C.) and initial (I.C.) conditions (see Fig. 2.3) are considered for numerical simulations:

$$\text{B.C.:} \begin{cases} c_c = \hat{c}_c & \text{for } x = 0 \text{ and } \forall\, t \\ \dfrac{\partial c_c}{\partial x} = 0 & \text{for } x = L \text{ and } \forall\, t \end{cases}, \tag{2.12}$$

$$\text{I.C.:} \quad c_c(x,0) = 0 \quad \text{for } x \neq 0\,, \tag{2.13}$$

Time	2 min	5 min	10 min	15 min	20 min	2 h	Average
$D_0 = 0.83$	4.98	0.17	42.61	53.23	70.07	262.51	72.26
$D_0 = 0.72$	13.28	8.07	31.21	41.12	56.72	234.73	64.19
$D_0 = 0.50$	31.65	26.47	5.66	13.96	26.74	172.14	46.10
$D(\alpha)$	19.33	23.01	1.24	2.82	8.74	12.85	11.33

Table 2.2: Absorbed $CaCl_2$ solution volume: normalized deviation (%) of model predictions with respect to the mean of experimental data at different times (Table 2.1). The average error is reported. Model results are obtained employing a constant diffusivity for different values D_0 ($\times 10^{-9}$ m^{2}s^{-1}) and by employing function $D(\alpha)$ in Eq. (2.2).

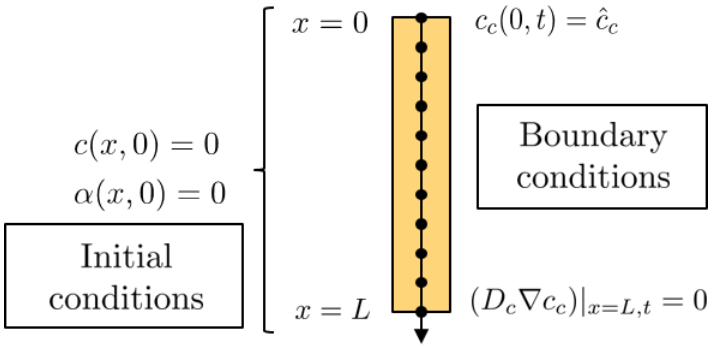

Figure 2.3: Simulation settings.

The assigned boundary concentration $\hat{c}_c$ is given by $\hat{c}_c = \mathrm{w_{Ca}} \cdot \hat{c}_{\mathrm{CaCl_2}}$ where $\hat{c}_{\mathrm{CaCl_2}} = 0.01$ mg μl^{-1} from crosslinker preparation (1% (w/v) $CaCl_2$) and $\mathrm{w_{Ca}}$ is the weight fraction of Ca^{2+} in $CaCl_2$ ($\mathrm{w_{Ca^{+2}}} = 0.36$). For the calibration of the diffusion parameter function in Eq. (2.2), a reference value $\bar{D}_0$ for D_0 is obtained from the mean of experimental data by BRASCHLER ET AL. (2011), resulting equal to $\bar{D}_0 = 0.83 \times 10^{-9}$ m^{2}s^{-1}. Moreover, parameter D_1 is chosen to be a fraction δ of $\bar{D}_0$, i.e., $D_1 = \delta \bar{D}_0$. As discussed in the following Section, $\delta = 0.5$ agrees well with data from molecular dynamics simulations (SALAHSHOOR & RAHBAR, 2014). Similarly, the gelation point $\alpha_{\mathrm{gel}} = 0.2$ will be adopted. The stoichiometric coefficient $N_c = 0.1$ is obtained by THU ET AL. (2000) and the diffusivity rate change parameter $n = 5$ has been calibrated based on the experimental result. Finally, addressing the gelation mechanism (Eq. (2.5)), the value $K = 0.03$ s^{-1} has been chosen for the reaction rate constant (see Discussions and Conclusions). Validation and effectiveness of the proposed model will be investigated on the basis of the time evolution of the total absorbed volume V_c of $CaCl_2$ solution, i.e., of function $V_c(t)$. This is read from the computed flux of calcium on the top surface of the gel ($x = 0$), as:

$$V_c(t) = \frac{A}{\mathrm{w_{Ca}} \cdot \rho^{\mathrm{Solution}}_{\mathrm{CaCl_2}}} \int_0^t D \frac{\partial c_c}{\partial x}|_{x=0} \, dt \,, \tag{2.14}$$

with the syringe cross-sectional area being equal to $A = 17.81$ mm^2 and the solution density $\rho^{\mathrm{Solution}}_{\mathrm{CaCl_2}}$ is estimated as $0.01 \rho^{\mathrm{Powder}}_{\mathrm{CaCl_2}}$ where $\rho^{\mathrm{Powder}}_{\mathrm{CaCl_2}} = 2.15$ mg μl^{-1} is the density of the powder of $CaCl_2$. Based on the volume occupied by the gel in the syringe, L results equal to 28 mm.

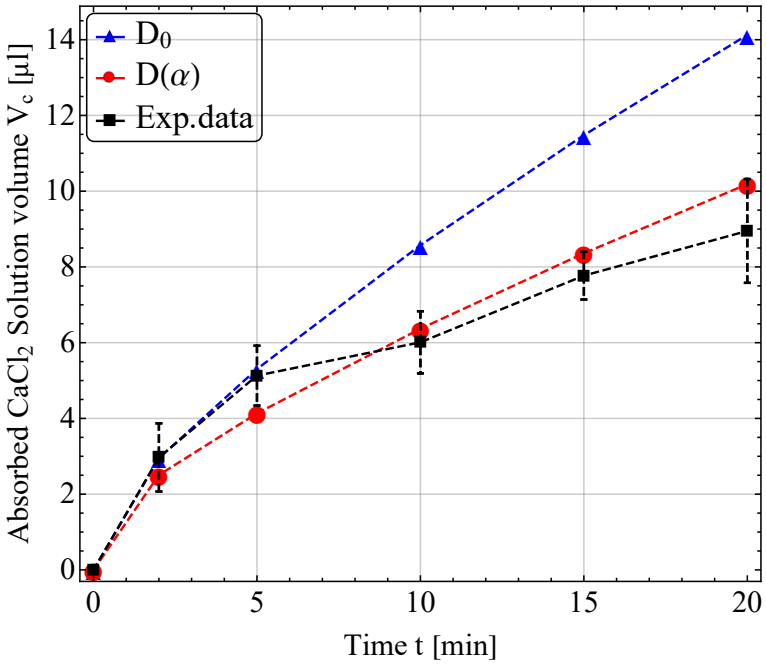

Figure 2.4: Model validation: absorbed $CaCl_2$ solution volume versus time. Comparison between experimental data and model results with gelation-dependent diffusion coefficient $D(\alpha)$ in Eq. (2.2) and constant diffusion coefficient $D = D_0$; both modelling results employ $D_0 = \bar{D}_0 = 0.83 \cdot 10^{-9}$ $m^2 s^{-1}$ by BRASCHLER ET AL. (2011).

Crosslinking-dependent effects are investigated comparing the capability of the diffusion model in Eq. (2.3) in reproducing experimental data by adopting a simplified approach which assumes a constant diffusion parameter $D = D_0$. Furthermore, the sensitivity of results with respect to δ, α_{gel} and K will be also investigated in a parametric campaign of simulations. The value $\Delta t = 20$ seconds has been employed in numerical simulations by addressing a final simulation time t_{end} equal to 2 hours. A sensitivity study has been conducted in order to prove that results are not sensitive to variations of Δt for $\Delta t \leq 20$ seconds. No numerical issues have been experienced in the afore-specified range of values.

2.3 Experimental results and model validation

Experimental results for means and standard deviations of V_c are reported in Table 2.1 up to two days. The accurateness of the adopted experimental methodology is proved by the robustness of measures (n.s.d. $\approx 10 - 15\%$). Experimental data are also reported in Fig. 2.4, Fig. 2.5 up to 20 minutes, which is the time range of practical interest for 3D-printing applications.

Figures 2.4, 2.5 reports also modelling predictions. As shown in Fig. 2.4, function $V_c(t)$ obtained with a constant diffusivity $D = \bar{D}_0$ significantly deviates from experimental data. As reported in Table 2.2, the normalized average error up to 2 hours is above 30% for the reference value $D_0 = \bar{D}_0$. On the other hand, accounting for the dependence of the diffusivity on crosslinking (i.e., $D(\alpha)$), experimental data can be accurately fitted, even considering

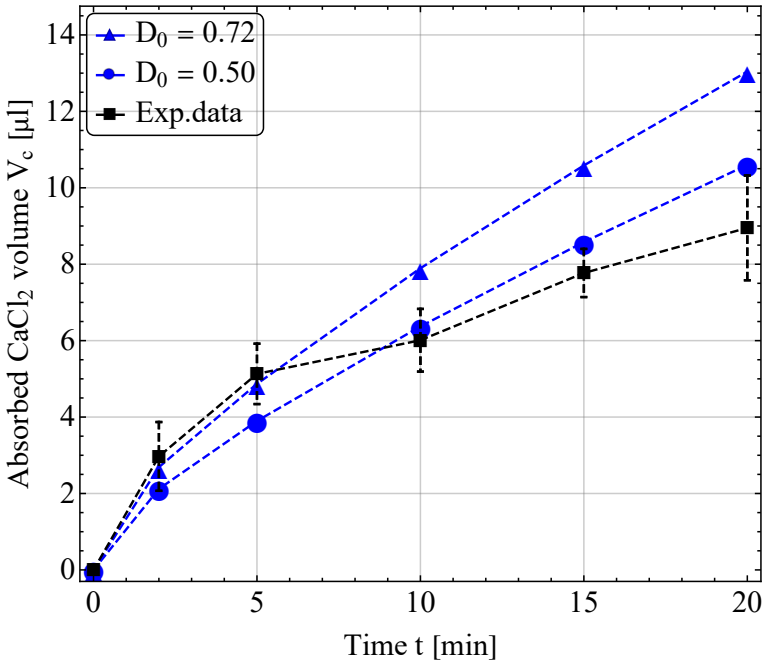

Figure 2.5: Model validation: absorbed $CaCl_2$ solution volume versus time. Comparison between experimental data and model results with constant diffusion coefficient $D = D_0$ for different values D_0.

$D_0 = \bar{D}_0$. The average error results equal to about 6% with respect to mean values (cf., Table 2.2). Remarkably, model predictions are always within a standard deviation of experimental measurements.
Clearly, when employing a constant diffusivity, parameter D_0 might be tuned in order to fit the obtained experimental data. This is shown in Fig. 2.5 and Table 2.2. It is worth highlighting that a good fitting is possible only for D_0 lying significantly outside of the experimental range reported by BRASCHLER ET AL. (2011), that is $D_0 \in (0.72-0.94)\times 10^{-9}$ $m^2 s^{-1}$.

2.4 Crosslinking effects

The evolution of calcium concentration c_c is reported in Fig. 2.6, showing the effects of a crosslinking dependent diffusivity concerning a constant one. The gelation, i.e., forming new crosslinks between polymeric chains, represents an obstacle to diffusion, inducing a slower diffusive process, which is captured by the proposed modeling framework, as shown by the evolution of the effective diffusivity D in Fig. 2.7. Although D is explicitly only a function of α from Eq. (2.3), it depicts the variation in time and space within the gel due to inhomogeneities in the gelation degree α.
The evolution of α in time and space is reported in Fig. 2.8. Since actors of a strongly coupled system, α is affected by choice of a constant or a varying diffusivity. Although D does not explicitly appear in Eq. (2.5), variations of D affect the calcium concentration distribution $c_c(x,t)$, which in turn affects the gelation rate.

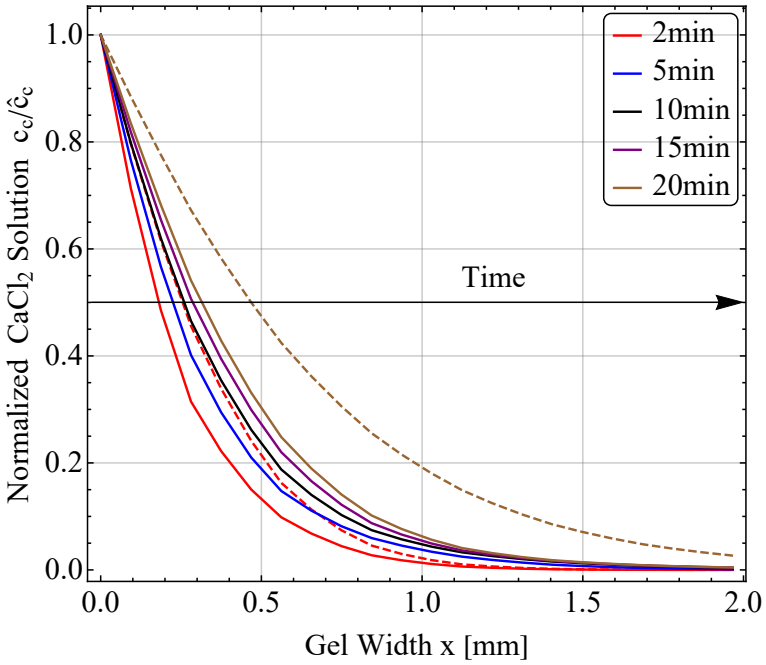

Figure 2.6: Crosslinking effects: calcium concentration function $c(x,t)$, normalized with respect to applied boundary concentration $\hat{c}$. Results are reported along gel's width $x \in [0, L]$ for different values of time $t = 2, 5, 10, 15, 20$ minutes. Dashed lines in plot correspond to results obtained with a constant diffusivity $D = \bar{D}_0 = 0.83 \times 10^{-9}$ m^{2}s^{-1} obtained from BRASCHLER ET AL. (2011).

This outcome has relevant consequences for applications. For instance, the front of the solidified portion of the gel evolves significantly differently when considering a varying or a constant diffusivity. This is depicted in Fig. 2.9, where the gel front x_{gel} that is the coordinate x for which $\alpha(x_{\text{gel}}) = \alpha_{\text{gel}}$, is reported versus time. Accounting for a constant diffusivity, the width of the gel front might be generally overestimated of about 20% (around $100\,\mu m$ at $t = 10$ minutes).

2.5 Parametric study

The robustness of data fitting with respect to uncertainties on the values of model parameters is analyzed by means of a parametric analysis. Addressing parameters $p = \delta$, α_{gel} and K, the average normalized variation $\Delta V_p(s)$ of absorbed $CaCl_2$ volume at $p = s$ is estimated as:

$$\Delta V_p(s) = \frac{1}{n_\Delta} \sum_i^{n_\Delta} \frac{V_c(t_i; p = s) - V_c(t_i; p = \bar{s})}{V_c(t_i; p = \bar{s})}, \tag{2.15}$$

where $V_c(t_i; p = s)$ represents function $V_c(t)$ at $t = t_i$ obtained employing value s for model parameter p. Moreover, t_i are n_Δ discrete values of time in $(0, t_{\text{end}}]$ and $\bar{s}$ is a reference value. In particular, it is employed $\{t_1, \ldots, t_5\} = \{2, 5, 10, 15, 20\}$ minutes, and $\bar{s} = \bar{\delta}, \bar{K}$ with $\bar{\delta} = 0.5$, and $\bar{K} = 0.03$ as in previous numerical tests.

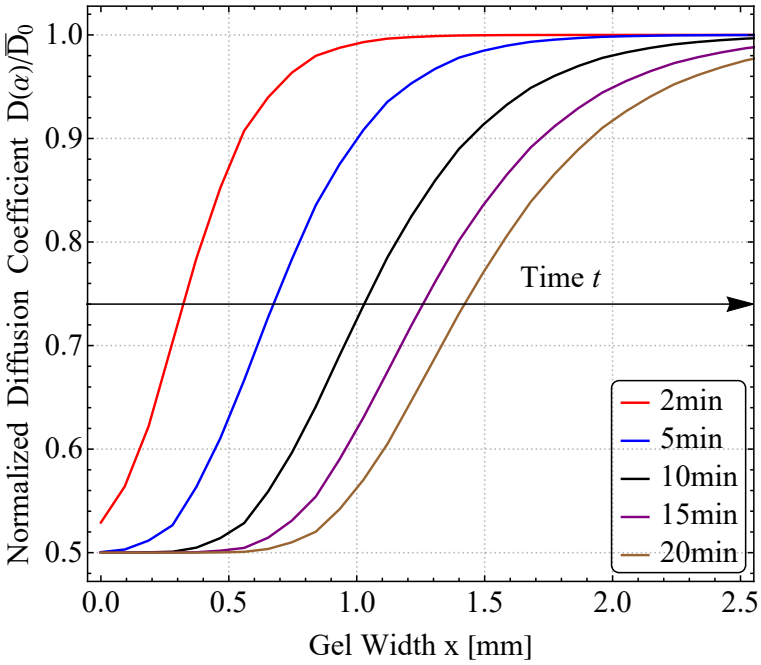

Figure 2.7: Crosslinking effects: diffusivity D, normalized with respect to the reference diffusivity constant $D_0 = \bar{D}_0$. Results are reported along gel's width $x \in [0, L]$ for different values of time $t = 2, 5, 10, 15, 20$ minutes.

The results of this parametric campaign of simulations are shown in Figs. 2.10, 2.11 and 2.12. The conducted analysis depicts that the absorbed $CaCl_2$ volume highly varies with all parameters under investigation.

2.6 Discussions

The present study describes an experimental characterization and the computational modeling of hydrogel crosslinking. Chemical gelation has been addressed, analyzing the diffusion of $CaCl_2$ within the gel. Computational analysis is another critical element in bioprinting, which provides a tool to qualitatively and quantitatively investigate the relationship between the patterned construct and the biological outcome (CARLIER ET AL., 2016). NAGHIEH ET AL. (2018b) has investigated the effect of crosslinking mechanism on the mechanical behavior of 3D bioprinted alginate scaffolds by varying the crosslinking agent volume and crosslinking time. These two factors play a decisive role in modulating the elastic modulus of 3D bioplotted alginate scaffolds. Ca^{2+} ions promote the formation of G-blocks within the gel, stabilizing the polymeric network. Experimental data of absorbed volumes of $CaCl_2$ have been obtained and fitted through a reactive-diffusive model that accounts for crosslinking effects in diffusivity properties.
When employing a constant diffusivity $D = \bar{D}_0$, that does not depend on crosslinking; the obtained experimental data could not be fitted by employing constants' values D_0 within experimental ranges reported in the literature (BRASCHLER ET AL., 2011). In particular, a good fitting would require a diffusivity constant significantly lower than the self-diffusion

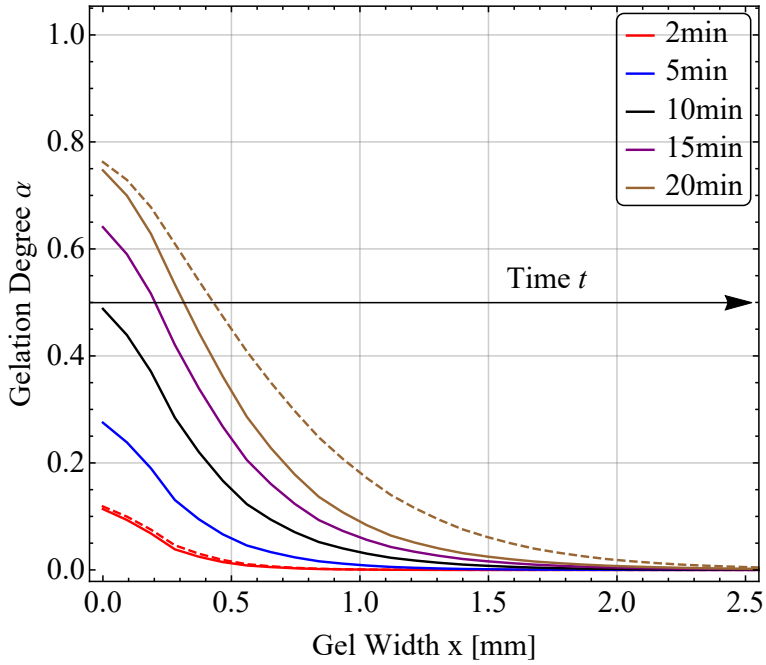

Figure 2.8: Crosslinking effects: gelation degree α. Results are reported along gel's width $x \in [0, L]$ for different values of time $t = 2, 5, 10, 15, 20$ minutes. Dashed lines in plot correspond to results obtained with a constant diffusivity $D = \bar{D}_0 = 0.83 \times 10^{-9}$ m^{2}s^{-1} obtained from BRASCHLER ET AL. (2011).

coefficient of Ca^{2+} ions in water at limiting dilution (equal to 0.78×10^{-9} m^{2}s^{-1}, (WANG, 1953)). It seems unreasonable since it is expected that Ca^{2+} ions can diffuse nearly unhindered through the gel before solidification because they are much smaller than the alginate gel's pore size (BRASCHLER ET AL., 2011).

On the other hand, by introducing a crosslinking dependent diffusion coefficient $D(\alpha)$, an excellent fitting of experimental data can be obtained. Remarkably, this has been obtained employing values of D_0 fully in agreement with experimental ranges. As regards the functional form chosen for $D(\alpha)$ in Eq. (2.2) results are sensitive to both the gelation point α_{gel}, and the diffusivity value D_1 at the solid-state. It has been shown in terms of sensitivity analysis. In particular, the reference value $\delta = 0.5$ has been chosen for the ratio $\delta = D_1/D_0$ based on evidence obtained from molecular dynamics simulations, which show an average decrease of 50% of water diffusivity in hydrogels before and after crosslinking (SALAHSHOOR & RAHBAR, 2014). Nevertheless, it is worth highlighting that more case-specific data would be required for a proper estimation based on the polymeric network structure at hand. In this regard, the functional form itself of $D(\alpha)$ in Eq. (2.2) is an arbitrary choice. Multiscale computational and modeling approaches describing crosslinking effects on polymer networks' features (i.e., pore size) might advantage a more physically-based description. Moreover, electrostatic effects associated with ions movements should also be taken into account.

The value of the reaction rate K has been chosen within the range $(10^{-4} - 10\text{s}^{-1})$ based on previously reported in the literature for the reaction kinetic constant $k = K/c_A^2$ (MIKKELSEN & ELGSAETER, 1995; THU ET AL., 2000). It is worth pointing out that the model chosen for

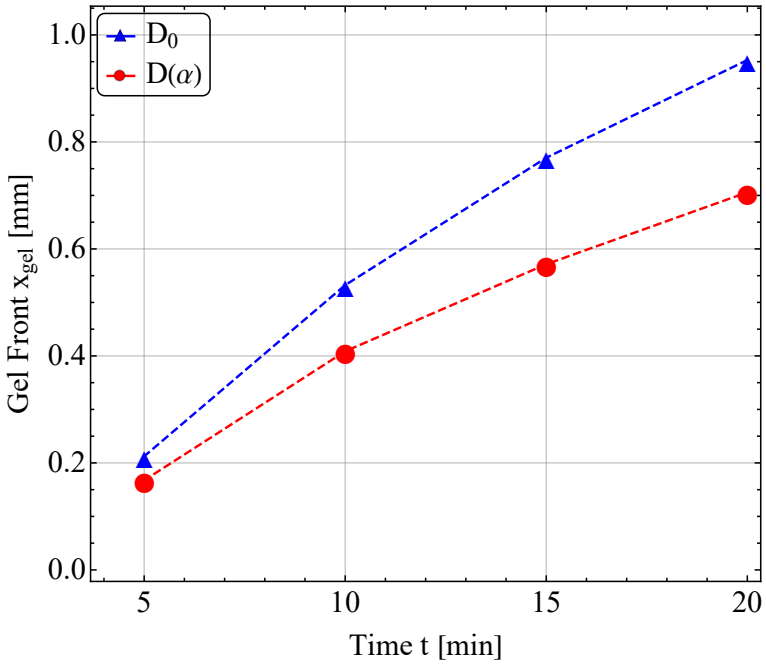

Figure 2.9: Crosslinking effects: gel front x_{gel}, such that $\alpha(x_{\text{gel}}) = \alpha_{\text{gel}}$, namely the gelation degree over which the gel exhibits a solid-like response. Results are reported along gel's width $x \in [0, L]$ for different values of time $t = 2, 5, 10, 15, 20$ minutes.

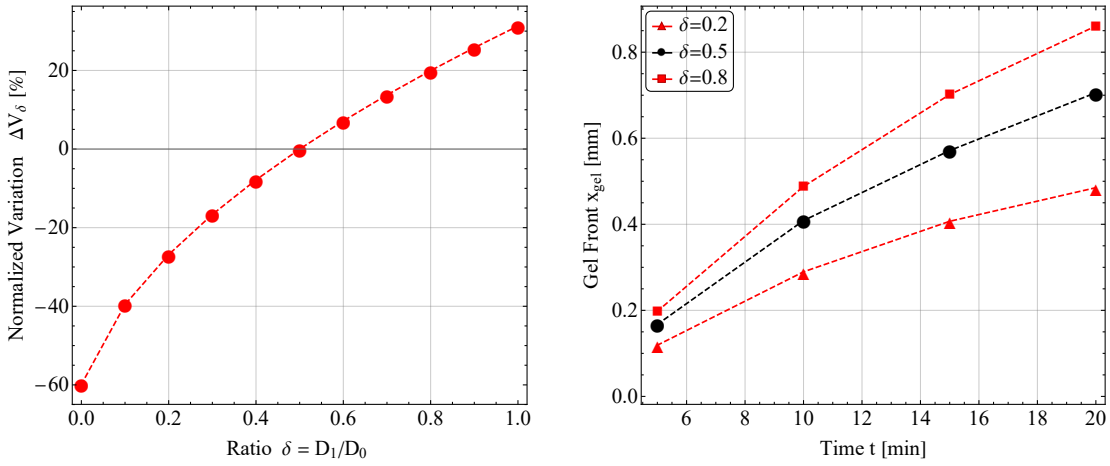

Figure 2.10: Parametric analysis for ratio $\delta = D_1/D_0$. Left: normalized volume variation ΔV_p (cf., Eq. (2.15)); right: gel front x_{gel}.

the reaction equation (2.5) is simplistic for the real physical mechanisms occurring within the gel. More refined approaches are indeed available in the literature (BRASCHLER ET AL., 2011). These are currently under investigation for future work since they would introduce parameters with a clear physical meaning and for which well-established experimental values would be available. As a matter of fact, K can have a relevant effect on the crosslinking agent's absorbed volume.

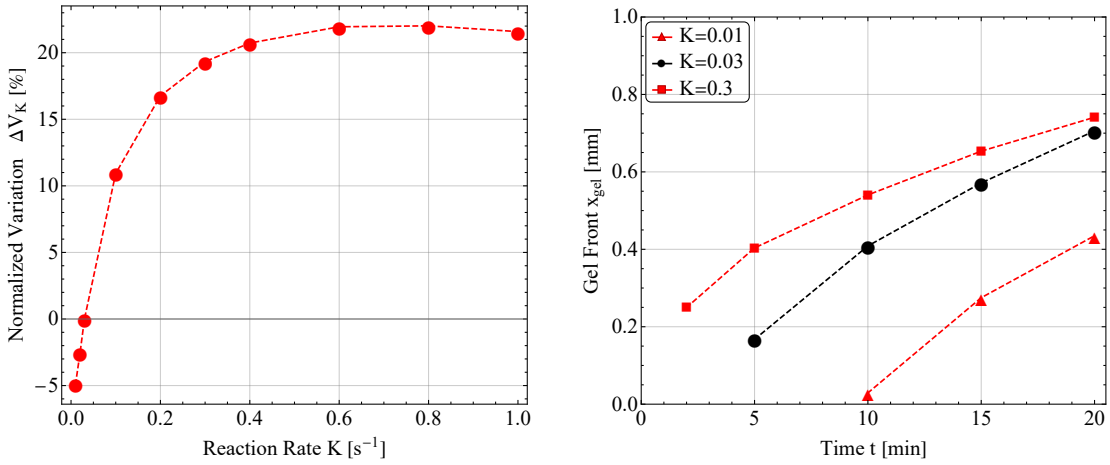

Figure 2.11: Parametric analysis for reaction rate K. Left: normalized volume variation ΔV_p (cf., Eq. (2.15)); right: gel front x_{gel}.

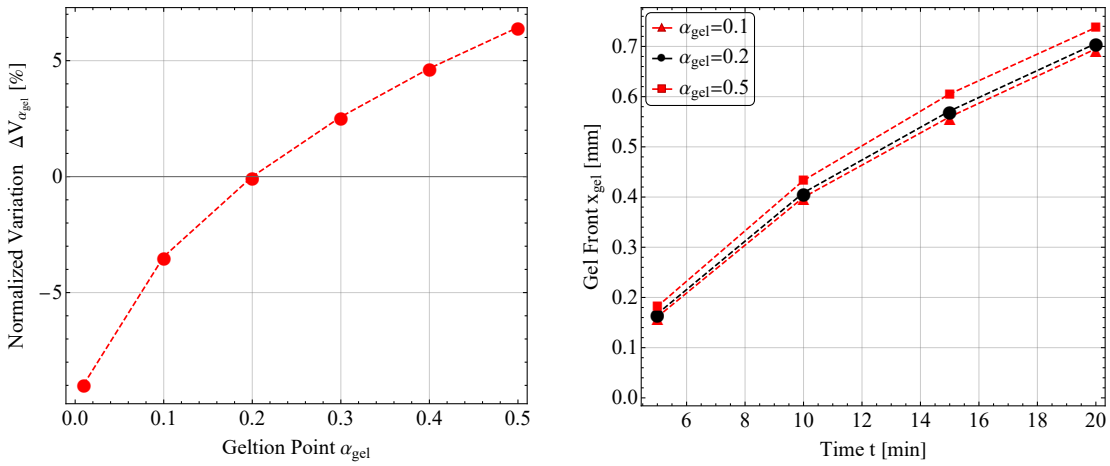

Figure 2.12: Parametric analysis for gel point α_{gel}. Left: normalized volume variation ΔV_p (cf., Eq. (2.15)); right: gel front x_{gel}.

From an applicative viewpoint, the present study addressed the evolution of the gel front with time. This information might guide the design of optimal post-printing protocols. Depending on modeling choices (i.e., constant versus crosslinking dependent diffusivity) and on the values of model parameters (i.e., diffusive properties at the solid-state and reaction rates), the predicted position of the gel front might differ of $\sim 100\,\mu m$. These differences are of significant relevance when addressing tissue engineering scaffolds obtained by means of bioprinting technologies. Hence, the local mechanical environment experienced by biological cells at different locations within the gel, hence their mechanobiological stimulus, would significantly vary with the gel state. Therefore, when a high resolution in the printing fidelity is required for bioprinting applications, *in silico* predictions are reliable only accounting for the coupled chemo-diffusion problem. The existing work represents the first step towards a full characterization and a comprehensive understanding of the involved mechanisms.

Moreover, a fundamental aspect that has not been taken into account in the present study is that volume changes due to fluid movements in porous materials can cause significant alterations in the porosity and permeability properties. Several poroelastic and poroelastoplastic theories are available in the literature and can reproduce the thermoelastic swelling response of polymeric materials properly (ANAND, 2017; DROZDOV & CHRISTIANSEN, 2013; BAEK & PENCE, 2011). Nevertheless, crosslinking induces shrinking, representing an inelastic deformation mechanism, concurrent to swelling, as well as the effects of crosslinking dependent variations of diffusion properties on poroelastic responses will be described in the following chapter. Hence, later advancements of the present study, which are presented in Chapter 3, will address the coupling of the proposed chemo-diffusive description of crosslinking with large deformation poroelastic theories of microporous polymeric materials (ANAND, 2017).

Chapter 3

Continuum multi-physics theory

This chapter presents the continuum-based constitutive theory and the governing balance laws of a novel chemo-mechanical model for alginate hydrogels' swelling behavior under a crosslinking agent's influence, such as calcium chloride $CaCl_2$. It addresses the shrinking and swelling effects, fluid movements influenced by the reaction kinetics of calcium-induced crosslinking. Crosslinks vary the mechanical and chemical properties in the hydrogel. The model is implemented in large strain/deformations theory under isothermal conditions. The current theory includes strong/solid thermodynamic considerations that describe the effect of internal stresses on the gelation kinetics. Consequently, it addresses a two-way coupling between mechanics and chemistry.

The standard notation of modern continuum mechanics (e.g. GURTIN ET AL., 2010; WRIGGERS, 2008) is employed. The hydrogel is considered a continuum body within the Euclidean space $\mathbb{E}^3$. The current configuration of the body at time $t \geq 0$ is described by means a one-to-one transformation mapping $\boldsymbol{\varphi} : \mathcal{B}_t \to \mathbb{E}^3$. The reference configuration $\mathcal{B}_o$ is assumed to be already swollen and thus obtained from the influx of fluid within a dry (and non-crosslinked) polymer, whose configuration is denoted by $\mathcal{B}_d$. It is noteworthy that $\mathcal{B}_o$ might or might not correspond to the current configuration $\mathcal{B}_0$ at time $t = 0$, but here is chosen $\mathcal{B}_o \equiv \mathcal{B}_0$.

The position vector in the reference configuration $\mathbf{X} \in \mathcal{B}_o$ relates to the one in the current configuration $\mathbf{x} \in \mathcal{B}_t$ as $\mathbf{x} = \boldsymbol{\varphi}(\mathbf{X}, t)$, from which the (material) displacement field reads $\mathbf{u}(\mathbf{X}, t) = \mathbf{x} - \mathbf{X} = \boldsymbol{\varphi}(\mathbf{X}, t) - \mathbf{X}$. The transformation map $\boldsymbol{\varphi}(\mathbf{X}, t)$ is described in terms of the (material) deformation gradient $\mathbf{F} = \nabla_{\mathbf{X}}\mathbf{x} = \partial\,\mathbf{x}/\partial\,\mathbf{X}$, with its determinant $J = J(\mathbf{X}, t) = \det\mathbf{F} \neq 0$ representing the volume change of a volume element $dv = JdV$ from the reference (dV) to the current (dv) configuration.

As notation rules, the spatial gradient is denoted by $\nabla_{\mathbf{x}}$, material and spatial divergence by $\nabla_{\mathbf{X}} \cdot (*)$, $\nabla_{\mathbf{x}} \cdot (*)$, while operators $\mathrm{tr}\mathbf{A}$ and $\mathrm{sym}\mathbf{A}$ denote respectively the trace and the symmetric part of a second-order tensor $\mathbf{A}$. The material time derivative of field $y(\mathbf{x}, t)$ in the current configuration is denoted by $\mathrm{D}y/\mathrm{D}t$. For quantities in the reference configuration $Y(\mathbf{X}, t)$, the material time derivative coincides with the partial one, which is denoted by the dot superscript, that is $\mathrm{D}Y/\mathrm{D}t = \partial Y/\partial t = \dot{Y}$.

Molar concentration fields represent the primary variables of the chemical description. For the chemical species β, the field $c_\beta(\mathbf{x}, t)$ represents its spatial concentration per unit volume of the current configuration in a spatial (Eulerian) description, while $C_\beta(\mathbf{X}, t)$ its material

concentration per unit volume of the reference configuration in a material (Lagrangian) description, resulting

$$C_\beta(\mathbf{X},t) = J(\mathbf{X},t)\, c_\beta(\boldsymbol{\varphi}(\mathbf{X},t),t)\,. \tag{3.1}$$

It is noteworthy that the introduced notation agrees with the one employed in Chapter 2, c_c representing in both cases, calcium concentration. Nevertheless, since Chapter 2 does not include kinematics of large deformation effects, no distinctions have been made between spatial and material concentrations. The number of moles $\mathcal{N}_\beta(t)$ of species β in a part $\mathcal{P}_t = \boldsymbol{\varphi}(\mathcal{P}_o,t) \subseteq \mathcal{B}_t$ of the hydrogel at time t hence reads:

$$\mathcal{N}_\beta(t) = \int_{\mathcal{P}_t} c_\beta(\mathbf{x},t)\, dv = \int_{\mathcal{P}_o} C_\beta(\mathbf{X},t)\, dV\,. \tag{3.2}$$

Poroelastic effects, due to the interaction between the solid polymer network and the fluid content, are accounted for by considering a homogenized material for the fluid-solid mixture (HONG ET AL., 2008; DUDA ET AL., 2010; GURTIN ET AL., 2010). The mechanics of swollen elastomers is described by coupling the (material) displacement field $\mathbf{u}(\mathbf{X},t)$ with the fluid concentration field $C_f(\mathbf{X},t)$. These variables will be accompanied by additional unknowns related to the chemical crosslinking kinetics, which will be introduced in the following section. The theory is developed under isothermal conditions.

3.1 Chemical model

Crosslinking in hydrogels represents a binary reaction-diffusion problem, in which the chemical reaction induces the formation of the crosslinks due to a diffusive crosslinking agent. Alginate is a type of naturally derived forming polymer. It is known to be a linear copolymer of guluronic and mannuronic acids (REES & SAMUEL, 1967). According to the egg-box model, calcium ions (Ca^{2+}) can bind the residues of guluronic acids, which consequently lead to forming the calcium-alginate hydrogel (MORRIS ET AL., 1978). The chemical reaction between alginate and Ca^{2+} can be described as (DUEZ ET AL., 2000; MIKKELSEN & ELGSAETER, 1995),

$$\text{alginate} + N_c\text{Ca}^{2+} \rightarrow \text{Ca}-\text{alginate}\,, \tag{3.3}$$

where N_c denotes the stoichiometric coefficient which depends on the amount of guluronic acid content inside the alginate. By introducing a sub-part $\mathcal{P}_t \subseteq \mathcal{B}_t$ within the hydrogel, the material (mole) balance equations governing the spatial concentration fields of (non-crosslinked) free-alginate c_a, of calcium ions c_c and of (Ca-alginate) gel c_g read in agreement with Eq (3.3):

$$\frac{\mathrm{D}}{\mathrm{D}t}\int_{\mathcal{P}_t} c_a dv = -\int_{\mathcal{P}_t} \nabla_{\mathbf{x}}\cdot\mathbf{j}_a dv - \frac{\mathrm{D}}{\mathrm{D}t}\int_{\mathcal{P}_t} c_g dv\,, \tag{3.4a}$$

$$\frac{\mathrm{D}}{\mathrm{D}t}\int_{\mathcal{P}_t} c_c dv = -\int_{\mathcal{P}_t} \nabla_{\mathbf{x}}\cdot\mathbf{j}_c dv - N_c\frac{\mathrm{D}}{\mathrm{D}t}\int_{\mathcal{P}_t} c_g dv\,, \tag{3.4b}$$

where $\mathbf{j}_a(\mathbf{x},t)$ and $\mathbf{j}_c(\mathbf{x},t)$ respectively denote the spatial diffusion vector fluxes of free-alginate and calcium ions (measured per unit area in the current configuration and per unit

time). Reaction terms in Eqs. (3.4) have been designed in agreement with the reaction relationship (3.3). In fact, excluding mass fluxes, an increase of gel concentration corresponds to an equal decrease of alginate from Eq. (3.4a) and to a proportional decrease of calcium (with proportionality constant corresponding to the stoichiometric coefficient) from Eq. (3.4b). By assuming gel diffusion as negligible, gel variation is only due to crosslinking kinetics which is described by MIKKELSEN & ELGSAETER (1995) in terms of a third-order reaction equation:

$$\frac{\mathrm{D}}{\mathrm{D}t}\int_{\mathcal{P}_t} c_g dv = \int_{\mathcal{P}_t} k\, c_a\, c_c (c_a + c_g)\, dv, \tag{3.4c}$$

where $k > 0$ is a third-order reaction parameter. MIKKELSEN & ELGSAETER (1995) show that the diffusivity of free alginate is a hundred times lower than the diffusivity of calcium ions. Moreover, as gel forms, the diffusivity of alginate decreases. Thereafter, in this study, alginate diffusivity is assumed to be negligible compared to calcium ions' diffusivity. Accordingly, the formulation in Eqs. (3.4) is here simplified by assuming a low free-alginate mobility (i.e., $\|\mathbf{j}_a\| \approx 0$). Via a pull-back transformation[1] from the current $\mathcal{P}_t$ to the reference $\mathcal{P}_o$ and exploiting the localization theorem, Eq. (3.4a) can be read as:

$$\dot{C}_a \approx -\dot{C}_g \quad \Rightarrow \quad \frac{\partial (C_a + C_g)}{\partial t} \approx 0\,. \tag{3.6}$$

Therefore, the sum $(C_a(\mathbf{X},t) + C_g(\mathbf{X},t))$ is constant in time. Hence, by introducing the material concentration field $C_A(\mathbf{X}) = C_a(\mathbf{X},0)$ of free-alginate at time $t = 0$, the following relationship holds true:

$$C_a(\mathbf{X},t) + C_g(\mathbf{X},t) = J(\mathbf{X},t)[c_a(\mathbf{x},t) + c_g(\mathbf{x},t)]|_{\mathbf{x}=\boldsymbol{\varphi}} = C_A(\mathbf{X})\,. \tag{3.7}$$

The extent of the chemical reaction is described by a (material) scalar variable $\alpha(\mathbf{X},t)$, referred to as gelation degree, defined in agreement with Eq. (2.1) as:

$$0 \leq \alpha(\mathbf{X},t) = \frac{C_g(\mathbf{X},t)}{C_A(\mathbf{X})} \leq 1\,. \tag{3.8}$$

Admissible physical values of gelation degree lie in the range $[0,1]$ because, for any time t, it results $C_g(\mathbf{X},t) > 0$ by definition and $C_g(\mathbf{X},t) \leq C_A(\mathbf{X})$ from Eq. (3.7). An upper limit $\alpha \leq \alpha_{lim} < 1$ might be also introduced in order to account for the fact that the full amount of free-alginate can not form Ca-alginate complexes. This occurrence depends on the availability of crosslinking sites in free-alginate, which is in turn affected by alginate composition (DAVIDOVICH-PINHAS & BIANCO-PELED, 2010). Since not affecting the general formulation and not related with computational challenges, it is here chosen $\alpha \in [0,1]$. Hence, it also results $C_a = C_A - C_g = C_A(1-\alpha)$.

[1] It is noteworthy that:

$$\frac{\mathrm{D}}{\mathrm{D}t}\int_{\mathcal{P}_t} c_\beta dv = \frac{\mathrm{D}}{\mathrm{D}t}\int_{\mathcal{P}_o} C_\beta dV = \int_{\mathcal{P}_o} \dot{C}_\beta dV\,. \tag{3.5}$$

Pulling-back Eq. (3.4c), the right-hand side (with Eq. (3.7), $c_a = C_A(1-\alpha)/J$ and $c_c = C_c/J$) reads:

$$\int_{\mathcal{R}_t} k\, c_a\, c_c (c_a + c_g)\, dv = \int_{\mathcal{R}_o} k\, C_A \frac{1-\alpha}{J}\, \frac{C_c}{J} \overbrace{(c_a + c_g) J}^{C_A}\, dV\,. \tag{3.9}$$

Then, by using the localization theorem and dividing by $C_A(\mathbf{X})$, Eq. (3.4c) thus leads to (since $\dot{\alpha} = \dot{C}_g/C_A$):

$$\dot{\alpha} = \frac{K C_c}{J^2 C_A}(1-\alpha)\,, \tag{3.10}$$

where $K = kC_A^2 > 0$ is a first-order reaction rate parameter.
In conclusion, under the assumption of low free-alginate mobility, the model by MIKKELSEN & ELGSAETER (1995) reduces to a single balance equation for the calcium concentration which, formulated in the reference configuration, reads:

$$\dot{C}_c = -\nabla_{\mathbf{x}} \cdot (J\mathbf{F}^{-1}\mathbf{j}_c) + R_c\,, \quad \text{with} \;\; R_c = -N_c C_A \dot{\alpha}\,. \tag{3.11}$$

The rate of gelation degree $\dot{\alpha}$ will be formulated in agreement with Eq. (3.10). The latter has been derived from the crosslinking model of MIKKELSEN & ELGSAETER (1995), but it accounts for the effects of medium deformation. The latter has been derived from the crosslinking model by MIKKELSEN & ELGSAETER (1995) corresponding to the one in Eqs. (2.3), and (2.3), but it accounts for the effects of medium deformation. The reaction kinetics speed up when $J < 1$ (i.e., shrinking) and decreases when $J > 1$ (i.e., swelling) due to a variation of the spatial concentration values. Moreover, the crosslinking reaction model will be further extended on the basis of thermodynamic arguments that derive from chemo-mechanical coupling effects.

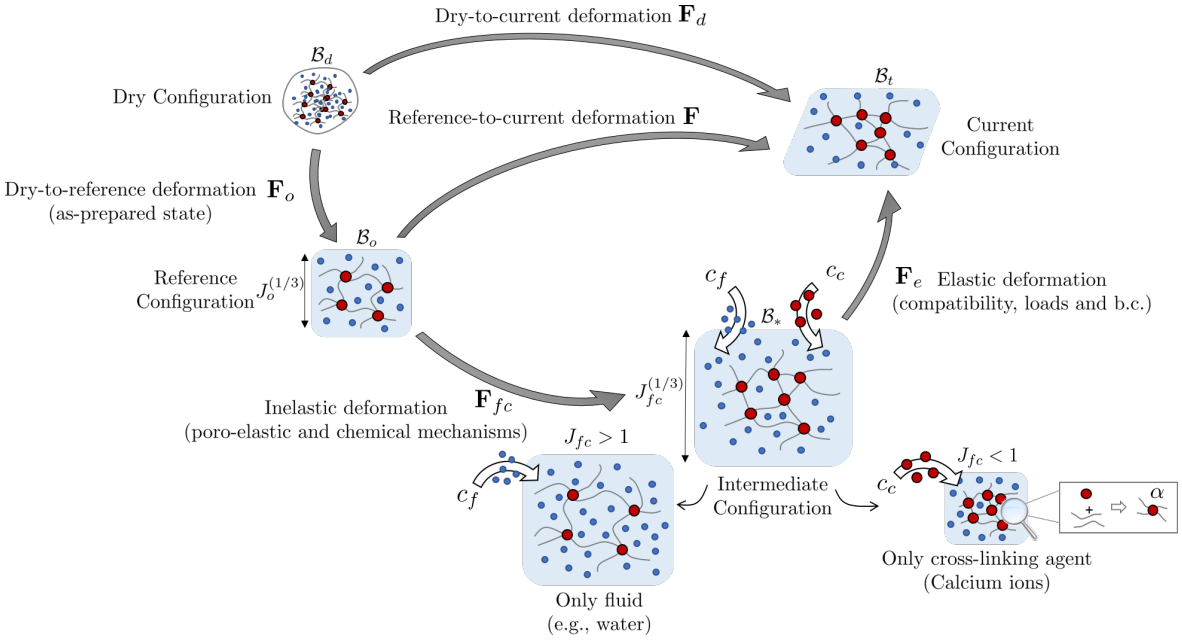

Figure 3.1: Schematic representation of the configurations: dry $\mathcal{B}_d$, reference $\mathcal{B}_o$, intermediate $\mathcal{B}_*$, current $\mathcal{B}_o$, along with the multiplicative decomposition of the deformation gradients: dry-to-current $\mathbf{F}_d$, dry-to-reference $\mathbf{F}_o$, reference-to-current $\mathbf{F}$, inelastic $\mathbf{F}_{fc}$, elastic $\mathbf{F}_e$.

3.2 Chemo-mechanical kinematical effects

The proposed chemo-mechanical theory couples crosslinking chemical reaction kinetics with poroelastic effects associated with swelling of elastomeric materials. To this aim, the following set of state variables is introduced:

$$\mathcal{S} = \{\mathbf{u}(\mathbf{X},t), C_f(\mathbf{X},t), C_c(\mathbf{X},t), \alpha(\mathbf{X},t)\}\,. \tag{3.12}$$

In $\mathcal{B}_o$, non-zero reference values of fluid concentration $C_f|_{\mathcal{B}_o} = C_{fo}$ and gelation degree $\alpha|_{\mathcal{B}_o} = \alpha_o$ are considered, while it results $\mathbf{u}|_{\mathcal{B}_o} = \mathbf{0}$ by definition and it is assumed null free calcium ions, that is $C_c|_{\mathcal{B}_o} = 0$.
The mapping from the dry (non-crosslinked) configuration $\mathcal{B}_d$ to the reference configuration $\mathcal{B}_o$ is locally described by an isotropic dry-to-reference deformation gradient $\mathbf{F}_o$ (Fig. 3.1):

$$\mathbf{F}_o = J_o^{1/3}\mathbf{I} = (J_{eo}J_{so})^{1/3}\mathbf{I}\,, \tag{3.13}$$

with $J_o = J_{eo}J_{so}$ representing the volume change from the dry polymer to the reference configuration. The dry-to-reference volume change is in turn split in two contributions: $J_{eo} > 0$, representing the dry-to-reference elastic volume change associated with a slight compressibility of the polymer network; $J_{so} > 0$, being the swelling volume change, defined as:

$$J_{so} = 1 + \Lambda(\alpha_o)C_{fo}^d - \Gamma\alpha_o\,, \tag{3.14}$$

which is affected by the reference fluid content $C_{fo}^d = J_o C_{fo}$ (expressed per unit of dry polymer), and the initial gelation degree α_o. Function $\Lambda(\alpha)$ is a gelation-dependent fluid

molar volume function:

$$\Lambda(\alpha) = (1-\alpha)\Lambda_0 + \alpha\Lambda_1, \tag{3.15}$$

with Λ_0, Λ_1 being two model parameters representing the reference values respectively at $\alpha = 0$ and $\alpha = 1$, with $\Lambda_0 > \Lambda_1$. Furthermore, $\Gamma \geq 0$ is a constant that describes the volume shrinking due to egg-box Ca-alginate complexes' formation. It is noteworthy that the effect of gelation is twofold: a reduced swelling capacity modeled through $\Lambda(\alpha)$ (indirect shrinking), and a contraction of the polymer network (direct shrinking). The reference configuration and the characterization of J_{eo} and J_{so} in terms of hydrogel composition will be discussed in Section 3.9 in terms of the *as-prepared* state.

The mapping from the reference $\mathcal{B}_o$ to the current $\mathcal{B}_t$ configuration is described by a standard multiplicative decomposition of the reference-to-current deformation gradient $\mathbf{F}$ (GURTIN ET AL., 2010; CHESTER & ANAND, 2011; SAIN ET AL., 2018) into an *inelastic* $\mathbf{F}_{fc}$ and an *elastic* $\mathbf{F}_e$ component (Fig. 3.1),

$$\mathbf{F} = \mathbf{F}_e\mathbf{F}_{fc}\,, \tag{3.16}$$

where considering an isotropic polymer network, it is introduced

$$\mathbf{F}_{fc} = J_{fc}^{1/3}\mathbf{I} \quad \text{with} \quad J_{fc} > 0, \tag{3.17a}$$

$$\mathbf{F}_e = \mathbf{F}\mathbf{F}_{fc}^{-1} = J_{fc}^{-1/3}\mathbf{F}\,. \tag{3.17b}$$

The inelastic deformation gradient $\mathbf{F}_{fc}$ describes kinematic effects due to diffusive-reactive mechanisms of the chemical species, that is the kinematics of the polymer network due to fluid content movements and reaction kinetics with respect to the reference state. In a material point, the influx of fluid induces swelling, while the increase of the gelation degree is associated with a shrinking of the polymer network. Accordingly, the inelastic volume change J_{fc} is defined as a function of fluid concentration C_f and gelation degree α by:

$$J_{fc}(C_f, \alpha) = 1 + J_{so}^{-1}\left[J_o(\Lambda(\alpha)C_f - \Lambda(\alpha_o)C_{fo}) - \Gamma(\alpha - \alpha_o)\right]\,, \tag{3.18}$$

such that the total dry-to-current volume change (with Eq. (3.14)),

$$\begin{aligned}\Delta V_{tot} = J_d = J_oJ_eJ_{fc} &= J_{eo}J_e\left[J_{so} + \Lambda(\alpha)C_f^d - \Lambda(\alpha_o)C_{fo}^d - \Gamma(\alpha-\alpha_o)\right] = \\ &= J_{eo}J_e\left[1 + \Lambda(\alpha)C_f^d - \Gamma\alpha\right]\,,\end{aligned} \tag{3.19}$$

results to be a superposition of an elastic contribution and a swelling component depending on the total fluid content $C_f^d = J_oC_f$ (expressed per unit of dry polymer) and the final gelation degree α.

For the following derivations, it is convenient to obtain from Eq. (3.18) the rate of inelastic volume change $\dot{J}_{fc}$, yielding:

$$\dot{J}_{fc} = \Lambda(\alpha)J_{eo}\dot{C}_f - \hat{\Gamma}(\alpha, C_f)\dot{\alpha}, \;\; \text{with} \;\; \hat{\Gamma}(\alpha, C_f) = J_{so}^{-1}\Gamma - J_{eo}\frac{\partial\Lambda}{\partial\alpha}C_f. \tag{3.20}$$

and to manipulate the spatial velocity gradient $\mathbf{L} = \nabla_{\mathbf{x}}\dot{\mathbf{x}} = \dot{\mathbf{F}}\mathbf{F}^{-1}$ as:

$$\mathbf{L} = \left(\mathbf{F}_e\mathbf{F}_{fc}\right)^{\cdot}\left(\mathbf{F}_e\mathbf{F}_{fc}\right)^{-1} = \mathbf{L}_e + \mathbf{F}_e\mathbf{L}_{fc}\mathbf{F}_e^{-1}\,, \tag{3.21}$$

with $\mathbf{L}_e = \dot{\mathbf{F}}_e \mathbf{F}_e^{-1}$ and $\mathbf{L}_{fc} = \dot{\mathbf{F}}_{fc} \mathbf{F}_{fc}^{-1}$.
Finally, the total dry-to-current deformation is described in terms of the total right Cauchy-Green deformation tensor $\mathbf{C}_d = \mathbf{F}_d^T \mathbf{F}_d$, yielding:

$$\mathbf{C}_d = (J_o J_{fc}(C_f, \alpha))^{2/3} \mathbf{C}_e \,, \tag{3.22}$$

where $\mathbf{C}_e = \mathbf{F}_e^T \mathbf{F}_e$ is the elastic contribution.

3.3 Balance of linear and angular momentum

The local form of the balance of linear momentum in the current configuration reads:

$$\nabla_{\mathbf{x}} \cdot \boldsymbol{\sigma} + \mathbf{b} = \mathbf{0} \;\text{ in }\; \mathcal{B}_t \quad \text{with} \quad \boldsymbol{\sigma}\mathbf{n} = \mathbf{t} \;\text{ on }\; \Sigma_t \,, \tag{3.23}$$

where $\boldsymbol{\sigma}$ is the Cauchy stress tensor (symmetric from the balance of angular momentum), $\mathbf{b}$ is the body force per unit deformed volume, and $\mathbf{t}$ is the external surface traction per unit deformed area applied on boundary $\Sigma_t \subseteq \partial\mathcal{B}_t$ with outward unit normal $\mathbf{n}$. On the portion $\Sigma_u = \partial\mathcal{B}_t \setminus \Sigma_t$ of the external surface, constraints on the displacement field $\mathbf{u}$ are considered. Due to the considerable long time scale of fluid diffusion compared to the mechanical waves propagation, inertial effects have been neglected (GURTIN ET AL., 2010).

3.4 Material (mole) balance

Fluid (subscript $\beta = f$) and calcium (subscript $\beta = c$) concentrations shall obey material balance equations. For calcium this is represented by the reaction-diffusion equation (3.11) obtained from the chemical model described in Section 3.1. On the other hand, fluid content is considered to be purely diffusive (null reaction term). In a Lagrangian description, the local form of the material (mole) balance equations in the reference configuration read:

$$\dot{C}_f = -\nabla_{\mathbf{X}} \cdot \mathbf{J}_f \,, \tag{3.24a}$$

$$\dot{C}_c = -\nabla_{\mathbf{X}} \cdot \mathbf{J}_c + R_c \,, \tag{3.24b}$$

with $\mathbf{J}_f$ and $\mathbf{J}_c$ being fluxes in the reference configuration, pulled back from the spatial configuration (i.e., $\mathbf{J}_\beta = J\mathbf{F}^{-1}\mathbf{j}_\beta$), and R_c is given in Eq. (3.11). The crosslinking reaction rate $\dot{\alpha}$ in Eq. (3.11) will be defined on the basis of the following thermodynamics arguments and such to agree with the crosslinking relation in Eq. (3.10) derived from the model by MIKKELSEN & ELGSAETER (1995) .

3.5 Second law of thermodynamics

Following standard thermodynamic arguments (WRIGGERS, 2008; GURTIN ET AL., 2010; HOLZAPFEL, 2000), the local form of the second law of thermodynamics (in material

description) accounting for mechanical stress power and chemical potentials of reactive-diffusive chemical species reads:

$$\mathbf{P} : \dot{\mathbf{F}} + \mu_f \dot{C}_f + \mu_c \dot{C}_c - \mathbf{J}_f \cdot \nabla_{\mathbf{X}} \mu_f - \mathbf{J}_c \cdot \nabla_{\mathbf{X}} \mu_c - \dot{\Psi} \geq 0 \,. \tag{3.25}$$

Here, $\mathbf{P} = J\boldsymbol{\sigma}\mathbf{F}^{-T}$ is the first Piola-Kirchhoff stress tensor, μ_f and μ_c denote respectively the chemical potentials of fluid and calcium, and $\dot{\Psi}$ is the rate of the Helmholtz free energy density Ψ per unit reference volume. Since the reference-to-current volume change results $J = J_e J_{fc}$, and by using Eq. (3.21) and $\mathbf{C}_e = \mathbf{F}_e^T \mathbf{F}_e$, the stress-power is conveniently reformulated as[2]:

$$\mathbf{P} : \dot{\mathbf{F}} = J\boldsymbol{\sigma} : \mathbf{L} = \frac{1}{2} J_{fc} \mathbf{S}_e : \dot{\mathbf{C}}_e + J_{fc} \mathbf{M}_e : \mathbf{L}_{fc} \,, \tag{3.26}$$

where $\mathbf{S}_e$ and $\mathbf{M}_e$ are the second Piola-Kirchhoff stress tensor and the Mandel stress tensor in the intermediate configuration, respectively,

$$\mathbf{S}_e \overset{\text{def}}{=} J_e \mathbf{F}_e^{-1} \boldsymbol{\sigma} \mathbf{F}_e^{-T} \,, \qquad \mathbf{M}_e \overset{\text{def}}{=} \mathbf{C}_e \mathbf{S}_e = J_e \mathbf{F}_e^T \boldsymbol{\sigma} \mathbf{F}_e^{-T} \,. \tag{3.27}$$

Given Eq. (3.17a), it results $\dot{\mathbf{F}}_{fc} = \dot{J}_{fc} J_{fc}^{2/3} \mathbf{I}/3$ which yields $\mathbf{L}_{fc} = \dot{J}_{fc} J_{fc}^{-1} \mathbf{I}/3$ and

$$J_{fc} \mathbf{M}_e : \mathbf{L}_{fc} = \dot{J}_{fc} \frac{\mathbf{M}_e : \mathbf{I}}{3} = -\dot{J}_{fc} \bar{p} \,, \tag{3.28}$$

where $\bar{p} = J_e p$, with $p = -\mathrm{Tr}(\boldsymbol{\sigma})/3$, is the hydrostatic pressure in the intermediate configuration. Accordingly, the second law of thermodynamics reads (Eq. (3.25)):

$$\frac{1}{2} J_{fc} \mathbf{S}_e : \dot{\mathbf{C}}_e + \mu_f \dot{C}_f + \mu_c \dot{C}_c - \dot{J}_{fc} \bar{p} - \sum_{\beta = f,c} \mathbf{J}_\beta \cdot \nabla_{\mathbf{X}} \mu_\beta - \dot{\Psi} \geq 0 \,, \tag{3.29}$$

and, accounting for the kinematic choice on $\dot{J}_{fc}$ in Eq. (3.20), as:

$$\frac{1}{2} J_{fc} \mathbf{S}_e : \dot{\mathbf{C}}_e + \left(\mu_f - \Lambda J_{eo} \bar{p}\right) \dot{C}_f + \mu_c \dot{C}_c + \hat{\Gamma} \bar{p} \dot{\alpha} - \sum_{\beta = f,c} \mathbf{J}_\beta \cdot \nabla_{\mathbf{X}} \mu_\beta - \dot{\Psi} \geq 0 \,. \tag{3.30}$$

3.6 Constitutive model

The free-energy is postulated to depend on the elastic deformation (through $\mathbf{C}_e$), concentrations C_c and C_f, as well as gelation degree α, namely

$$\Psi = \Psi(\mathbf{C}_e, C_f, C_c, \alpha) \,. \tag{3.31}$$

[2] It results in:

$$\begin{aligned} \boldsymbol{\sigma} : \mathbf{L} &= \boldsymbol{\sigma} : \mathbf{L}_e + \boldsymbol{\sigma} : \left(\mathbf{F}_e \mathbf{L}_{fc} \mathbf{F}_c^{-1}\right) = \boldsymbol{\sigma} : \left(\dot{\mathbf{F}}_e \mathbf{F}_e^{-1}\right) + \mathbf{F}_e^T \boldsymbol{\sigma} \mathbf{F}_e^{-T} : \mathbf{L}_{fc} = \\ &= \frac{1}{2} \mathbf{F}_e^{-1} \boldsymbol{\sigma} \mathbf{F}_e^{-T} : \dot{\mathbf{C}}_e + J_e^{-1} \mathbf{M}_e : \mathbf{L}_{fc} = \frac{1}{2} J_e^{-1} \mathbf{S}_e : \dot{\mathbf{C}}_e + J_e^{-1} \mathbf{M}_e : \mathbf{L}_{fc}, \end{aligned}$$

Considering the rate of the free-energy Ψ,

$$\dot{\Psi}(\mathbf{C}_e, C_f, C_c, \alpha) = \frac{\partial \Psi}{\partial \mathbf{C}_e} : \dot{\mathbf{C}}_e + \sum_{\beta=f,c} \frac{\partial \Psi}{\partial C_\beta} \dot{C}_\beta + \frac{\partial \Psi}{\partial \alpha} \dot{\alpha}\,, \tag{3.32}$$

Eq. (3.30) yields,

$$\begin{aligned} &\left(\frac{1}{2} J_{fc} \mathbf{S}_e - \frac{\partial \Psi}{\partial \mathbf{C}_e}\right) : \dot{\mathbf{C}}_e + \left(\mu_f - \Lambda J_{eo} \bar{p} - \frac{\partial \Psi}{\partial C_f}\right) \dot{C}_f + \\ &+ \left(\mu_c - \frac{\partial \Psi}{\partial C_c}\right) \dot{C}_c + \left(\hat{\Gamma} \bar{p} - \frac{\partial \Psi}{\partial \alpha}\right) \dot{\alpha} - \sum_\beta \mathbf{J}_\beta \cdot \nabla_{\mathbf{X}} \mu_\beta \geq 0\,. \end{aligned} \tag{3.33}$$

It is thus convenient to introduce the fluid active chemical potential μ_f^{act},

$$\mu_f^{act} = \mu_f - \Lambda J_{eo} \bar{p}, \tag{3.34}$$

and the affinity term A_α for the calcium-driven reaction,

$$A_\alpha = \hat{\Gamma} \bar{p} - \frac{\partial \Psi}{\partial \alpha}\,. \tag{3.35}$$

The following constitutive choices are then introduced:

$$\mathbf{S}_e = 2 J_{fc}^{-1} \frac{\partial \Psi}{\partial \mathbf{C}_e}\,, \tag{3.36a}$$

$$\mu_f^{act} = \frac{\partial \Psi}{\partial C_f} \quad \Rightarrow \quad \mu_f = \frac{\partial \Psi}{\partial C_f} + \Lambda J_{eo} \bar{p}\,, \tag{3.36b}$$

$$\mu_c = \frac{\partial \Psi}{\partial C_c}\,, \tag{3.36c}$$

$$\mathbf{j}_\beta = -c_\beta m_\beta \nabla_{\mathbf{x}} \mu_\beta \quad \text{for} \quad \beta = f, c \tag{3.36d}$$

In particular, Eq. (3.36d) is a well-established transport equation which correlates molecular flux in the current configuration with a mobility parameter $\bar{m}_\beta$, the availability of molecules (term c_β), and the gradient of chemical potential. Since $\nabla_{\mathbf{x}} \mu_\beta = \mathbf{F}^{-T} \nabla_{\mathbf{X}} \mu_\beta$ Eq. (3.36d) reads in the reference configuration,

$$\mathbf{J}_\beta = -J \mathbf{F}^{-1} (c_\beta \bar{m}_\beta \mathbf{F}^{-T} \nabla_{\mathbf{X}} \mu_\beta) = -C_\beta \bar{m}_\beta \mathbf{C}^{-1} \nabla_{\mathbf{X}} \mu_\beta, \tag{3.37}$$

and $\mathbf{J}_\beta \cdot \nabla_{\mathbf{X}} \mu_\beta \propto -\|\mathbf{F}^{-T} \nabla_{\mathbf{X}} \mu_\beta\|^2$, hence resulting $(-\mathbf{J}_\beta \cdot \nabla_{\mathbf{X}} \mu_\beta) \geq 0$.
Finally, the evolution equation for the gelation degree is chosen as:

$$\dot{\alpha} = \left(\frac{K C_c}{\kappa_\alpha J^2 C_A}\right) A_\alpha = \left(\frac{K C_c}{\kappa_\alpha J^2 C_A}\right) \left(\hat{\Gamma} \bar{p} - \frac{\partial \Psi}{\partial \alpha}\right), \tag{3.38}$$

where the chemo-mechanical coupling modulus $\kappa_\alpha > 0$ characterizes the influence of the hydrostatic pressure on the extent of the reaction and it has the unit of a stress. The choice in Eq. (3.38) will become clear in the following Section 3.8, where the free-energy term will be specialized to recover the chemical crosslinking model described in Section 3.1. At the moment, it is noteworthy that Eq. (3.38) yields $A_\alpha \dot{\alpha} \propto A_\alpha^2$, resulting $A_\alpha \dot{\alpha} \geq 0$.
Overall, choices in Eqs. (3.36) and (3.38) allow to satisfy *a priori* the dissipation inequality in Eq. (3.33).

3.7 Free-Energy definition

The total free-energy density (per unit reference volume) is specialized as

$$\Psi(\mathbf{C}_e, C_f, C_c, \alpha) = \Psi_{mech}(\mathbf{C}_e, C_f, \alpha) + \Psi_{ch}(C_f, C_c) + \Psi_{\alpha}(\alpha)\,, \tag{3.39}$$

where Ψ_{mech} represents the mechanical contribution, Ψ_{ch} the contribution from the mixing of the chemical species, and Ψ_{α} the crosslinking reaction term. Note that, the free energy can be specialized for specific applications by imposing different constitutive assumptions. Following well-established approaches, the free-energy density has been written in a separable form by considering an additive decomposition between mixing, mechanical and chemical reaction parts (FLORY & ERMAN, 1982; CHESTER & ANAND, 2011; SAIN ET AL., 2018). Due to coupled functional dependencies between the single energy terms, the adopted additive decomposition of the free-energy does not lead to a simple superposition of the effects of the different fields.

The mechanical free-energy density Ψ_{mech} of the hydrogel is assumed to depend on the total (dry-to-current) deformation gradient $\mathbf{F}_d$ since swelling-induced volume changes have elastic effects, contrarily to other types of inelastic deformations like plasticity or thermal expansion. Term Ψ_{mech} is introduced by coupling an energetic contribution with an entropic term based on Gaussian statistics for moderate deformation (CHESTER & ANAND, 2011):

$$\Psi_{mech}(\mathbf{C}_e, C_f, \alpha) = \overbrace{\Psi_{en}(\mathbf{C}_e, \alpha)}^{\text{energetic}} + \overbrace{\frac{G_p(\alpha)}{2}\left(\text{Tr}(\mathbf{C}_d) - 3\right) - G_p(\alpha)\ln(J_d)}^{\text{entropic}}\,, \tag{3.40}$$

where $\mathbf{C}_d$ is the total (dry-to-current) right Cauchy-Green deformation gradient and $J_d = (J_o J_{fc}(C_f, \alpha))^{1/3}(\text{Det}(\mathbf{C}_e))^{1/2}$ is the total (dry-to-current) volume change (see Eq. (3.22)). The following choice on Ψ_{en} is made :

$$\Psi_{en}(\mathbf{C}_e, \alpha) = \frac{\kappa_p(\alpha)}{2}\left(\frac{J_{eo}J_e^2}{2} - \frac{\ln(J_e)}{J_{eo}} - \frac{J_{eo}}{2}\right)\,, \tag{3.41}$$

depending on the total (dry-to-current) elastic contributions (i.e., J_{eo} and J_e), such that the resulting stress quantity σ_{en},

$$\sigma_{en} = \frac{\partial \Psi_{en}}{\partial J_e} = \frac{\kappa_p}{2}\left(\frac{(J_{eo}J_e)^2 - 1}{J_{eo}J_e}\right)\,, \tag{3.42}$$

enforces quasi-incompressibility ($\sigma_{en} \to 0 \iff J_{eo}J_e \to 1$) and avoids volume annihilation and infinite growth (if $J_{eo}J_e \to 0$ or $J_{eo}J_e \to \infty$, then $\sigma_{en} \to +\infty$) for the elastic part of the deformation.

Introducing the second Piola–Kirchhoff stress (in the intermediate configuration) tensor from Eq. (3.36a), it gives

$$\begin{aligned}
\mathbf{S}_e &= 2J_{fc}^{-1}\frac{\partial \Psi}{\partial \mathbf{C}_e} \\
&= 2J_{fc}^{-1}(\mathbb{I} - \frac{1}{3}\mathbf{C}_e^{-1} \otimes \mathbf{C}_e)\frac{\partial \Psi}{\partial \mathbf{C}_e} + J_e\frac{\partial \Psi}{\partial J_e}\mathbf{C}_e^{-1} \\
&= \frac{2}{J_{fc}}\big[\frac{\partial \Psi}{\partial \mathbf{C}_e} - \frac{1}{3}\big(\mathbf{C}_e : \frac{\partial \Psi}{\partial \mathbf{C}_e}\big)\mathbf{C}_e^{-1}\big] + J_e\frac{\partial \Psi}{\partial J_e}\mathbf{C}_e^{-1}\,,
\end{aligned} \tag{3.43}$$

Next by using Eq. (3.43), the first Piola–Kirchhoff stress tensor has the form

$$\begin{aligned}\mathbf{P} &= \mathbf{F}_e\mathbf{S}_e \\ &= \frac{2}{J_{fc}}\big[\mathbf{F}_e\frac{\partial\Psi}{\partial\mathbf{C}_e} - \frac{1}{3}\big(\mathbf{C}_e\colon\frac{\partial\Psi}{\partial\mathbf{C}_e}\big)\mathbf{F}_e^{-T}\big] + J_e\frac{\partial\Psi}{\partial J_e}\mathbf{F}_e^{-T}\,.\end{aligned} \tag{3.44}$$

Furthermore, utilizing Eq. (3.44) the Cauchy stress can be formulated as follows

$$\begin{aligned}\boldsymbol{\sigma} &= J_e^{-1}\mathbf{P}\mathbf{F}_e^T \\ &= \frac{2}{J_{fc}J_e}\big[\mathbf{F}_e\frac{\partial\Psi}{\partial\mathbf{C}_e}\mathbf{F}_e^T - \frac{1}{3}\big(\mathbf{C}_e\colon\frac{\partial\Psi}{\partial\mathbf{C}_e}\big)\mathbf{I}\big] + \frac{\partial\Psi}{\partial J_e}\mathbf{I}\,,\end{aligned} \tag{3.45}$$

further in detail description can be found by GURTIN ET AL. (2010).
In Eqs. (3.40) and (3.41), material parameters G_p and κ_p respectively represent the ground-state shear modulus of the hydrogel and the ground-state bluk modulus of the polymer network. In order to account for crosslinking effects on polymer mechanics, G_p is assumed to be gelation-dependent, i.e.

$$G_p(\alpha) = (1-\alpha)G_p^0 + \alpha G_p^1\,, \tag{3.46}$$

where G_p^0, G_p^1 are the shear moduli of the polymer network (for $\alpha = 0$) and the one of a fully cross-linked gel (for $\alpha = 1$), with $G_p^1 > G_p^0$. As a consequence of Eq. (3.46), also the bulk modulus is assumed to be gelation-dependent, i.e. $\kappa_p = \kappa_p(\alpha)$, namely:

$$\kappa_p(\alpha) = \frac{2G_p(\alpha)(1+\nu_p)}{3(1-2\nu_p)}\,, \tag{3.47}$$

where ν_p is a model parameter representing a measure of the Poisson's ratio of the polymer network.
The chemical free-energy density per unit reference volume accounting for the mixing of chemical species is defined as,

$$\Psi_{ch}(C_f, C_c) = \bar{\mu}_f C_f + \bar{\mu}_c C_c + \overbrace{RT\sum_{\beta=f,c,p} C_\beta \ln\left(m_\beta(C_f,C_c)\right)}^{\text{entropy}} + \overbrace{RT\frac{\chi}{\bar{\Lambda}}\frac{v_p v_f(C_f)}{v_p + v_f(C_f)}}^{\text{enthalphy}}\,, \tag{3.48}$$

where $\bar{\mu}_f$ and $\bar{\mu}_c$ are reference chemical potentials of fluid (f) and calcium (c), R is the universal gas constant, T the absolute temperature, and m_β the mole fraction of chemical species β:

$$m_\beta(C_f, C_c) = \frac{C_\beta}{C_f + C_c + C_p}\,. \tag{3.49}$$

Here, C_p represents polymer molar concentration in the reference configuration. Both free-alginate and gel are comprised within C_p, resulting $C_p = C_A$ (constant in time and space) in agreement with Eq. (3.6). The enthalpy term in Eq. (3.48) is introduced for the fluid-polymer mixing in agreement with the Flory-Huggins theory. This term depends on: the dimensionless parameter χ, proportional to the dis-affinity between the polymer and the

fluid; fluid volume per unit reference volume v_f which is defined as $v_f(C_f) = \bar{\Lambda} C_f$, with $\bar{\Lambda}$ being a reference fluid molar volume in the polymer (see Table 3.1); and the polymer volume fraction v_p (per unit reference volume) which will be related to hydrogel composition and reference conditions in the following Section 3.9 (see Eq. (3.65)). It is pointed out that the amount of calcium is considered negligible for the mixing enthalpy.
Finally, the gelation reaction free-energy term Ψ_α is (SAIN ET AL., 2018)

$$\Psi_\alpha(\alpha) = \frac{\kappa_\alpha}{2}(\alpha - 1)^2 \,. \tag{3.50}$$

3.8 Resulting chemo-mechanical thermodynamic quantities

Introducing Eq. (3.48) into Eqs. (3.36b) and (3.36c), the chemical potential expressions result:

$$\mu_f = \overbrace{\bar{\mu}_f + RT\ln\left(m_f(C_f, C_c)\right)}^{\text{entropy}} + \overbrace{RT\chi\left(\frac{v_p}{v_p + v_f(C_f)}\right)^2}^{\text{enthalpy}} + \overbrace{\mu_f^\sigma(\mathbf{C}_e, \alpha)}^{\text{mech.}} \,, \tag{3.51a}$$

$$\mu_c = \underbrace{\bar{\mu}_c + RT\ln\left(m_c(C_f, C_c)\right)}_{\text{entropy}} \,, \tag{3.51b}$$

where $\mu_f^\sigma = \Lambda J_{eo} \bar{p}$. The expressions obtained in Eq. (3.51) motivate the choice of the chemical free-energy term Ψ_{ch} in Eq. (3.48): the potential of the chemical species is described in terms of an entropy mixing term for ideal solutions which, for the fluid, is corrected with a Flory-Huggins enthalpy term and with a poroelastic coupling quantity. It is noteworthy that in general it results $\mu_f = \mu_f(\mathbf{C}_e, C_f, C_c, \alpha)$ and $\mu_c = \mu_c(C_f, C_c)$.
From Eq. (3.37), fluid flux reads:

$$\mathbf{J}_f = -C_f \mathbf{D}_f \nabla_{\mathbf{X}} \mu_f \,, \tag{3.52}$$

where $\mathbf{D}_f = \bar{D}_f J \mathbf{C}^{-1}$ and $\bar{D}_f = RT\bar{m}_f$ is the diffusivity of the fluid content. In order to account for obstruction effects (AMSDEN, 1998), $\bar{D}_f$ is defined as a linear function of the crosslinking degree α, that is

$$\bar{D}_f(\alpha) = D_f^0(1 - \alpha) + D_f^1 \alpha, \tag{3.53}$$

with D_f^0, D_f^1 being respectively values at $\alpha = 0$ and at $\alpha = 1$, with $D_f^0 > D_f^1$ (SALAHSHOOR & RAHBAR, 2014). Furthermore, the flux of calcium hence results from Eq. (3.37),

$$\mathbf{J}_c = -C_c \mathbf{D}_c \nabla_{\mathbf{X}} \mu_c \,, \tag{3.54}$$

where $\mathbf{D}_c = \bar{D}_c J \mathbf{C}^{-1}$ with $\bar{D}_c = RT\bar{m}_c$. Analogously to $\bar{D}_f$, also calcium diffusivity $\bar{D}_c$ is assumed to depend on α and introduced as in Eq. (3.55), relationship validated on the basis of the experimental-modeling activity in Chapter 2 (HAJIKHANI ET AL., 2019),

$$\bar{D}_c(\alpha) = D_c^0 + (D_c^1 - D_c^0)\frac{\mathrm{Exp}(-n\alpha/\alpha_{\text{gel}}) - 1}{\mathrm{Exp}(-n/\alpha_{\text{gel}})} \,, \tag{3.55}$$

with D_c^0, D_c^1 being respectively values at $\alpha = 0$ and $\alpha = 1$ (with $D_c^0 > D_c^1$), n a model parameter governing the rate of calcium diffusivity change and α_{gel} the gelation point (i.e., the gelation degree when the gel exhibits a solid-like response). It is noteworthy that, inserting Eq. (3.51b) into Eq. (3.37), the first Fick's law can be recovered under the assumption of low relative calcium concentration $r_c = C_c/(C_p + C_f) \to 0$, that is:

$$\begin{aligned} \lim_{r_c \to 0} \mathbf{J}_c &= \lim_{r_c \to 0} -C_c \mathbf{D}_c \nabla_{\mathbf{X}} \mu_c = \\ &= \mathbf{D}_c \lim_{r_c \to 0} - \left(\frac{1}{1+r_c} \nabla_{\mathbf{X}} C_c - \frac{r_c}{1+r_c} \nabla_{\mathbf{X}} C_f \right) = -\mathbf{D}_c \nabla_{\mathbf{X}} C_c \,. \end{aligned} \tag{3.56}$$

Finally, introducing Eq. (3.50) in Eq. (3.35), the affinity reads:

$$A_\alpha = \hat{\Gamma} \bar{p} - \frac{\partial \Psi}{\partial \alpha} = \kappa_\alpha (1 - \alpha) + \hat{p} \,, \tag{3.57}$$

where $\hat{p} = \hat{\Gamma} \bar{p} - \partial \Psi_{mech} / \partial \alpha$ is a generalized pressure-like term that accounts for the effect of mechanics on the chemical reaction, resulting (since $G_p^1 > G_p^0$ and $\Lambda_0 > \Lambda_1$):

$$\hat{p} = \hat{\Gamma} \bar{p} + \frac{\partial \Psi_{mech}}{\partial \alpha} = \left[J_{so}^{-1} \Gamma + J_{eo} C_f (\Lambda_0 - \Lambda_1) \right] \bar{p} + (G_p^1 - G_p^0) \frac{\partial \Psi_{mech}}{\partial G_p} \,. \tag{3.58}$$

Therefore, the evolution equation in Eq. (3.38), together with the physical requirement on the definition of α (see Eq. (3.8)), yields:

$$\dot{\alpha} = \frac{K C_c}{\kappa_\alpha J^2 C_A} A_\alpha = \frac{K C_c}{J^2 C_A} \left(1 - \alpha + \frac{\hat{p}}{\kappa_\alpha} \right) \quad \text{with } \alpha \in [0, 1] \,. \tag{3.59}$$

When neglecting term $\hat{p}$ (e.g., when modulus $\kappa_\alpha \to +\infty$), the crosslinking kinetics in Eq. (3.59) coincides with the (purely) chemical description in Section 3.1 (see Eq. (3.11)). The direct influence of mechanics revealed by $\hat{p}$ follows thermodynamic requirements, and it is due to the effects of the crosslinking degree on the swelling kinematics (i.e., J_{fc}) and on stiffness constants (i.e., G_p). By accounting only for swelling effects (i.e., $G_p^1 = G_p^0$), the coupling term induces an acceleration of the reaction when $\bar{p} > 0$. This observation agrees with evidence that crosslinking processes in polymers are accelerated by compressive actions (ANNABI ET AL., 2009; BELLANDER ET AL., 1998; MA ET AL., 2015; MAITRA & SHUKLA, 2014; TONPHENG & ANDERSSON, 2008). In the present framework of swollen elastomers, the effect of the coupling term is harder to predict *a priori* since the mechanical energy is always contributing to the acceleration of the reaction despite the sign of the hydrostatic stress ($\partial \Psi_{mech} / \partial G_p \geq 0$ for any deformation state). Therefore, the sign of $\hat{p}$ is highly dependent on the relative values of Γ, Λ_1, Λ_0, and G_p^0, G_p^1, as well as on stresses and strains in the hydrogel. Moreover, its effective impact depends on the value of the chemo-mechanical coupling modulus κ_α for which the experimental identification in the context of hydrogels is, to the best of authors' knowledge, not available. The present study provides a modeling framework that, coupled with *ad hoc* experimental campaigns, clarifies the influence of the (thermodynamically required) chemo-mechanical coupling term crosslinking reaction is significant or not.

Table 3.1: Biophysical properties of polymers and fluid for the definition of hydrogels' composition and as-prepared state. Reference values for alginate(polymer) and water(fluid) are given. The value of $\bar{\Lambda}$ is taken from CHESTER & ANAND (2011).

Definition	**Symbol**	**Value**
Polymer molar weight	W_p	216.12 g/mol
Polymer density	ρ_p	1.6 g/cm^3
Polymer molar volume	Λ_p	$\rho_p^{-1} W_p$ (m^3/mol)
Polymer moles per unit polymer volume	M_p	$1/\Lambda_p$ (mol/m^3)
Fluid molar volume	$\bar{\Lambda}$	10^{-4} m^3/mol
Fluid moles per unit fluid volume	N_f	$1/\bar{\Lambda}$ (mol/m^3)
Room temperature	T	298 K
Universal gas constant	R	8.3145 J/mol

3.9 Reference configuration: as-prepared state

The reference configuration is chosen to coincide with the *as-prepared* state. The preparation of hydrogels is generally characterized in laboratories in terms of fluid (solvent) volume $\bar{V}_{fo}$ and alginate (solute) concentration $\bar{C}_p$ expressed as molar concentration per unit of fluid volume[3]. Starting from assigned values for $\bar{V}_{fo}$ and $\bar{C}_p$ and from basic biophysical properties listed in Table 3.1 (where typical values for alginate hydrogels are given), it is convenient to characterize the as-prepared hydrogel composition in terms of the dry polymer volume $\bar{V}_p = \Lambda_p \bar{C}_p \bar{V}_{fo}$ and the molar concentration of the fluid per unit dry polymer volume $\bar{C}_{fo}^{ap} = N_f \bar{V}_{fo}/\bar{V}_p = N_f M_p/\bar{C}_p$. The crosslinking density α_o in the as-prepared state is here an assigned quantity and its determination on the basis of the specific preparation conditions is not object of present investigation[4].

The as-prepared state is obtained from the dry one by means of an isotropic deformation

[3]Generally, polymer concentration is expressed in terms of weight/volume percentage (% w/v) which can be converted in terms of molar concentration (moles/volume) through the polymer molar weight W_p via the following conversion: 1% w/v = 1 g/(100 ml) = 10^4 g/m^3 =$10^4 W_p^{-1}$ mol/m^3.

[4]An effective strategy for the stabilization of the polymer network in the preparation phase is the internal gelation method (SCHUSTER ET AL., 2014). In the internal gelation method, an insoluble calcium source is dispersed in the alginate solution, followed by the addition of a slowly hydrolysed acid. This gelation approach allows to obtain isotropic polymer networks with an initial crosslinking density, which can be reasonably considered homogenous within the specimen (i.e., $\alpha(\mathbf{X}, 0) = \alpha_o$)

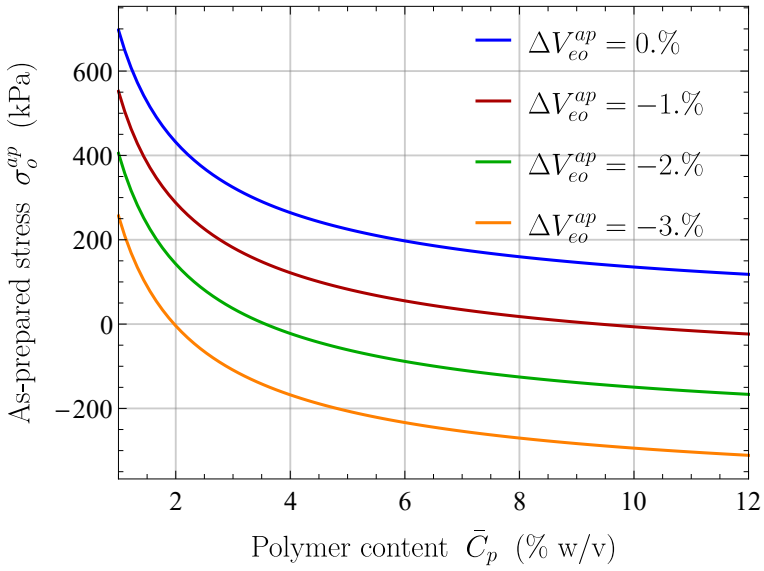

Figure 3.2: As-prepared state. Stress σ_o^{ap} versus polymer content $\bar{C}_p$ for different elastic volume change $\Delta V_{eo}^{ap} = J_{eo}^{ap} - 1$. If not differently specified, parameters' values are given in Table 5.1.

gradient[5] describing the as-prepared state $\mathbf{F}_o^{ap}$, defined as:

$$\mathbf{F}_o = \mathbf{F}_o^{ap} = (J_o^{ap})^{1/3}\mathbf{I}\,, \quad \text{with} \quad J_o^{ap} = J_{eo}^{ap}\overbrace{(1+\Lambda(\alpha_o)\bar{C}_{fo}^{ap} - \Gamma\alpha_o)}^{J_{so}^{ap}}\,, \tag{3.60}$$

where J_{eo}^{ap} is the elastic polymer stretch from the dry to the as-prepared configuration and J_{so}^{ap} the volume change due to the influx of $\bar{C}_{fo}^{ap}$ fluid in the hydrogel network (accounting for the initial crosslinking α_o). Since $\mathbf{F}_o = \mathbf{F}_o^{ap}$, it results $J_{eo}^{ap} = J_{eo}$, $J_{so}^{ap} = J_{so}$ and $\bar{C}_{fo}^{ap} = C_{fo}^{d}$ with respect to quantities in Eqs. (3.13) and (3.14). For a given hydrogel composition, J_{so}^{ap} is a fixed and known quantity, while J_{eo}^{ap} has to be determined. This is determined by enforcing the stress-free condition, such that the as-prepared state satisfies the equilibrium of the balance of linear momentum (3.23) under null applied external loads (gravity loads are neglected). In particular, by assuming the as-prepared state in the reference configuration,

$$\text{AP} = \{\mathbf{F}_o = \mathbf{F}_o^{ap},\ \mathbf{C}_e = \mathbf{I},\ C_f = C_{fo},\ C_c = 0,\ \alpha = \alpha_o\}\,, \tag{3.61}$$

the resulting Cauchy stress tensor obtained from Eq. (3.36a) in the as-prepared state is hydrostatic and depending only on J_{eo}^{ap}, that is $\boldsymbol{\sigma}|_{\text{AP}} = \sigma_o^{ap}(J_{eo}^{ap})\mathbf{I}$ with:

$$\sigma_o^{ap}(J_{eo}^{ap}) = G_p(\alpha_o)\left[(J_{eo}^{ap}J_{so}^{ap})^{2/3} - 1\right] + \kappa_p(\alpha_o)\frac{(J_{eo}^{ap})^2 - 1}{2J_{eo}^{ap}}\,. \tag{3.62}$$

[5] An isotropic deformation gradient is in this step proposed, since, the dry configuration ideally has the same shape of the as-prepared configuration (with various dimensions). The underlying assumptions results in the same polymer chains' stretch in all directions and homogenous within hydrogel domain, constant in space. In particular, the latter presumption will allow to characterize the before-mentioned step from the solution of non-linear algebraic relationship (see Section 3.9).

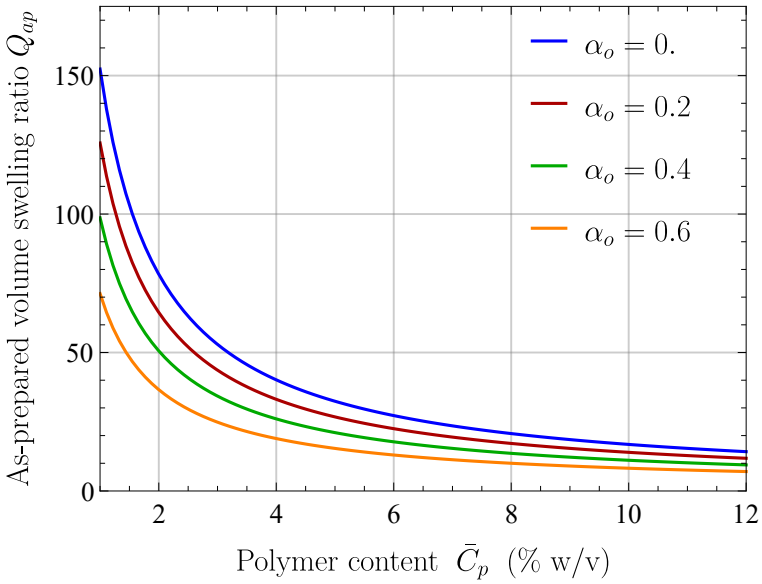

Figure 3.3: As-prepared state. As-prepared volume dilation $Q_{ap} = J_o^{ap}$ (from the dry polymer to the as-prepared state) versus polymer content $\bar{C}_p$ for different initial gelation degree α_o. If not differently specified, the parameter values are taken from Table 5.1.

Therefore, the stress-free condition reads:

$$\text{find } J_{eo}^{ap} \text{ s.t. } \sigma_o^{ap}(J_{eo}^{ap}) = 0\,. \tag{3.63}$$

Results associated with the characterization of the as-prepared state are reported in Fig. 3.2 where, for a given fluid amount $\bar{V}_f$, the variation of the as-prepared stress σ_o^{ap} with polymer content and elastic volume change $\Delta V_{eo}^{ap} = J_{eo}^{ap} - 1$ is reported. The dilation of the polymer network due to fluid content increases the internal stress, which can be compensated by an elastic volume change for restoring the stress-free configuration. The lower the polymer content $\bar{C}_p$, the higher the elastic contribution shall result. By computing J_{eo}^{ap} as in Eq. (3.63), Fig. 3.3 also reports the as-prepared volume dilation J_o^{ap} (from the dry polymer to the as-prepared state), which results inversely proportional to polymer content $\bar{C}_p$ and to the initial gelation degree α_o. These outcomes agree respectively with evidence reported by YAZICI & OKAY (2005), and GIRIDHAR & AKANKSHA (2011).

It is worth highlighting that, in general, the as-prepared state is not at equilibrium from the chemical viewpoint. As a matter of fact, fluid chemical potential μ_f within the hydrogel might not coincide with the one on the exterior μ_f^{ext} and the fluid material balance equation (3.24a) is not satisfied. In detail, μ_f in the as-prepared state is determined by hydrogel composition and the elastic stretch J_{eo}^{ap} obtained from Eq. (3.63), resulting $\mu_f|_{\text{AP}} = \mu_{fo}^{ap}$, with:

$$\mu_{fo}^{ap} = \bar{\mu}_f - \frac{\Lambda(\alpha_o)\kappa_p(\alpha_o)}{2}\left[(J_{eo}^{ap})^2 - 1\right] + RT\left[\ln\left(\frac{C_{fo}^{ap}}{C_{fo}^{ap} + C_p^{ap}}\right) + \chi\left(\frac{v_p}{v_p + \bar{\Lambda} C_{fo}^{ap}}\right)^2\right], \tag{3.64}$$

where $C_{fo}^{ap} = J_o^{-1}\bar{C}_{fo}^{ap}$, $C_p^{ap} = J_o^{-1}\bar{C}_p^{ap}$, and polymer volume fraction v_p in the reference configuration is defined as:

$$v_p = J_{eo}\bar{V}_p/(J_{eo}\bar{V}_p + \bar{V}_{fo})\,. \tag{3.65}$$

This expression accounts for the polymer elastic volume change. The as-prepared state is introduced (and chosen as the reference state) for two reasons: firstly, it allows an explicit dependence on hydrogel composition as characterized in laboratories; secondly, the characteristic time of diffusion (governing chemical equilibrium) is significantly longer than the one governing mechanical equilibrium (LUCANTONIO ET AL., 2013). Therefore, starting from the as-prepared state, transient mechanisms governing the diffusion of the fluid and the crosslinker agent will occur. For dealing with the resulting variations, both in time and space, a numerical discretization of the chemo-mechanical continuum problem is necessary. The finite element implementation of the proposed model is presented in Chapter 4.

Chapter 4

Numerical treatment

In this chapter, the applied numerical methods for solving the nonlinear differential equations from the continuum mechanics in Chapter 3, and their conversion from the strong form to the weak form will be explained. Furthermore, a summary of the Finite Element Method (FEM) fundamentals will be described. For detailed explanation, reader is referred to ZIENKIEWICZ & TAYLOR (2005), and WRIGGERS (2008). The concepts considered here forms the basis of the implemented numerical model.

4.1 Spatial discretization

For finding the solution of the FEM problems associated with the weak formulations of the non-linear problems described in Eqs. (3.23), and (3.24), the continuous body $\mathcal{B}$ is subdivided into a finite number n_e of compatible, and non-overlapping elements. Thus, the continuous body $\mathcal{B}$ subdivided into n_e elements as

$$\mathcal{B} \approx \mathcal{B}_e = \bigcup_{e=1}^{n_e} \Omega_e. \tag{4.1}$$

Several types of elements can be utilized for the discretization of the continuum domain. For Instance, quadrilateral or triangular elements are used for the two-dimensional cases, and hexahedral or tetrahedral elements are employed for the three-dimensional cases. As an example, Fig. 4.1a illustrates a domain, which is subdivided in quadrilateral elements by representing the continues boundary with the discrete boundary $\partial\mathcal{B}_e$.

4.1.1 Isoparametric mapping

The exact solution of the mathematical model can be approximated utilizing interpolation functions based on the standard Galerkin approach; hence, the estimated primary field variables (i.e., $\mathbf{p} = \{\mathbf{u}, \mu_f, C_c\}$) from Eq. (3.12) within one finite element can be written as,

$$\mathbf{p}(\mathbf{X}) \approx \mathbf{p}_e(\mathbf{X}) = \sum_{i=1}^{m} N_i(\mathbf{X})\, \mathbf{p}_i\,, \tag{4.2}$$

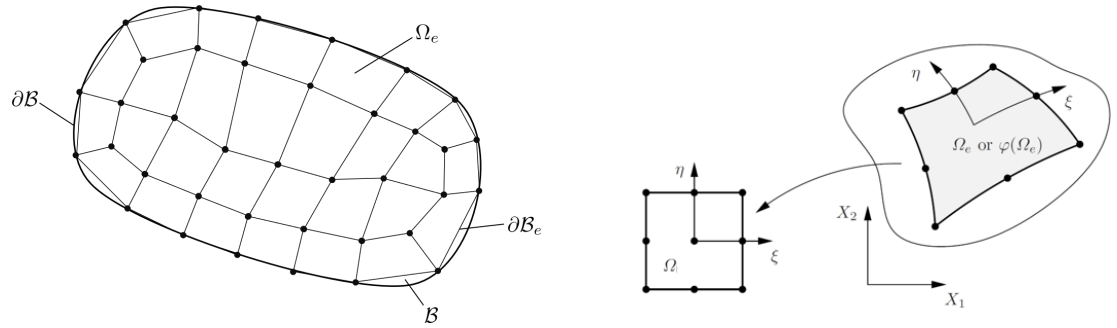

(a) (b)

Figure 4.1: Discretized continuum body $\mathcal{B}$ (a); Isoparametric mapping considering the reference configuration Ω (WRIGGERS, 2008) (b).

in which, $\mathbf{p}_i$ is the unknown field and/or nodal variables, N_i represents shape functions defined in Ω_e, m depicts the number of unknown nodal variables, and $\mathbf{X}$ is the coordinate of a material point in a reference configuration. The reference configuration in FEM is introduced for facilitating the numerical integration, see Fig.4.2. As a matter of fact, the provided partial differential equation's true solution requires to be converged for the approximated primary variables $\mathbf{p}_e$. Several options exist to form the interpolation or ansatz functions for geometry and variables within the finite element method. Because of convergence-related reasons, the interpolation functions have to be fulfilled up to the approximation order (ZIENKIEWICZ ET AL., 2000). The isoparametric concept is mostly utilized as an interpolation strategy for numerous engineering study cases. Based on this concept, geometry and variables are interpolated by the same shape functions. Sufficient accuracy and good mapping of arbitrary geometries are obtained using isoparametric elements into a finite element mesh. Also, the spatial formulation discretization can be easily acquired, considering nonlinear problems by using the isoparametric concept. Regardless of the performance of the isoparametric mapping from the initial or the spatial configuration, it will be mapped into the reference configuration. All kinematical variables as well as the geometry. The shape or ansatz functions are determined locally for the interpolation inside the element. The primary variables and the geometry both in the initial $\mathbf{X}$ or spatial configuration $\mathbf{x}$ are interpolated by the same shape function N_i by the classical isoparametric mapping. Additionally, the geometry of an element with the same ansatz function is described in what follows,

$$\mathbf{X} \approx \mathbf{X}_e = \sum_{i=1}^{m} N_i(\boldsymbol{\xi})\mathbf{X}_i, \tag{4.3a}$$

$$\mathbf{x} \approx \mathbf{x}_e = \sum_{i=1}^{m} N_i(\boldsymbol{\xi})\mathbf{x}_i, . \tag{4.3b}$$

For the ansatz function N_i normally a polynomial function is chosen, which is defined in the reference configuration Ω for characterizing the arbitrary element geometries in the initial or spatial configuration. The shape function that is defined in the initial configuration in Eq. (4.3a) is substituted by $N_i(\boldsymbol{\xi})$ in the reference configuration Ω. Hence, a transformation by Eq. (4.3a) has to be executed for each element in initial configuration Ω_e, which associates

with the coordinate $\mathbf{X}_e = \mathbf{X}_e(\boldsymbol{\xi})$ to the coordinates $\boldsymbol{\xi}$ in the reference configuration Ω (See Fig.4.1b). It is noteworthy to mention that these isoparametric transformation has to preserve the type of element such that a quadrilateral element has to be remained a quadrilateral element in the initial or deformed finite element configurations. The mentioned isoparametric transformation will be employed by considering all coordinate directions in identical behaviour. When an element undergoes a physical deformation, the volume Ω in the reference configuration will not be occupied by the real configuration. Meanwhile, for handling different configuration, reference configuration supplies a simple way that can be utilized for the integration of the element matrices. Particularly, it makes more comprehensible formulations correlated to the current configuration whether the transformation is implemented from the reference element to the current or the initial configuration. The mentioned transformation procedure is shown in Fig. 4.2, in which the mapping of an element from the initial configuration Ω_e to the current configuration $\varphi(\Omega_e)$ is performed by applying the approximate deformation map φ_e. The deformations gradient $\mathbf{F}_e$, which is only associated to the element Ω_e and not to be confused with the elastic one described in Eqs. (3.16), is required for the mapping procedure. The following kinematical relations for a finite element can be simply concluded from Fig. 4.2,

$$\mathbf{F}_e = \mathbf{j}_e \mathbf{J}_e^{-1} \,, \tag{4.4a}$$

$$J_e = \det\mathbf{F}_e = \frac{\det\mathbf{j}_e}{\det\mathbf{J}_e}, \tag{4.4b}$$

where, it depicts the deformation gradient's definition by the isoparametric mapping from reference Ω to the initial configuration Ω_e and to the current configuration $\varphi_e(\Omega_e)$. The gradients $\mathbf{j}_e$ and $\mathbf{J}_e$ in Eq. (4.4) are formulated as,

$$\mathbf{j}_e = \nabla_\xi \mathbf{x}_e = \frac{\partial \mathbf{x}}{\partial \boldsymbol{\xi}} = \sum_{i=1}^{m} N_{i,\xi}(\boldsymbol{\xi}) \mathbf{x}_i \otimes \mathbf{E}_\xi \,, \tag{4.5a}$$

$$\mathbf{J}_e = \nabla_\xi \mathbf{X}_e = \frac{\partial \mathbf{X}}{\partial \boldsymbol{\xi}} = \sum_{i=1}^{m} N_{i,\xi}(\boldsymbol{\xi}) \mathbf{X}_i \otimes \mathbf{E}_\xi \,, \tag{4.5b}$$

in which, the derivatives $N_{i,\xi}$ are described as scalar quantities and can be moved to the basis vectors $\mathbf{E}_\xi$. Thereafter, it gives,

$$\mathbf{j}_e = \sum_{i=1}^{m} \mathbf{x}_i \otimes N_{i,\xi}(\boldsymbol{\xi}) \mathbf{E}_\xi = \sum_{i=1}^{m} \mathbf{x}_i \otimes \nabla_\xi N_{i,\xi}(\boldsymbol{\xi}) \,, \tag{4.6a}$$

$$\mathbf{J}_e = \sum_{i=1}^{m} \mathbf{X}_i \otimes N_{i,\xi}(\boldsymbol{\xi}) \mathbf{E}_\xi = \sum_{i=1}^{m} \mathbf{X}_i \otimes \nabla_\xi N_{i,\xi}(\boldsymbol{\xi}) \,, \tag{4.6b}$$

where, $\nabla_\xi N_i$ represents the gradient of scalar ansatz function N_i with regard to ξ. Hence, considering the mentioned equations, it is relatively simple to build gradients correlated to the initial or current configuration. For instance, the gradients of the primary fields $\mathbf{p}$ in Eq.

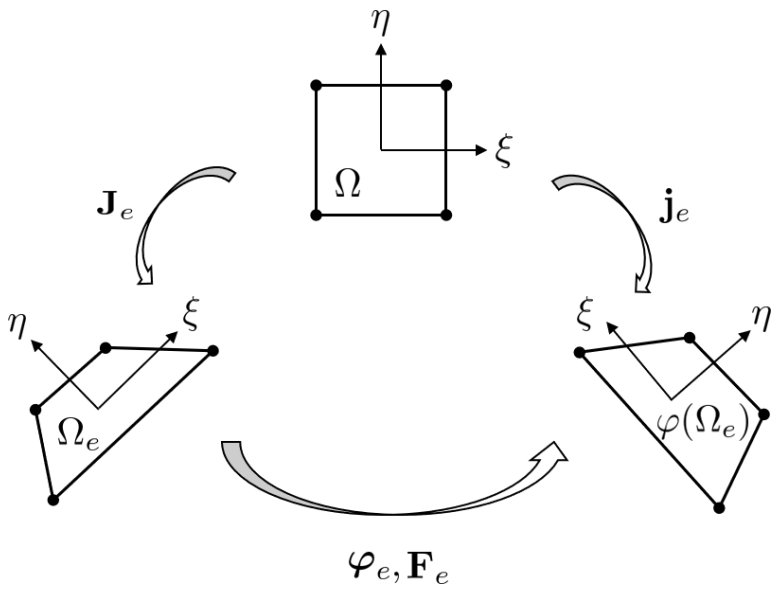

Figure 4.2: Isoparametric mapping for the deformation of an element Ω_e

4.2 can be formulated in an element Ω_e by

$$\nabla_X \mathbf{p}_e = \sum_{i=1}^{n} \mathbf{p}_i \otimes \nabla_X N_i, \tag{4.7a}$$

$$\nabla_x \mathbf{p}_e = \sum_{i=1}^{n} \mathbf{p}_i \otimes \nabla_x N_i. \tag{4.7b}$$

The transformation between the various gradients of different configurations are resulted in,

$$\nabla_\xi N_i = \mathbf{J}_e^T \nabla_X N_i \,, \tag{4.8a}$$

$$\nabla_\xi N_i = \mathbf{j}_e^T \nabla_x N_i \,. \tag{4.8b}$$

Similarly, it holds for the inverse formulation,

$$\nabla_X N_i = \mathbf{J}_e^{-T} \nabla_\xi N_i \,, \tag{4.9a}$$

$$\nabla_x N_i = \mathbf{j}_e^{-T} \nabla_\xi N_i \,. \tag{4.9b}$$

Consequently, the gradient from Eq. (4.7) can be determined in the reference Ω_e and spatial $\varphi(\Omega_e)$ configurations, respectively, as follows,

$$\nabla_X \mathbf{p}_e = \sum_{i=1}^{n} \mathbf{p}_i \otimes \mathbf{J}^{-T} \nabla_\xi N_i, \tag{4.10a}$$

$$\nabla_x \mathbf{p}_e = \sum_{i=1}^{n} \mathbf{p}_i \otimes \mathbf{j}_e^{-T} \nabla_\xi N_i. \tag{4.10b}$$

Regarding the nonlinear finite element methods, the mentioned formulation provides the most flexible approach.

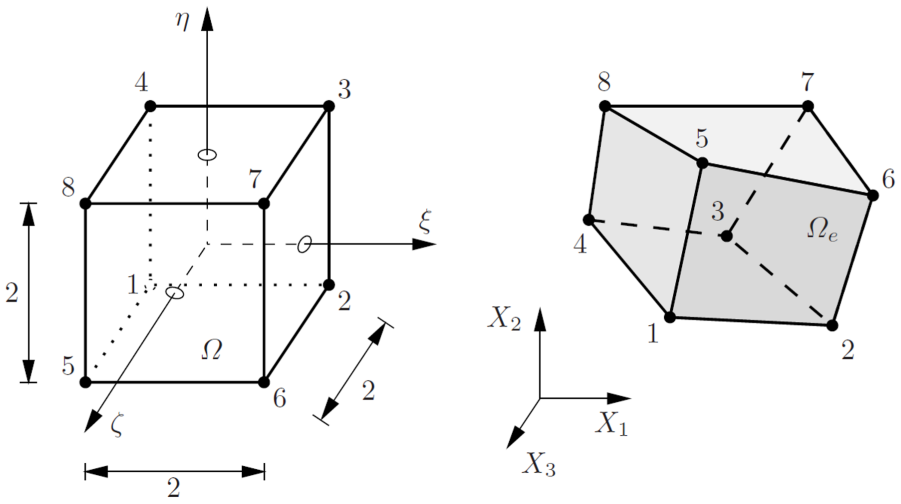

Figure 4.3: Schematic illustration of an isoparametric 8-node hexahedral element (WRIGGERS, 2008).

4.1.2 Three-dimensional shape function

Shape functions which are effective for the isoparametric mapping are provided by the Lagrangian interpolation functions (ZIENKIEWICZ ET AL., 2000). Further, three-dimensional elements utilized in finite element method can have different shapes and patterns. They can have hexahedral or tetrahedral shapes as well as mixtures of both types such as prisms. This section focuses on the formulation of the hexahedral finite elements. It is worthy to mention that the isoparametric mapping is implemented to build the shape funtions for the discretization of three-dimensional geometries. These can be tetrahedral or hexahedral shapes but also mixtures of both types for special geometries like prisms. The 8-noded hexahedral shape function with linear order of interpolation for the three-dimensional element, which is shown in Fig. 4.3, are given by

$$N_i(\boldsymbol{\xi}) = \frac{1}{8}(1+\xi_i\xi)(1+\eta_i\eta)(1+\zeta_i\zeta). \tag{4.11}$$

The nodal coordinates ξ_i, η_i, ζ_i inside the Eq. (4.11) are given in the reference configuration. As shown in Fig. 4.2, the mapping operation from reference configuration Ω into the initial configuration Ω_e and the current configuration $\varphi(\Omega_e)$ is described. As a standard element for this study, a linear hexahedral element (H1) in three-dimensions is used with straight edges, where eight corner nodes describe the shape with eight integration points.

4.2 Temporal discretization

The response of a time-dependent problem in partial differential equations Eq. (3.24) relies on the discretization of the time along with the spatial discretization. Time derivatives are

treated by means of a backward Euler-type finite difference scheme, leading to an implicit formulation. As a notation rule, unknown x at the current time step $t = t_{n+1}$ has no subscript while, at previous time step $t = t_n$, is denoted by x_n. The time step increment is $\Delta t = t_{n+1} - t_n$. All solution algorithms for the transient problems depends on an approximation of the time derivatives which must be selected in a particular time step. Generally, the current residual in Eq. (4.30a), $\mathbf{R} = \mathbf{R}_{n+1} = \mathbf{R}(t_{n+1})$ depend implicitly on all the solution vectors. For instance, the rate of field variables $\mathbf{p}(t)$ can be approximated by a different quotient utilizing the primary variable at different times namely

$$\dot{\mathbf{p}}(t) = \frac{d}{dt}\mathbf{p} \approx \frac{1}{\Delta t}\big[\alpha \mathbf{p}(t_{n-1}) + \beta \mathbf{p}(t_n) + \gamma \mathbf{p}(t_{n+1})\big], \tag{4.12}$$

where, α, β, and γ represent the scalar parameters for the time integration scheme.
The Eq. (4.12) yields to the following system of equations as follows

$$\mathbf{R}(\mathbf{p}, \mathbf{p}_n, \mathbf{p}_{n-1}) = \mathbf{0}, \tag{4.13}$$

with $\mathbf{p} = \mathbf{p}(t)$, $\mathbf{p}_n = \mathbf{p}(t_n)$, and $\mathbf{p}_{n-1} = \mathbf{p}(t_{n-1})$.

4.2.1 First-order finite difference method

By considering the simplest case in Eq. (4.12), in which the time derivatives are estimated by a first-order finite difference scheme (i.e. $\alpha = 0$, $\beta = -1$, and $\gamma = 1$), and applying it to the Eq. (4.12), it gives

$$\dot{\mathbf{p}}(t) \approx \frac{1}{\Delta t}\big[\mathbf{p}(t_{n+1}) - \mathbf{p}(t_n)\big]. \tag{4.14}$$

Hence, by utilizing Eq. (4.14) in the residual vectors of Eq. (4.13), the time-dependent problem can explicitly depend on only two solution vectors as given below

$$\mathbf{R}(\mathbf{p}, \mathbf{p}_n) = \mathbf{0}. \tag{4.15}$$

4.3 Multi-physics computational implementation

The primary variable describing the mechanical deformation is the displacement field $\mathbf{u}$. As regards the chemical description, the fluid chemical potential μ_f is chosen as primary variable for the fluid content, while the molar concentration C_c for calcium content (See Fig. 4.4). This choice is made to ease the imposition of boundary conditions as function of laboratories set-up (see the simulation settings in the simulations and results' Chapter 5). Therefore, denoting by n_{nod} the total number of nodes associated with the finite element spatial discretization, the following set of primary variables $\mathbf{p}$ is introduced:

$$\mathbf{p} = \{\mathbf{u}^i,\, \mu_f^i,\, C_c^i \text{ with } i = 1, \ldots, n_{nod}\}\,, \tag{4.16}$$

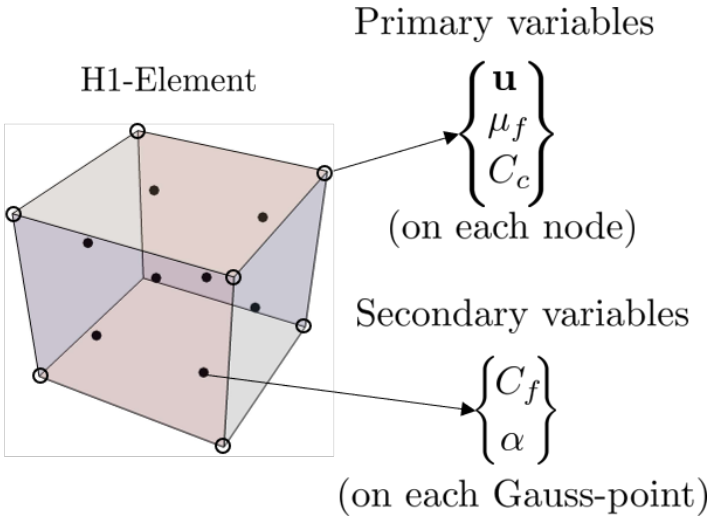

Figure 4.4: Schematic demonstration of the developed H1-Element with primary variables (i.e., $\mathbf{p} = \{\mathbf{u}, \mu_f, C_c\}$) and secondary variables (i.e., $\mathbf{h} = \{C_f, \alpha\}$).

where $\mathbf{u}^i$, μ_f^i and C_c^i are the values at the i-th node. In an element-wise description, the primary variables associated with the e-th element are collected[1] in vector $\mathbf{p}_e$. In addition, denoting by n_{gp} the number of Gauss integration points, the following set of local (internal) variables $\mathbf{h}$ is also introduced:

$$\mathbf{h} = \{\mathbf{h}_g \text{ with } \mathbf{h}_g = \{C_{f,g}, \alpha_g\} \text{ and } g = 1, \dots, n_{gp}\}\,, \tag{4.17}$$

where $C_{f,g}$ and α_g are the values at the g-th Gauss point (See Fig. 4.4). In an element-wise description, local variables associated with the Gauss points belonging to the e-th element are denoted as $\mathbf{h}_g^e$.

4.3.1 Backward Euler scheme

Local variables $\mathbf{h}$ are determined by solving the following system of nonlinear equations in each Gauss point $g = 1, \dots, n_{gp}$:

$$\text{given } \mathbf{p} \text{ find } \mathbf{h}_g \text{ s.t. } \mathbf{Q}_g(\mathbf{p}, \mathbf{h}_g) = \begin{pmatrix} Q_f(\mathbf{p}, \mathbf{h}_g) \\ Q_\alpha(\mathbf{p}, \mathbf{h}_g) \end{pmatrix} = \mathbf{0}\,, \tag{4.18}$$

where Q_f and Q_α are derived respectively from Eqs. (3.51a) and (3.59):

$$Q_f = \mu_f - \bar{\mu}_f - RT\left[\ln\left(m_f(C_f, C_c)\right) - \chi\left(\frac{v_p}{v_p + v_f(C_f)}\right)^2\right] - \mu_f^\sigma(\mathbf{C}_e, \alpha)\,, \tag{4.19a}$$

$$Q_\alpha = \alpha - \alpha_n - \Delta t\left[\frac{KC_c}{J^2 C_A}\left(1 - \alpha + \frac{\hat{p}}{\kappa_\alpha}\right)\right]. \tag{4.19b}$$

[1]Element-wise quantities will be denoted by subscript e, to be not confused with quantities associated with the elastic part of the deformation introduced in Section 3.2.

The local system of equations (4.18) is solved by means of the Netwon-Raphson method. For a given value of the primary variables $\mathbf{p}$, value $\mathbf{h}_g$ is found iteratively as:

$$\mathbf{h}_g \rightarrow \mathbf{h}_g + \Delta\mathbf{h}_g \;\text{ until }\; \|\Delta\mathbf{h}_g\| < tol_{loc}\,, \tag{4.20}$$

where tol_{loc} is the tolerance of the local problem (with $tol_{loc} = 10^{-8}$ in all numerical simulations) and increment $\Delta\mathbf{h}_g$ at each iteration is the solution of:

$$\mathbf{A}_g\Delta\mathbf{h}_g + \mathbf{Q}_g = \mathbf{0} \;\text{ with }\; \mathbf{A}_g = \frac{\partial\mathbf{Q}_g}{\partial\mathbf{h}_g} \tag{4.21}$$

with $\mathbf{A}_g$ being the tangent matrix of the local (Gauss point level) problem.
Primary variables $\mathbf{p}$ are found from the weak form of Eqs. (3.23) and (3.24) together with a standard Galerkin spatial discretization based on Lagrangian shape functions with the same interpolation order for all fields, i.e.

$$\begin{pmatrix}\mathbf{u}(\mathbf{X})\\ \mu_f(\mathbf{X})\\ C_c(\mathbf{X})\end{pmatrix} = \sum_{i=1}^{n_{nod}} N_i(\mathbf{X}) \begin{pmatrix}\mathbf{u}^i\\ \mu_f^i\\ C_c^i\end{pmatrix}\,. \tag{4.22}$$

4.3.2 Local residual

The resulting residual non-linear algebraic set of equations reads:

$$\text{given }\; \mathbf{h} \;\text{ find }\; \mathbf{p} \;\text{ s.t. }\; \mathbf{R}(\mathbf{p},\mathbf{h}) = \mathbf{0} \tag{4.23}$$

Residuum $\mathbf{R}$ is obtained from a variational formulation based on the definition of a pseudo-energy potential, which in an element-wise description reads:

$$\Pi_e(\mathbf{p}_e,\mathbf{h}_g^e) = \int_{\Omega_e} (\Psi_{mech} + \mu_f b_f + \nabla_{\mathbf{X}}\mu_f\cdot\mathbf{b}_f + C_c b_c + \nabla_{\mathbf{X}}C_c\cdot\mathbf{b}_c)\,d\Omega \tag{4.24}$$

where Ω_e is element domain in the reference configuration, the mechanical part of the free-energy Ψ_{mech} is given in Section 3.7, and the chemical pseudo-energy terms b_f, $\mathbf{b}_f$, b_c and $\mathbf{b}_c$ are defined as:

$$b_f = \frac{C_f - C_{f,n}}{\Delta t}\,, \qquad \mathbf{b}_f = C_f\mathbf{D}_f\nabla_{\mathbf{X}}\mu_f\,, \tag{4.25a}$$

$$b_c = \frac{C_c - C_{c,n}}{\Delta t} + N_c C_c\frac{\alpha-\alpha_n}{\Delta t}\,, \qquad \mathbf{b}_c = C_c\mathbf{D}_c\nabla_{\mathbf{X}}C_c\,. \tag{4.25b}$$

Accordingly, the element-wise residuum reads:

$$\mathbf{R}_e(\mathbf{p}_e,\mathbf{h}_g^e) = \left.\frac{\partial\Pi_e}{\partial\mathbf{p}_e}\right|_{\mathbf{h}_g,b_f,\mathbf{b}_f,b_c,\mathbf{b}_c=const}\,, \tag{4.26}$$

furthermore, the total residuum $\mathbf{R}$ is obtained from a standard assembly procedure. It is immediate to verify that stationary conditions of Eq. (4.24) concerning the displacement

field $\mathbf{u}$ lead to the weak form of the balance of linear momentum [2] in Eq. (3.23), while with respect to potential μ_f and concentration C_c lead to the weak form of fluid [3] and calcium [4] in Eqs. (3.24). This is true only under the differentiation rules specified in Eq. (4.26) and since Ψ_{mech} is not an explicit function of μ_f and C_c (see Eq. (3.40)).

4.3.3 Global residual and tangent matrix

The resulting nonlinear system of algebraic equations (4.23) for the determination of the primary variables are solved by means of a Newton-Raphson procedure which reads:

$$\mathbf{p} \rightarrow \mathbf{p} + \Delta\mathbf{p} \;\; \text{until} \;\; \|\Delta\mathbf{p}\| < tol_{glo}\,, \tag{4.27}$$

where tol_{glo} is the tolerance of the global problem (with $tol_{glo} = 10^{-8}$ in all numerical simulations) and increment $\Delta\mathbf{p}$ at each iteration is the solution of:

$$\mathbf{K}\Delta\mathbf{p} + \mathbf{R} = \mathbf{0}\,, \tag{4.28}$$

with $\mathbf{K}$ being the tangent matrix of the global (equilibrium) problem. Tangent $\mathbf{K}$ is obtained from the assembly of the element-wise counterparts $\mathbf{K}_e$:

$$\mathbf{K}_e = \left.\frac{D\mathbf{R}_e}{D\mathbf{p}_e}\right|_{\frac{D\mathbf{h}_g^e}{D\mathbf{p}_e} = -\mathbf{A}_g^{-1}\frac{\partial \mathbf{Q}_g}{\partial \mathbf{p}_e}}\,. \tag{4.29}$$

which accounts for the implicit dependency of local variables $\mathbf{h}_g^e$ on global ones $\mathbf{p}_e$, thus leading to a consistent linearization of the solving system and ensuring quadratic convergence. The global residual vector $\mathbf{R}$ and the global tangent stiffness matrix $\mathbf{K}$, are formed, respectively, in FEM by the standard assembly procedure by

$$\mathbf{R} = \mathop{\mathbin{\mathop{\mathrm{A}}}}_{e=1}^{\mathrm{n_e}} \mathbf{R}_e\,, \tag{4.30a}$$

$$\mathbf{K} = \mathop{\mathbin{\mathop{\mathrm{A}}}}_{e=1}^{\mathrm{n_e}} \mathbf{K}_e\,, \tag{4.30b}$$

which is required for the Newton-Raphson iterative solver.

[2] With null body loads ($\mathbf{b} = \mathbf{0}$) and apart from boundary terms, the weak form of the balance of linear momentum reads: $\int_\Omega (\mathbf{P}_e \cdot \delta\mathbf{F}_e)\, d\Omega = 0$, for any admissible variation $\delta\mathbf{F}$. It is noteworthy that, under the differentiation rules in Eq. (4.26)(and in particular $\mathbf{h}$= constant), it results (see Eq. (3.26) with $\dot{J}_{fc} = 0$ and Eq. (3.36a)):

$$\mathbf{P}_e \cdot \delta\mathbf{F}_e = \mathbf{P}_e \cdot \frac{\partial \mathbf{F}_e}{\partial \mathbf{u}}\delta\mathbf{u} = \frac{1}{2} J_{fc}\mathbf{S}_e \cdot \frac{\partial \mathbf{C}_e}{\partial \mathbf{u}}\delta\mathbf{u} = \frac{\partial \Psi_{mech}}{\partial \mathbf{C}_e} \cdot \frac{\partial \mathbf{C}_e}{\partial \mathbf{u}}\delta\mathbf{u},$$

proving that stationary conditions in Eq. (4.26) lead to the weak form of the linear momentum balance.

[3] Apart from boundary terms, the weak form of fluid mass balance reads: $\int_\Omega (\delta\mu_f b_f + \nabla_{\mathbf{X}}\delta\mu_f \cdot \mathbf{b}_f)\, d\Omega = 0$, for any admissible variation $\delta\mu_f$, it is immediate to prove that this is obtained from Eq. (4.26).

[4] Apart from boundary terms, the weak form of calcium mass balance reads: $\int_\Omega (\delta C_c b_c + \nabla_{\mathbf{X}}\delta C_c \cdot \mathbf{b}_c)\, d\Omega = 0$, for any admissible variation δC_c, it is immediate to prove that this is obtained from Eq. (4.26).

The local and global Newton-Raphson procedures in Eqs. (4.18) and (4.23) are solved in a nested scheme as for standard locally-coupled Gauss point problems with adaptive time stepping (KORELC & WRIGGERS, 2016). A schematic description of the associated algorithm can be seen in Algorithm 1. Codes are developed through the Wolfram Mathematica package AceGen, a tool that allows for automated computational modeling (e.g., automatic differentiation) through a combined numeric-symbolic strategy (KORELC & WRIGGERS, 2016; HUDOBIVNIK, 2016). In particular, a three-dimensional hexahedral element with trilinear Lagrangian shape functions (H1), characterized by 8 nodes and $2 \times 2 \times 2$ Gauss integration points, has been implemented in this study [5].

[5] For a detailed description on the element technology, see KORELC & WRIGGERS (2016).

Algorithm 1 Pseudocode of the coupled iterative algorithm with adaptive time stepping

procedure GLOBAL NEWTON-RAPHSON ITERATIVE SCHEME
  Given: $\{\boldsymbol{p}_n,\ \boldsymbol{h}_n,\ \mathbf{F}_n,\ \mathbf{F}_{en},\ \mathbf{F}_{fcn},\ \Psi_n\}$
  Find: $\{\boldsymbol{p} = \{\mathbf{u}, \mu_f, C_c\},\ \boldsymbol{h} = \{C_f, \alpha\},\ \mathbf{F},\ \mathbf{F}_e,\ \mathbf{F}_{fc},\ \Psi\}$
  Input: $\boldsymbol{p}_0$, $\boldsymbol{h}_0$, t_0, Δt_0 // starting values for $\{\boldsymbol{p}_n,\ \boldsymbol{h}_n,\ t_n,\ \Delta t\}$
  $\boldsymbol{p}_n \leftarrow \boldsymbol{p}_0$; $\boldsymbol{h}_n \leftarrow \boldsymbol{h}_0$; $t_n \leftarrow 0$; $\Delta t \leftarrow \Delta t_0$
  repeat
    $t \leftarrow t_n + \Delta t$
    begin solution of one step
      $\boldsymbol{p} \leftarrow \boldsymbol{p}_n$ // last converged solution for the current step
      repeat
        for each element **do**
          procedure LOCAL NEWTON-RAPHSON($\boldsymbol{h}_g$)
            begin sub iterative loop
              $\boldsymbol{h}_g \leftarrow \boldsymbol{h}_{gn}$
              repeat
                $\mathbf{Q}_g \leftarrow \mathbf{Q}_g(\boldsymbol{p}, \boldsymbol{h}_g)$ from Eq. (4.19)
                $\mathbf{A}_g \leftarrow \frac{\partial \mathbf{Q}_g}{\partial \boldsymbol{h}_g}$
                solve $\mathbf{A}_g \Delta \boldsymbol{h}_g + \mathbf{Q}_g = 0$ for unknown $\Delta \boldsymbol{h}_g$
                $\boldsymbol{h}_g \leftarrow \boldsymbol{h}_g + \Delta \boldsymbol{h}_g$
              until error criterion for $||\Delta \mathbf{h}_g||$ is fulfilled
            end
          end procedure
          $\mathbf{R}_e \leftarrow \mathbf{R}_e(\boldsymbol{p}_e, \boldsymbol{h}_g^e(\boldsymbol{p}_e))$
          $\mathbf{K}_e \leftarrow \frac{\partial \mathbf{R}_e}{\partial \boldsymbol{p}_e}\Big|_{\frac{D\boldsymbol{h}_g^e}{D\boldsymbol{p}_e} = -\boldsymbol{A}_g^{-1}\frac{\partial \mathbf{Q}_g}{\partial \boldsymbol{p}_e}}$
          assemble $\mathbf{R}_e$ to $\mathbf{R}$ and $\mathbf{K}_e$ to $\mathbf{K}$
        end for
        solve $\mathbf{K}\Delta \boldsymbol{p} + \mathbf{R} = 0$ for unknown $\Delta \boldsymbol{p}$
        $\boldsymbol{p} \leftarrow \boldsymbol{p} + \Delta \boldsymbol{p}$
      until error criterion for $\|\Delta \mathbf{p}\|$ is fulfilled
    end
    if error criterion is fulfilled **then**
      $\boldsymbol{p}_n \leftarrow \boldsymbol{p}$; $\boldsymbol{h}_n \leftarrow \boldsymbol{h}$; $t_n \leftarrow t$ // update solution for next time step
      adjust time step Δt
    else
      reduce time step Δt
    end if
  until total time is reached
  Results: $\{\boldsymbol{p},\ \boldsymbol{h},\ \mathbf{F},\ \mathbf{F}_e,\ \mathbf{F}_{fc},\ \mathbf{Q},\ \Psi\}$// converged solution in last step
end procedure

Chapter 5

Simulations and results

Dynamics of swelling and deswelling (i.e., absorption-desorption) in the context of hydrogels have attracted great interest recently TANAKA ET AL. (1987); HONG ET AL. (2008); DOI (2009). A vast understanding of the dynamics of swelling and deswelling is crucial for engineering and designing an optimal gel shape and refining the rate of drug release, avoiding crack propagation in reusable sensors or actuators, or optimizing tissue engineering scaffolds.

In this Chapter, few illustrative numerical simulations are shown on the chemo-mechanical response of different test cases, such as a cubic hydrogel under free-swelling, buckling of hydrogel tubes, wrinkling of cuboid gels, bending of a polymeric bilayer bar, and spherical hydrogel confined swelling. The proposed analysis aims to demonstrate the model's capability to elucidate complex coupled mechanisms and the developed numerical implementation's effectiveness.

An alginate hydrogel with 8 % (w/v) sodium alginate in 2 ml of water is addressed. Values of model parameters are reported in Table 5.1 and are mainly chosen on the basis of well-established literature evidence (such as for the elasticity constants and the diffusivity-related parameters). Swelling- and shrinking-related parameters are identified from the following considerations: *i)* the fluid molar volume Λ_1 at $\alpha = 1$ is defined as 10% of the reference fluid molar volume Λ_0 at $\alpha = 0$; *ii)* the shrinking parameter Γ is chosen as 10% of a reference value $\bar{\Gamma} = \Lambda_1 \bar{C}_{fo}^{ap}$ which would correspond to null swelling for $\alpha_o = 1$ in the as-prepared state (i.e., $J_{so}^{ap} = 1$). Furthermore, few evidence are available on the value of the reaction rate K and no data could be found on the chemo-mechanical coupling modulus κ_α. Accordingly, ratio $r_\Lambda = \Lambda_1/\Lambda_o$, and parameters Γ, K and κ_α will be object of a parametric study in Section 5.2.4.

5.1 Initialization and boundary conditions

Simulations are initialized from the as-prepared state (see Section 3.9) with the utilized total volume of $V_o = J_o \bar{V}_p$ which is consistently applied for every test case. The as-prepared fluid chemical potential inside the hydrogel can be computed from Eq. (3.64), resulting in $\mu_{fo}^{ap} = -834$ J/mol. The computation of J_{eo}^{ap} allows defining the reference dimensions of the specimen, corresponding to the computational domain of the finite element model discretized

by a three-dimensional hexahedral element with trilinear Lagrangian shape functions (H1), characterized by 8 nodes and $2 \times 2 \times 2$ Gauss integration points (See Chapter 4).
In terms of boundary condition, the as-prepared gel is firstly considered to be immersed in a bath of calcium chloride solution (resulting in absorption of water and calcium) and then removed from the bath (determining water desorption). This process is repeated for different number of cycles (i.e. depending on the test case) in order to investigate how absorption and desorption mechanisms are altered by the calcium-related crosslinking kinetics. The duration of each cycle is denoted as τ_d and chosen in agreement with the characteristic time scale of fluid diffusion in the hydrogel. In each cycle $n_c = 1, \dots, 4$, the following time-varying boundary conditions are applied for the chemical problem on the entire external surface $\partial\mathcal{B}_o$ of the hydrogel:

$$\begin{aligned} t \in [(n_c-1)\tau_d, (n_c-1)\tau_d + t_{ab}] \quad &\Rightarrow \quad \begin{cases} \mu_f|_{\partial\mathcal{B}_o} = \mu_f^{bath} \\ C_c|_{\partial\mathcal{B}_o} = \bar{C}_c \end{cases} , \\ t \in ((n_c-1)\tau_d + t_{ab}, (n_c-1)\tau_d + t_{de}] \quad &\Rightarrow \quad \begin{cases} \mu_f|_{\partial\mathcal{B}_o} = \mu_f^{air} \\ \nabla C_c \cdot \mathbf{n}|_{\partial\mathcal{B}_o} = 0 \end{cases} , \end{aligned} \tag{5.1}$$

where $t_{ab} = (n_c-1)\tau_d + \tau_d/2$ is the end of the absorption phase and $t_{de} = (n_c-1)\tau_d + \tau_d = n_c\tau_d$ of the desorption phase. For each cycle, two additional relevant time-points $t_{ab}^{1/2} = (n_c-1)\tau_d + \tau_d/4$ and $t_{de}^{1/2} = (n_c-1)\tau_d + 3\tau_d/4$ are introduced at the middle of the absorption and of the desorption phases, respectively. Moreover, a normalized variable $\tau = t/\tau_d \in [0, 4]$ for the entire time range of the simulations is also introduced.
In Eq. (5.1), the fluid chemical potential is assigned equal to the one in the bath μ_f^{bath} during absorption and equal to the one in air μ_f^{air} during desorption. In particular, μ_f^{air} is chosen to be in equilibrium with the as-prepared one (i.e., $\mu_f^{air} = \mu_{fo}^{ap}$), while the one in the bath μ_f^{bath} can vary case-by-case. During the absorption phase, calcium concentration at the boundary is fixed to the one in the bath, while during desorption a null flux condition is considered. Different values for the bath calcium concentration $\bar{C}_c$ are employed and specified case-by-case. To be consistent with laboratories specifications, $\bar{C}_c$ is expressed in terms of the corresponding weight/volume percentage concentration $\tilde{C}_c$ of the calcium chloride solution in the bath[1], which is generally assigned during experiments. For numerical reasons, the step-wise change of boundary conditions values in Eq. (5.1) are regularized by means of a steep linear function (going from the initial to the final value in a time range lower than $0.01\tau_d$. The adaptive time discretization scheme employs a time step in the interval $10^{-6}\tau_d \leq \Delta t \leq 10^{-2}\tau_d$).

[1]The molar concentration of calcium ions can be read from the weight/volume (w/v) concentration of the calcium chloride solution as $\bar{C}_c = w_{CaCl_2}\tilde{C}_c$ where $w_{CaCl_2} = 110.98$ g/mol is calcium chloride molar mass. For instance, a solution of $\tilde{C}_c = 1\%$ (w/v) = 0.01 mg/μl corresponds to $\bar{C}_c = 90$ mM.

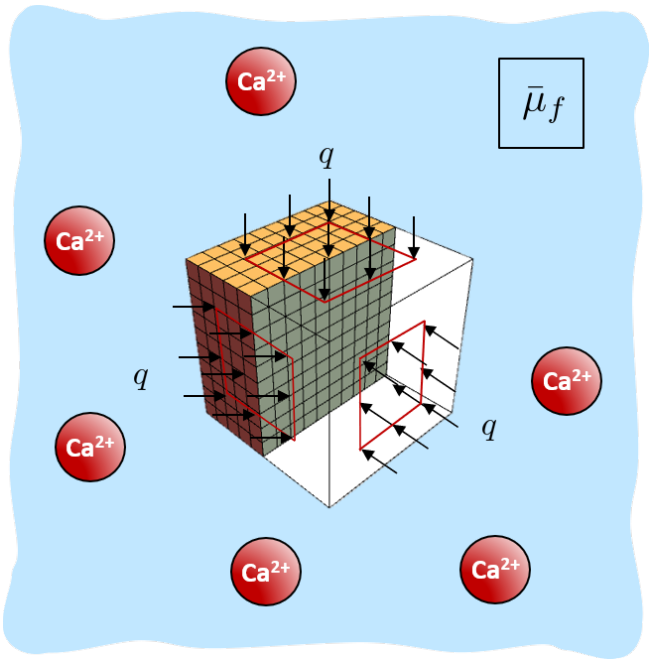

Figure 5.1: Numerical simulations set-up: cross-sectional view of the cubic specimen, mesh details, boundary conditions schematic. Four absorption-desorption cycles are considered: the hydrogel is immersed in a bath of calcium chloride $CaCl_2$ solution during the absorption phase undergoing swelling-crosslinking mechanisms, and removed from the bath during the desorption phase. *As-prepared* initial conditions, as detailed in Table 5.1, are considered.

5.2 Free-swelling of cubic hydrogel

The first benchmark test is a cube with the length of $L_o = V_o^{1/3}$, here resulting $L_o \approx 2.14$ mm, aligned with the coordinate axes $(\mathbf{i}, \mathbf{j}, \mathbf{k})$ parametrized in (X, Y, Z) in the reference configuration.

Considering the mentioned time scale τ_d, the duration of each cycle for the cubic hydrogel is denoted as $\tau_d = L_o^2/\bar{D}_f$ which results in ca. $\tau_d = 2.5$ hours. From the mechanical viewpoint, rigid body motions are prevented by applying a minimal set of boundary conditions. Among these, it is highlighted that the bottom surface at $Z = 0$ is constrained in the direction identified by $\mathbf{k}$. In Section 5.2.7, chemo-mechanical coupling effects are investigated by considering a distributed load of magnitude q applied in the normal inward direction on all surfaces, like a constrained swelling experiment.

The computational domain is discretized with a structured mesh of H1 elements with a total number of degrees of freedom equal to 10985. A schematic representation of the numerical case study is shown in Fig. 5.1. If not differently specified, the reference simulation settings are chosen as: $\mu_f^{bath} = \bar{\mu}_f$, that is the bath fluid chemical potential equal to the reference fluid one; a concentration $\tilde{C}_c = 1\%$ (w/v) of calcium chloride in the solution; a null external load $q = 0$. The only-fluid case is identical to the reference settings but with $\tilde{C}_c = 0$.

Table 5.1: Values of parameters employed in numerical simulations with relevant references (when missing, see the explanation provided at the beginning of Chapter 5). Biophysical properties of alginate for the definition of the as-prepared state are given in Table 3.1.

Parameter	**Value**	**Source**
$\bar{C}_p$	0.08 mg/μL	as-prepared state
$\bar{V}_{fo}$	2 ml	as-prepared state
α_o	0.01	as-prepared state
G_p^0	10 kPa	DRURY ET AL. (2004)
G_p^1	10 G_p^0	DRURY ET AL. (2004)
ν_p	0.499	BOUKLAS & HUANG (2012)
$\bar{\mu}_f$	0.0 J/mol	BOUKLAS & HUANG (2012)
D_f^0	0.5 $\times$ 10^{-9} m^2/s	SALAHSHOOR & RAHBAR (2014)
D_f^1	0.5D_f^0	SALAHSHOOR & RAHBAR (2014)
Λ_0	10^{-4} m^3/mol	CHESTER & ANAND (2011)
Λ_1	$r_\Lambda \Lambda_0$ with $r_\Lambda = 0.1$	–
χ	0.2	CHESTER ET AL. (2015)
D_c^0	0.83 $\times$ 10^{-9} m^2/s	BRASCHLER ET AL. (2011)
D_c^1	0.5 D_c^0	HAJIKHANI ET AL. (2019)
α_{gel}	0.2	HAJIKHANI ET AL. (2019)
n	5	HAJIKHANI ET AL. (2019)
K	1 s^{-1}	THU ET AL. (2000)
N_c	0.1	THU ET AL. (2000)
Γ	0.1 $\bar{\Gamma}$ *	–
κ_α	1 MPa	–

$*$ The reference value $\bar{\Gamma}$ is chosen as the one which would correspond to null swelling for $\alpha_o = 1$ in the as-prepared state, that is $\bar{\Gamma} = \Lambda_1 \bar{C}_{fo}^{ap}$.

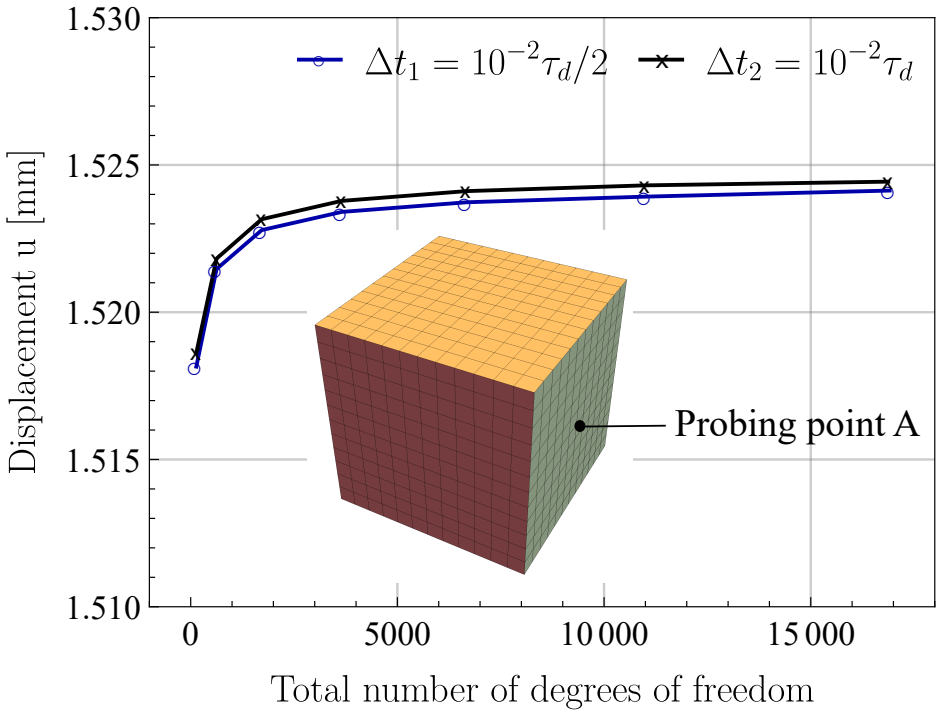

Figure 5.2: Displacement u located at the probing point A versus the total number of degrees of freedom, results are presented for two different maximum time step intervals (i.e., Δt_1 , Δt_2).

5.2.1 Convergence study

This section reports a convergence analysis investigating the independency of numerical results on the introduced discretization. In particular, Fig. 5.2 depicts the convergence study for the displacement u at the end of the absorption period t_{ab} at probing point A, which is in the center of the outer surface versus the total number of degrees of freedom for the hydrogel cube. Moreover, Fig.5.3 presents the convergence analysis for the calcium concentration C_c at the probing point B, located in the center of the hydrogel cube. Considering the time step independence of the numerical simulations, the mentioned convergence studies are applied for two different maximum time step intervals, that is $\Delta t_1 = 10^{-2}\tau_d/2$ and $\Delta t_2 = 10^{-2}\tau_d$. Results show a promising convergence for the number of degrees of freedom, approximately more than 5000, justifying the adopted number of degrees of freedom (>10000) in all numerical simulations. Similarly, dependency on the time step size results is not significant, which justifies the choice of Δt_2 in all numerical simulations.

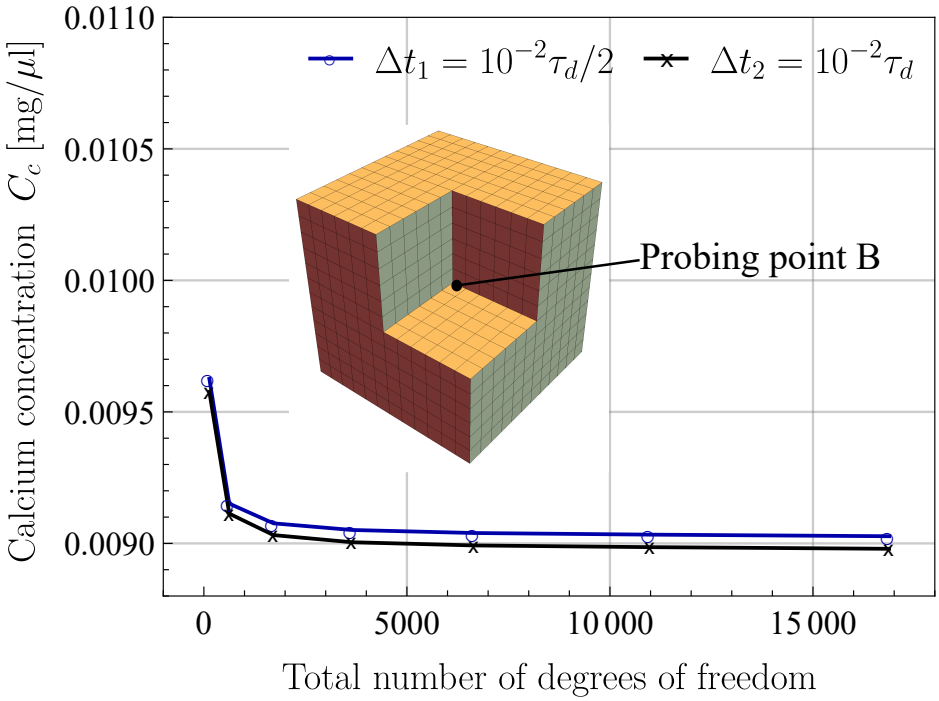

Figure 5.3: Calcium chloride C_c situated at the probing point B for two different maximum time step intervals (i.e., Δt_1 , Δt_2) with respect to the total number of degrees of freedom.

5.2.2 Chemo-mechanical hydrogel behaviour

The distribution of chemo-mechanical variables within the hydrogel as obtained from numerical simulations is shown in Figs. 5.4 which represent a snapshot at the end of the first absorption phase ($t = t_{ab}$ at $n_c = 1$). In particular, it clearly results from Figs. 5.4(a,b) that fluid and crosslinker contents are not uniform within the specimen, inducing in turn a non-uniform crosslinking degree α in Fig. 5.4c. In addition, the evolution of the crosslinking degree alters mechanical and diffusivity properties in the hydrogel, as shown by the distribution of fluid diffusivity D_f, calcium diffusivity D_c in Fig. 5.4(d,e) and polymer shear modulus G_p in Fig. 5.4f. A higher crosslinking degree corresponds to a reduced diffusivity (due to obstruction effects) and increased stiffness (due to an increase of molecular bonds). In turn, these alterations affect the solution of the chemo-mechanical balance equations leading to a fully coupled system.

The evolution of this coupled system changes during the time in the considered absorption-desorption cycles. The deformed configurations along the time path are shown in Fig. 5.5, where the local volume change $J = \det\mathbf{F}$ is shown at different times. The numerical model's capability of capturing extremely large deformations, up to $J > 10$, is highlighted. Moreover, it can be noticed that the corners of the hydrogel cube are swelling promptly. It is due to the largest contact surface with the solvent, and hence to the highest amount of fluid entering the hydrogel. The growth will be followed by cube edges and then surfaces. This phenomenon has been experimentally observed by ZHANG ET AL. (2009). The hydrogel response changes during time in the considered absorption-desorption cycles. Hydrogel

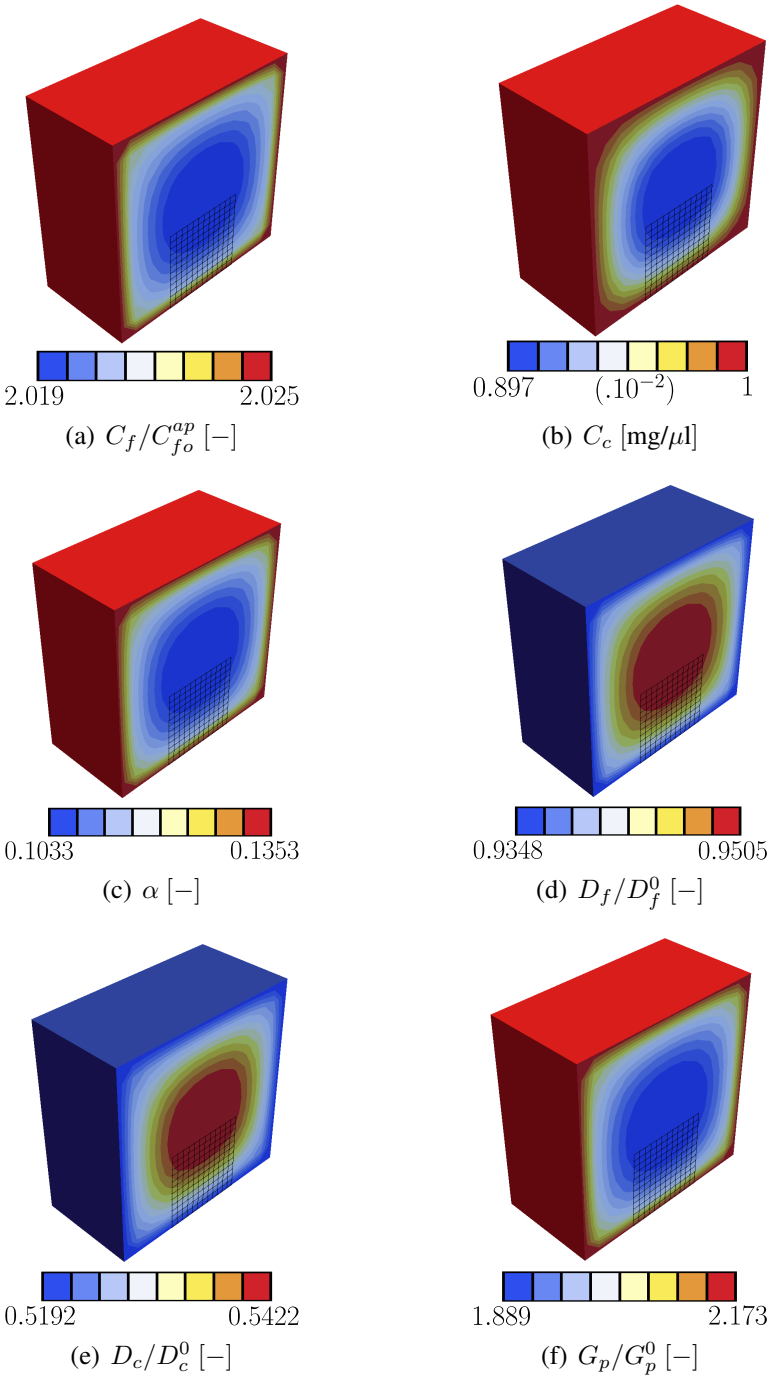

(a) C_f/C_{fo}^{ap} [−] (b) C_c [mg/μl]

(c) α [−] (d) D_f/D_f^0 [−]

(e) D_c/D_c^0 [−] (f) G_p/G_p^0 [−]

Figure 5.4: Chemo-mechanical in the hydrogel at the end of the first absorption phase ($t = t_{ab}$ at $n_c = 1$): fluid content C_f normalized with respect to the as-prepared concentration C_{fo}^{ap} (a), crosslinker content C_c (b), gelation degree α (c), fluid diffusivity D_f normalized with respect to the reference value D_f^0 (d), calcium diffusivity D_c normalized with respect to the reference value D_c^0 (e), polymer shear modulus G_p normalized with respect to the reference value G_p^0 (f). Simulation settings correspond to the reference case study: $\mu_f^{bath} = \bar{\mu}_f$, $\tilde{C}_c = 1\%$ (w/v) and $q = 0$. The undeformed mesh (in the reference configuration) is reported in each image.

swelling decreases from the first to the second cycle, with the maximum value of volume change at $t = t_1$ equal to $J = 14.5$ and at $t = t_1$ equal to $J = 12.7$, with a reduction higher than 10%. This shrinking phenomenon is reiterated through the cycles, and it is due to the effect of crosslinking. The following sections present a quantitative assessment of this mechanism.

5.2.3 Effect of external bath composition

In a first analysis, the alteration of the absorption-desorption behavior due to crosslinking kinetics is analyzed for different external calcium concentrations $\tilde{C}_c$ in the bath. Volume change at time t is computed in terms of the volumetric free-swelling capacity $FSC(t)$, defined as:

$$FSC(t) = \frac{1}{V_o}\left(\int_{\mathcal{B}_o} J(\mathbf{X}, t)dV - V_o\right) . \tag{5.2}$$

The free-swelling capacity is normalized with respect to a reference value FSC_r, which is defined as the maximum overall cycles obtained in the only-fluid case, yielding to $nFSC(t) = FSC(t)/FSC_r$.
Results in Fig. 5.6 show that $nFSC(t)$ repeats identically between the different cycles in the only-fluid case because, at each cycle, the hydrogel absorbs and desorbs the same amount of fluid. On the other hand, when calcium is present, $nFSC(t)$ significantly decreases at each cycle, revealing a lower fluid absorption capacity (i.e., swelling). Moreover, $nFSC(t)$ decreases proportionally to the increase of calcium concentration in the bath. The model is thus able to capture the impact of crosslinking extent on the swelling capacity of hydrogels, in agreement with well-established experimental evidence (e.g., MARTINSEN ET AL., 1989; DRAGET ET AL., 2001; DAVIDOVICH-PINHAS & BIANCO-PELED, 2010; GÓMEZ, 2015; RAMDHAN ET AL., 2019).
Further, the influence of the external fluid chemical potential μ_f^{bath} on the swelling behaviour is analysed. In detail, the maximum value $nFSC_{max}$ of $nFSC(t)$ over each cycle (i.e., over $t \in [(n_c - 1)\tau_d, n_c\tau_d]$) is represented in Fig. 5.7. These results show the high non-linear dependency of hydrogel swelling as a function of external conditions. The shrinking phenomenon due to the crosslinking agent's action occurs in all cases but is more or less pronounced depending on the external fluid chemical potential.

5.2.4 Parametric analysis

This section presents a parametric analysis on the parameters governing the main novel contributions of the present formulation, that is, the crosslinking reaction kinetics (Section 5.2.5) and the inelastic rearrangement of crosslinked polymer networks (Section 5.2.6).
The parametric study analyzes $\Delta FSC(t)$, that is the total variation of the free-swelling capacity. In detail, $\Delta FSC(t)$ compares the change of volume of an hydrogel immersed in a bath of calcium chloride solution with respect to the one where the hydrogel is immersed in a bath of pure fluid, that is:

$$\Delta FSC(t) = \frac{1}{FSC_r}\int_{\mathcal{B}_o} \left(J(\mathbf{X}, s) - J_{fluid}(\mathbf{X}, s)\right) dV . \tag{5.3}$$

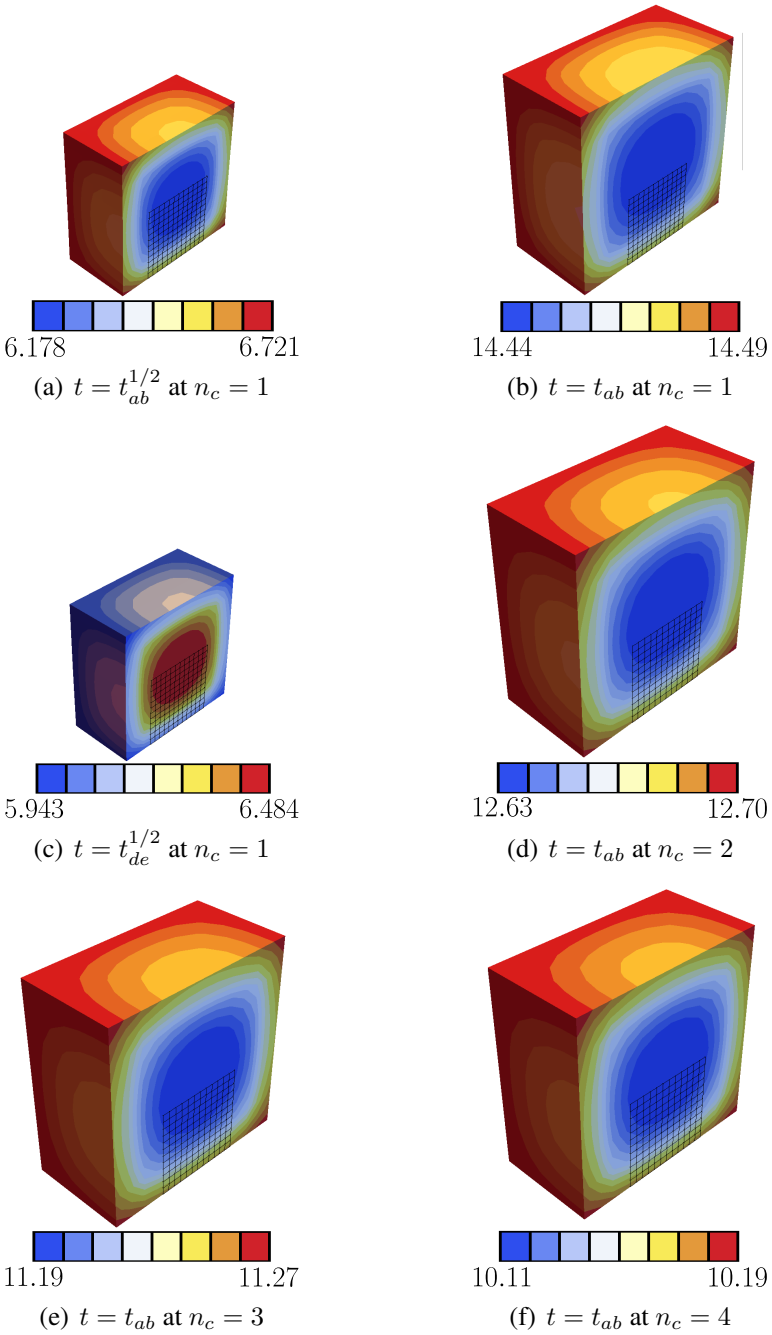

(a) $t = t_{ab}^{1/2}$ at $n_c = 1$ (b) $t = t_{ab}$ at $n_c = 1$

(c) $t = t_{de}^{1/2}$ at $n_c = 1$ (d) $t = t_{ab}$ at $n_c = 2$

(e) $t = t_{ab}$ at $n_c = 3$ (f) $t = t_{ab}$ at $n_c = 4$

Figure 5.5: Local volume change, i.e. $J = \det\mathbf{F}$, at the middle of the first absorption phase (a), at the end of the first absorption cycle (b), at the middle of the first desorption phase (c), and at the end of the second (d), third (e) and fourth (f) absorption phases. Simulation settings correspond to the reference case study: $\mu_f^{bath} = \bar{\mu}_f$, $\tilde{C}_c = 1\%$ (w/v) and $q = 0$. The undeformed mesh (in the reference configuration) is reported in each image.

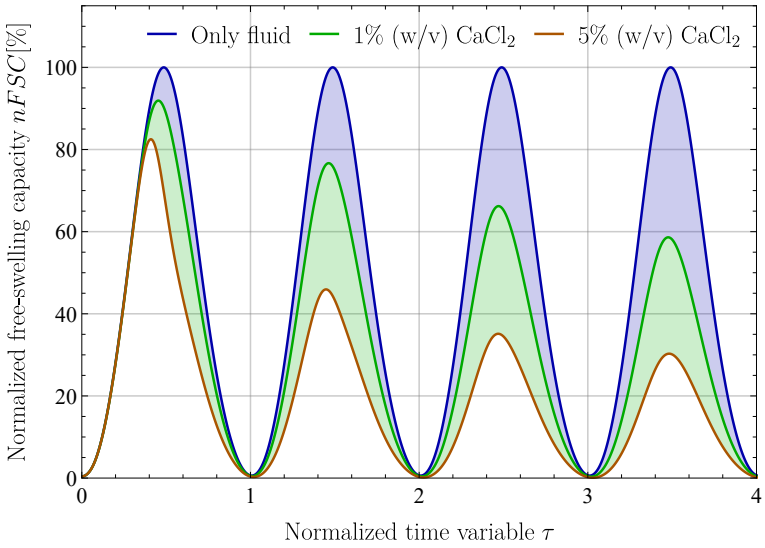

Figure 5.6: Normalized free-swelling capacity $nFSC$ (%) versus the normalized time variable $\tau = t/\tau_d$ (corresponding to different absorption-desorption cycles n_c). Results address four different cases, associated with different assigned boundary calcium concentrations $\tilde{C}_c$, corresponding to only-fluid (i.e., 0%), and solutions with 1%, 2% and 5% (w/v) calcium chloride $CaCl_2$. Values of parameters are given in Table 5.1. Simulation settings: $\mu_f^{bath} = \bar{\mu}_f$ and $q = 0$.

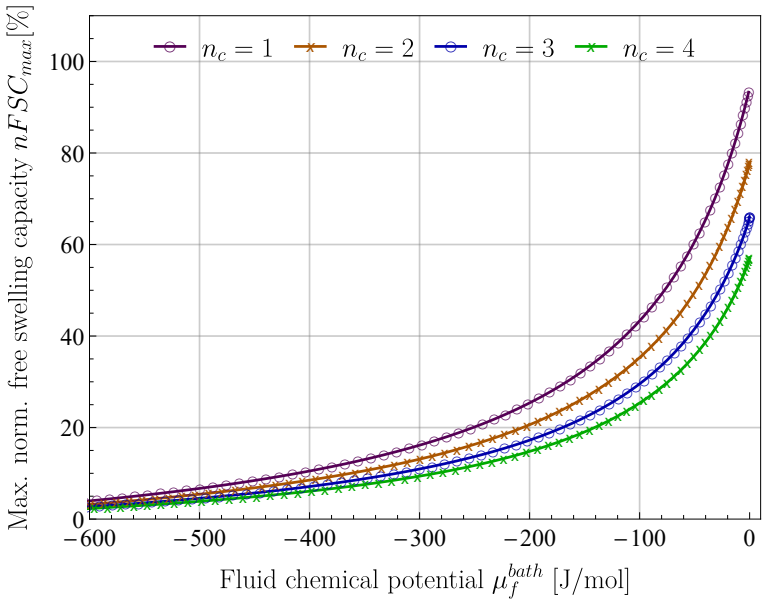

Figure 5.7: Maximum normalized free swelling capacity $nFSC_{max}$ (%) over the four cycles and versus the fluid chemical potential μ_f^{bath} in the bath. Parameters' values in Table 5.1. Simulation settings: $\tilde{C}_c = 1\%$ (w/v) and $q = 0$.

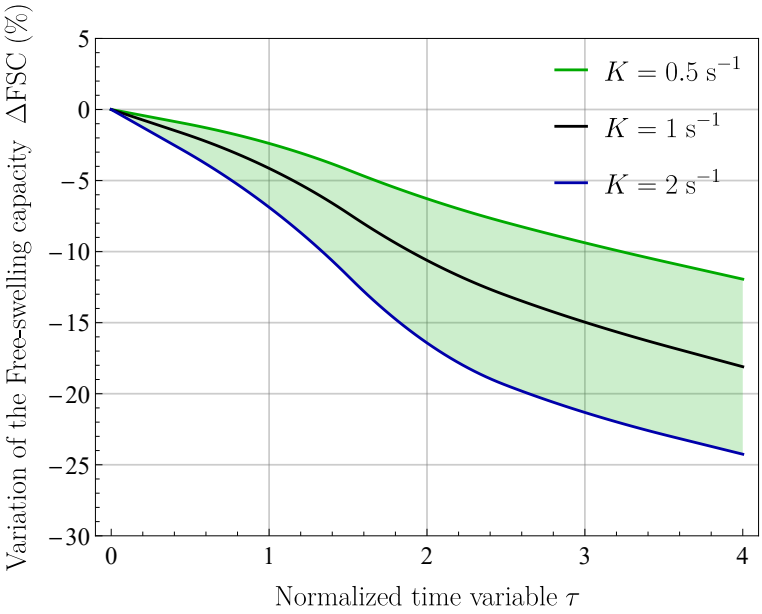

Figure 5.8: Variation of the free-swelling capacity ΔFSC over the normalized time variable $\tau \in [0, 4]$. Results address different values of reaction rates K. If not differently specified, parameters' values are given in Table 5.1. Simulation settings correspond to the reference case study: $\mu_f^{bath} = \bar{\mu}_f$, $\tilde{C}_c = 1\%$ (w/v), and $q = 0$.

Here, J_{fluid} is the local volume change obtained in the only-fluid case.

5.2.5 Crosslinking kinetics

As regards the crosslinking kinetics, results in Fig. 5.8 and Fig. 5.9 show that the reduction of the free-swelling capacity is directly proportional to the reaction rate K and the chemo-mechanical coupling modulus κ_α. This outcome is explained by the evolution of the gelation degree α within the construct, as shown in Figs. 5.10-5.12. In detail, Fig. 5.10 and Fig. 5.11 report α at the centre of the construct over the time path, while Fig. 5.13, Fig. 5.12 report α at the end of each cycle n_c along the normalized length X/L_o at $Y = Z = L_o/2$. An higher gelation degree corresponds to an higher reduction of the free-swelling capacity, since J_{fc} is inversely proportional to α. In turn, an higher gelation degree is obtained, for instance, when the reaction rate K increases. As shown in Fig. 5.14, the crosslinking kinetics is, for the case under investigation, directly proportional to κ_α since the chemo-mechanical term $\hat{p}$ is negative within the specimen, essentially because of the negative pressure exerted by the fluid (i.e., $\hat{p} \approx \bar{p} < 0$).
It is worth highlighting that the chemo-mechanical coupling can even induce a premature interruption of the chemical reaction with respect to a purely chemical description. The reaction rate in Eq. (3.59) indeed stops (i.e., $\dot{\alpha} = 0$) when $\alpha \to 1 + \hat{p}$ and the end value results $\alpha_{end} = \min(1, 1+\hat{p})$. When $\hat{p} < 0$, as in this case, it then results $\alpha_{end} < 1$. As shown in Fig. 5.9, this outcome can be clearly observed for $\kappa_\alpha = 0.1$ MPa, for which the gelation degree tends towards an asymptotic value $\alpha_{end} < 0.4$.

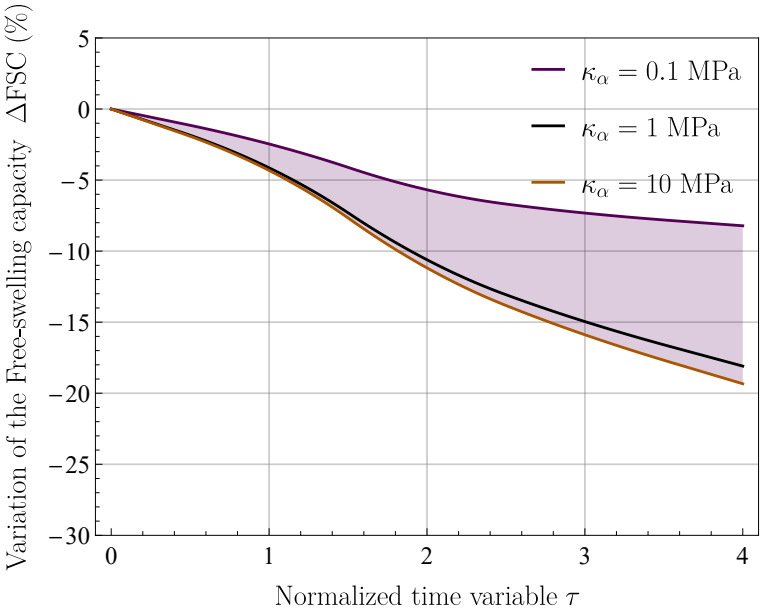

Figure 5.9: Variation of the free-swelling capacity ΔFSC over the normalized time variable $\tau \in [0, 4]$. Results address different values of the chemo-mechanical coupling modulus κ_α. If not differently specified, parameters' values are given in Table 5.1. Simulation settings correspond to the reference case study: $\mu_f^{bath} = \bar{\mu}_f$, $\tilde{C}_c = 1\%$ (w/v), and $q = 0$.

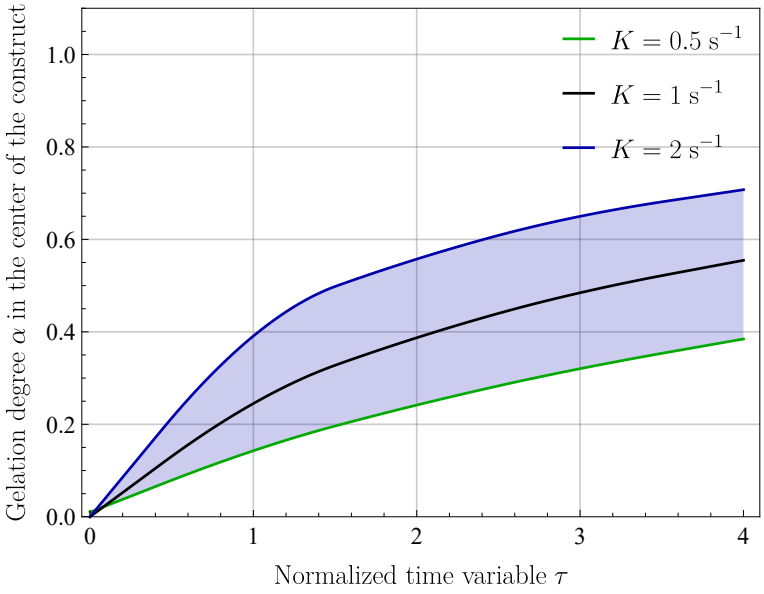

Figure 5.10: Gelation degree α in the center of the construct over the normalized time variable $\tau \in [0, 4]$. Results address different values of reaction rates K. If not differently specified, parameters' values are given in Table 5.1. Simulation settings correspond to the reference case study: $\mu_f^{bath} = \bar{\mu}_f$, $\tilde{C}_c = 1\%$ (w/v), and $q = 0$.

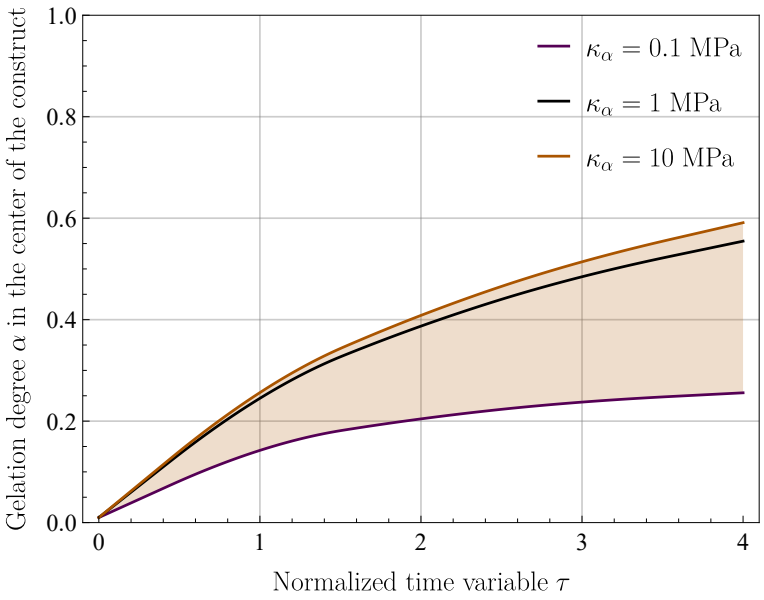

Figure 5.11: Gelation degree α in the center of the construct over the normalized time variable $\tau \in [0, 4]$. Results address different values of the chemo-mechanical coupling modulus κ_α. If not differently specified, parameters' values are given in Table 5.1. Simulation settings correspond to the reference case study: $\mu_f^{bath} = \bar{\mu}_f$, $\tilde{C}_c = 1\%$ (w/v), and $q = 0$.

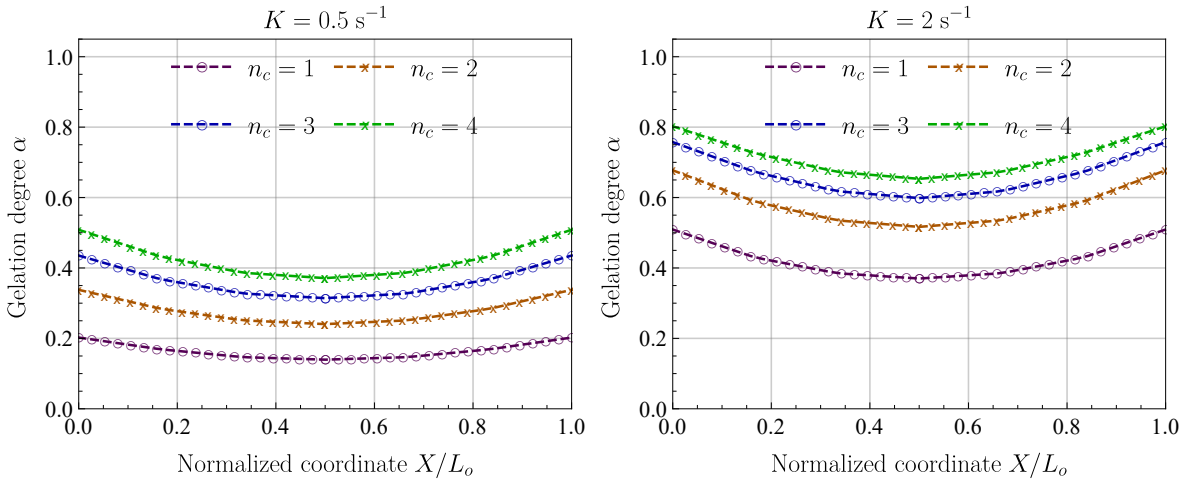

Figure 5.12: Effect of the reaction rate K on gelation degree α along construct width (i.e., along the normalized coordinate X/L_o at $Y = Z = L_o/2$) at the end of each cycle $n_c = 1, \ldots, 4$. If not differently specified, parameters' values are given in Table 5.1. Simulation settings correspond to the reference case study: $\mu_f^{bath} = \bar{\mu}_f$, $\tilde{C}_c = 1\%$ (w/v), and $q = 0$.

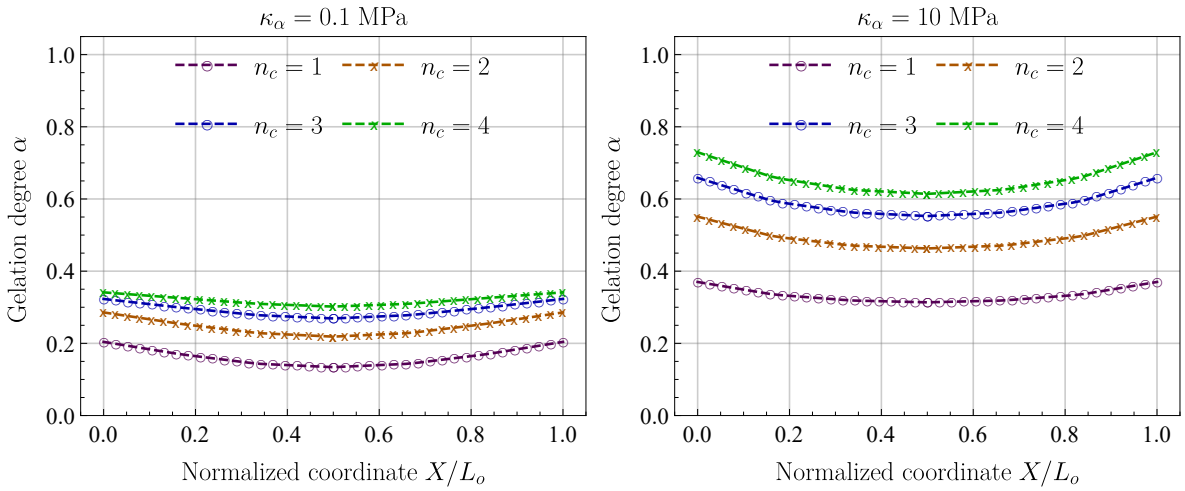

Figure 5.13: Effect of the chemo-mechanical coupling modulus κ_α on gelation degree α along construct width (i.e., along the normalized coordinate X/L_o at $Y = Z = L_o/2$) at the end of each cycle $n_c = 1, \ldots, 4$. If not differently specified, parameters' values are given in Table 5.1. Simulation settings correspond to the reference case study: $\mu_f^{bath} = \bar{\mu}_f$, $\tilde{C}_c = 1\%$ (w/v), and $q = 0$.

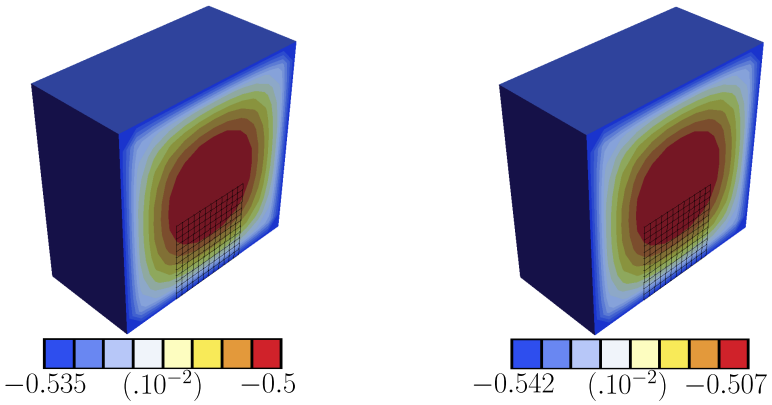

(a) $\hat{p}$ [MPa] (b) $\bar{p}$ [MPa]

Figure 5.14: Mechanical quantities affecting chemical reactions: pressure-like coupling term $\hat{p}$ and pressure $\bar{p}$ at $t = t_{ab}$ at $n_c = 1$. If not differently specified, parameters' values are given in Table 5.1. Simulation settings correspond to the reference case study: $\mu_f^{bath} = \bar{\mu}_f$, $\tilde{C}_c = 1\%$ (w/v), and $q = 0$.

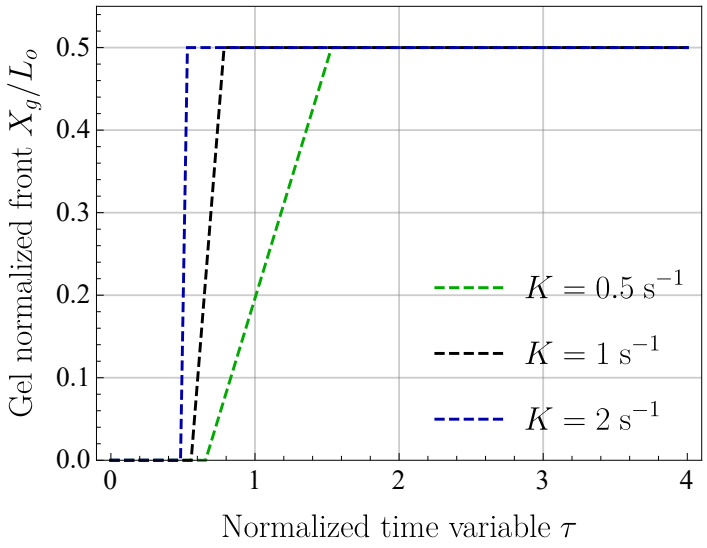

Figure 5.15: Gel front X_g (normalized with respect to reference cube width L_o) over the normalized time variable $\tau \in [0, 4]$ for different values of reaction rate K. If not differently specified, parameters' values are given in Table 5.1. Simulation settings correspond to the reference case study: $\mu_f^{bath} = \bar{\mu}_f$, $\tilde{C}_c = 1\%$ (w/v), and $q = 0$.

A classical way of measuring the extent of the crosslinking reaction in hydrogels is the gel front's propagation rate. The diffusion of calcium in the setting at hand induces the gellified region's propagation from the lateral surfaces to the center. The position of the gel front is then here measured as the coordinate $X = X_g$ at which $\alpha \geq \alpha_{\text{gel}}$ for $X \leq X_g$ (for a fixed $Y = Z = L_o/2$). The evolution of the gel front X_g inside the hydrogel cube during the simulation is shown for different values of K in Fig. 5.15 and κ_α in Fig. 5.16. These results confirm that the propagation of the gel front is faster, with increasing K (as expected), but also with higher values of κ_α. It is interesting to notice that the gel front continues to propagate also during the desorption phases (e.g., $\tau \in [0.5, 1]$ or $\tau \in [1.5, 2]$) because, although there is no more calcium influx, free calcium ions remain in the hydrogel and continue to diffuse and react.

5.2.6 Inelastic rearrangement of the polymer network

Figures 5.17, 5.18 present the results of the parametric study on ratio $r_\Lambda = \Lambda_1/\Lambda_0$, describing swelling reduction due to crosslinking, and the shrinking parameter Γ. In detail, the variation of the free-swelling capacity ΔFSC through the absorption-desorption cycles is reported. Due to crosslinking mechanisms, swelling is highly affected by the inelastic rearrangement of the crosslinked polymer network, both for swelling-related (i.e., r_Λ) and for shrinking-related (i.e., Γ) effects.

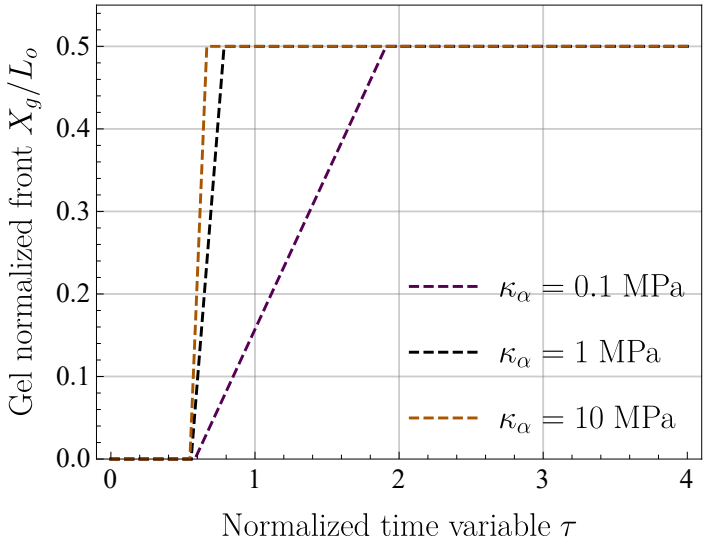

Figure 5.16: Gel front X_g (normalized with respect to reference cube width L_o) over the normalized time variable $\tau \in [0, 4]$ for different values of chemo-mechanical coupling modulus κ_α. If not differently specified, parameters' values are given in Table 5.1. Simulation settings correspond to the reference case study: $\mu_f^{bath} = \bar{\mu}_f$, $\tilde{C}_c = 1\%$ (w/v), and $q = 0$.

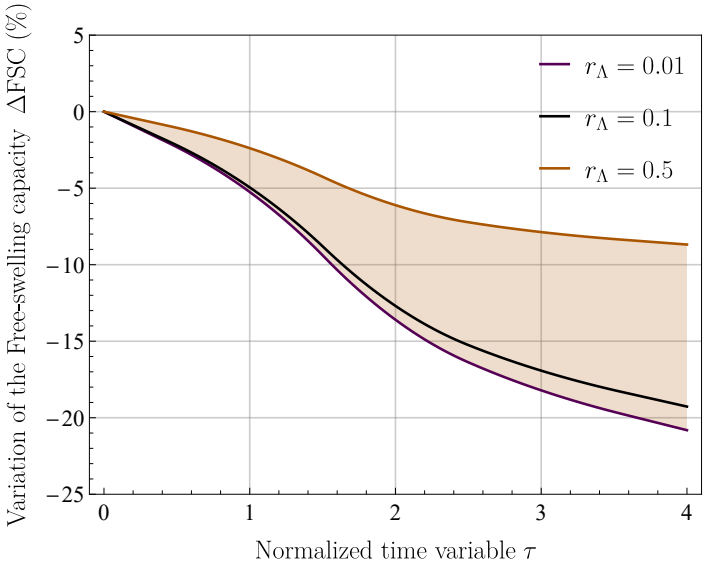

Figure 5.17: Inelastic rearrangement of the polymer network: variation of the free-swelling capacity ΔFSC over the normalized time variable $\tau \in [0, 4]$. Results address different values of ratio $r_\Lambda = \Lambda_1/\Lambda_0$. If not differently specified, parameters' values are given in Table 5.1. Simulation settings correspond to the reference case study: $\mu_f^{bath} = \bar{\mu}_f$, $\tilde{C}_c = 1\%$ (w/v), and $q = 0$.

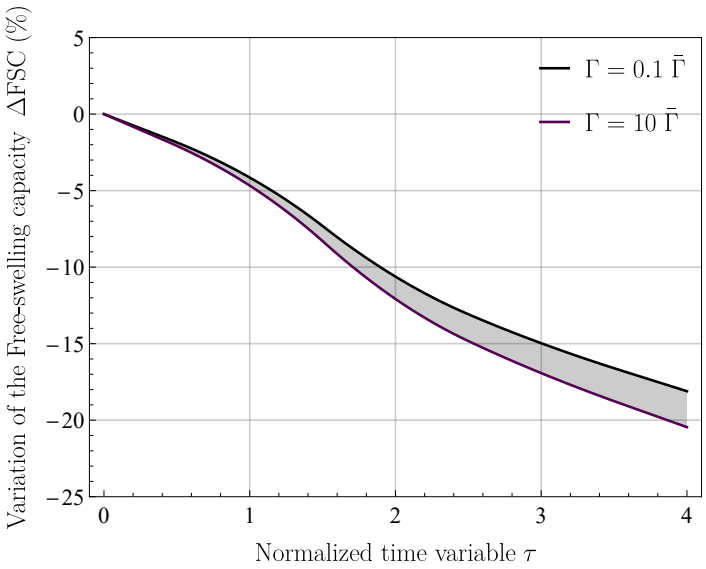

Figure 5.18: Inelastic rearrangement of the polymer network: variation of the free-swelling capacity ΔFSC over the normalized time variable $\tau \in [0, 4]$. Results address different values of the shrinking parameter Γ. If not differently specified, parameters' values are given in Table 5.1. Simulation settings correspond to the reference case study: $\mu_f^{bath} = \bar{\mu}_f$, $\tilde{C}_c = 1\%$ (w/v), and $q = 0$.

5.2.7 Effect of mechanical actions

This section investigates the effects of external mechanical actions on the chemo-mechanical response of hydrogels undergoing crosslinking. An external uniform pressure $q \neq 0$ is considered, and results are shown in Figs. 5.19-5.22. At first, the only-fluid case is addressed. The overall volume increase with $q \neq 0$ is around 70% of the variation obtained with $q = 0$, revealing a reduced fluid absorbance capacity due to compressive external actions (associated with the pressure term in the fluid chemical potential, see Eq. (3.36b)). In the only-fluid case, these mechanisms repeat unaffectedly through the different cycles.
On the other hand, when a crosslinking agent is immersed in the bath, the phenomenological behavior is different. As for the case $q = 0$, the free-swelling capacity reduces through the test due to crosslinking. Besides, the effects of loading (i.e., a reduced fluid absorbance capacity) decrease through the cycles, as shown by the fact that the curves with $q = 0$ and $q \neq 0$ progressively coincide. It is likely due to the polymer chain's stiffening as long as the crosslinking reaction kinetics evolves (i.e., $G_p(\alpha)$ increases with α). Further, the change of the local volume (i.e., $J = \det\mathbf{F}$) and the polymer shear modulus G_p after the desorption cycles for the case $q \neq 0$ are shown in Fig. 5.23 and Fig. 5.24, respectively. Finally, numerical simulations' most remarkable effect is the evidence of an acceleration of the chemical reaction with $q \neq 0$. In fact, the external uniform pressure q increases the value of the pressure term $\bar{p}$, and then of $\dot{\alpha}$ in Eq. (3.59). This phenomenon is shown in Fig. 5.20 and 5.21, respectively in terms of the time-evolution of the gelation degree in the middle of the specimen and the gel front propagation. This outcome highlights the relevance of accounting for chemo-mechanical coupling mechanisms, as addressed in the current work.

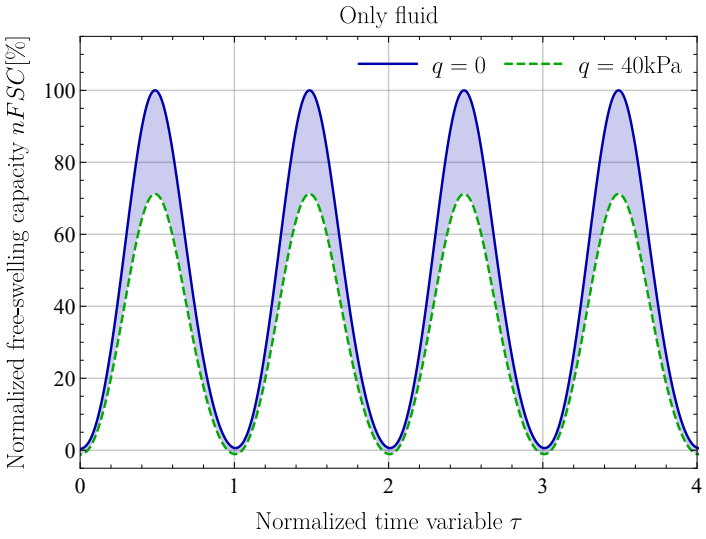

Figure 5.19: Effect of external mechanical actions: swelling capacity in the only-fluid case with $\tilde{C}_c = 1\%$ (w/v) calcium. Parameters' values are given in Table 5.1. Simulation settings: $\mu_f^{bath} = \bar{\mu}_f$.

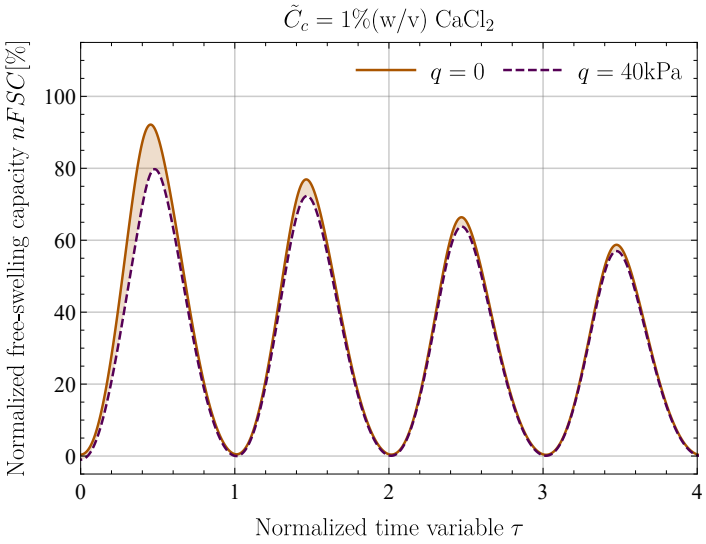

Figure 5.20: Effect of external mechanical actions: swelling capacity in the only-fluid case with $\tilde{C}_c = 1\%$ (w/v) calcium. Parameters' values are given in Table 5.1. Simulation settings: $\mu_f^{bath} = \bar{\mu}_f$.

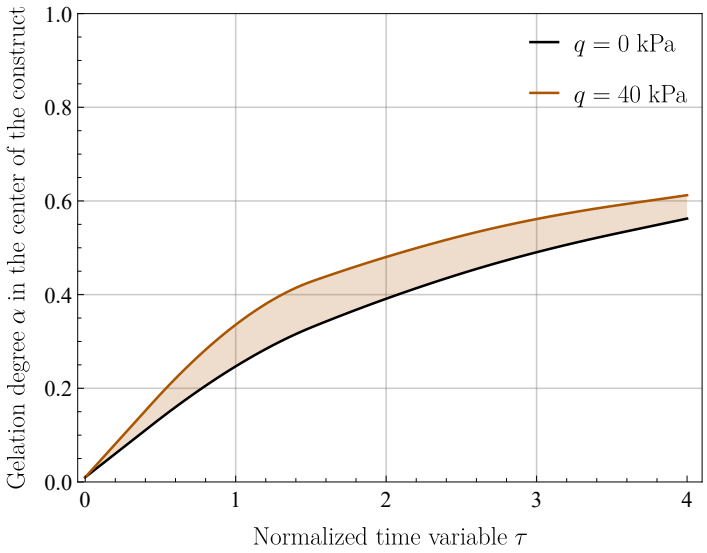

Figure 5.21: Effect of external mechanical actions: gelation degree with $\tilde{C}_c = 1\%$ (w/v) calcium. Parameters' values are given in Table 5.1. Simulation settings: $\mu_f^{bath} = \bar{\mu}_f$.

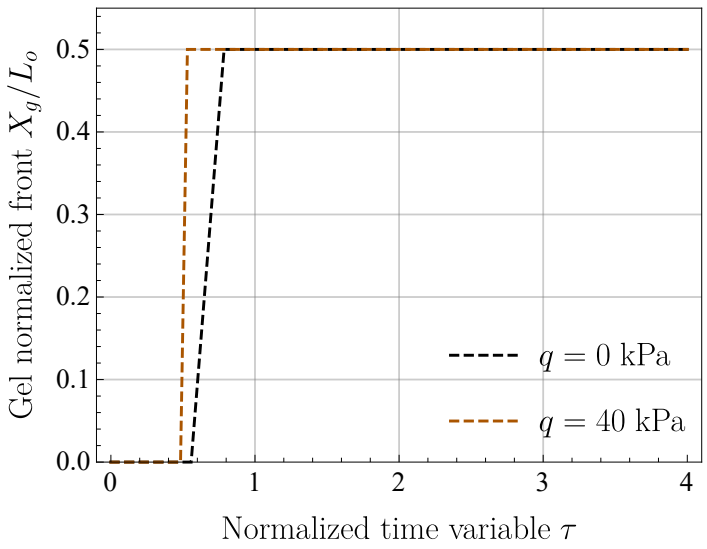

Figure 5.22: Effect of external mechanical actions: gel front propagation with $\tilde{C}_c = 1\%$ (w/v) calcium. Parameters' values are given in Table 5.1. Simulation settings: $\mu_f^{bath} = \bar{\mu}_f$.

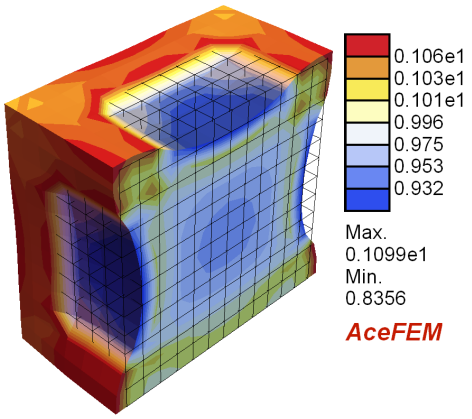

(a) $t = t_{de}$ at $n_c = 1$

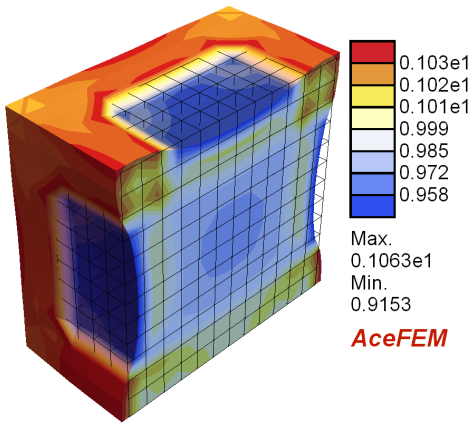

(b) $t = t_{de}$ at $n_c = 2$

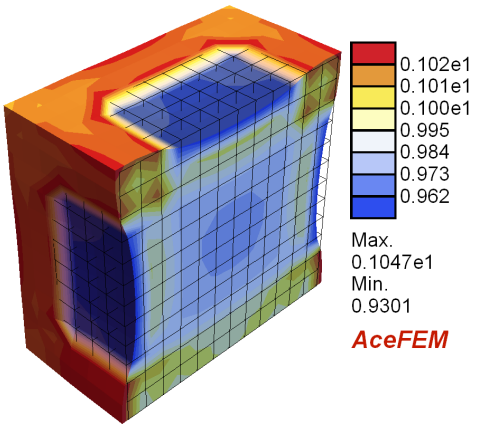

(c) $t = t_{de}$ at $n_c = 3$

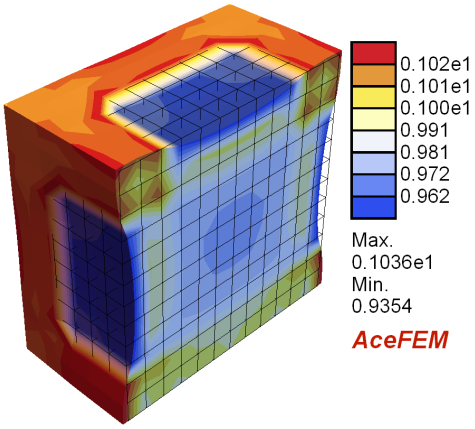

(d) $t = t_{de}$ at $n_c = 4$

Figure 5.23: Local volume change, i.e. $J = \det\mathbf{F}$, after the first (a), second (d), third (e) and fourth (f) desorption phase. Simulation settings correspond to the reference case study: $\mu_f^{bath} = \bar{\mu}_f$, $\tilde{C}_c = 1\%$ (w/v) and $q = 40$ Mpa. The undeformed mesh (in the reference configuration) is reported in each image.

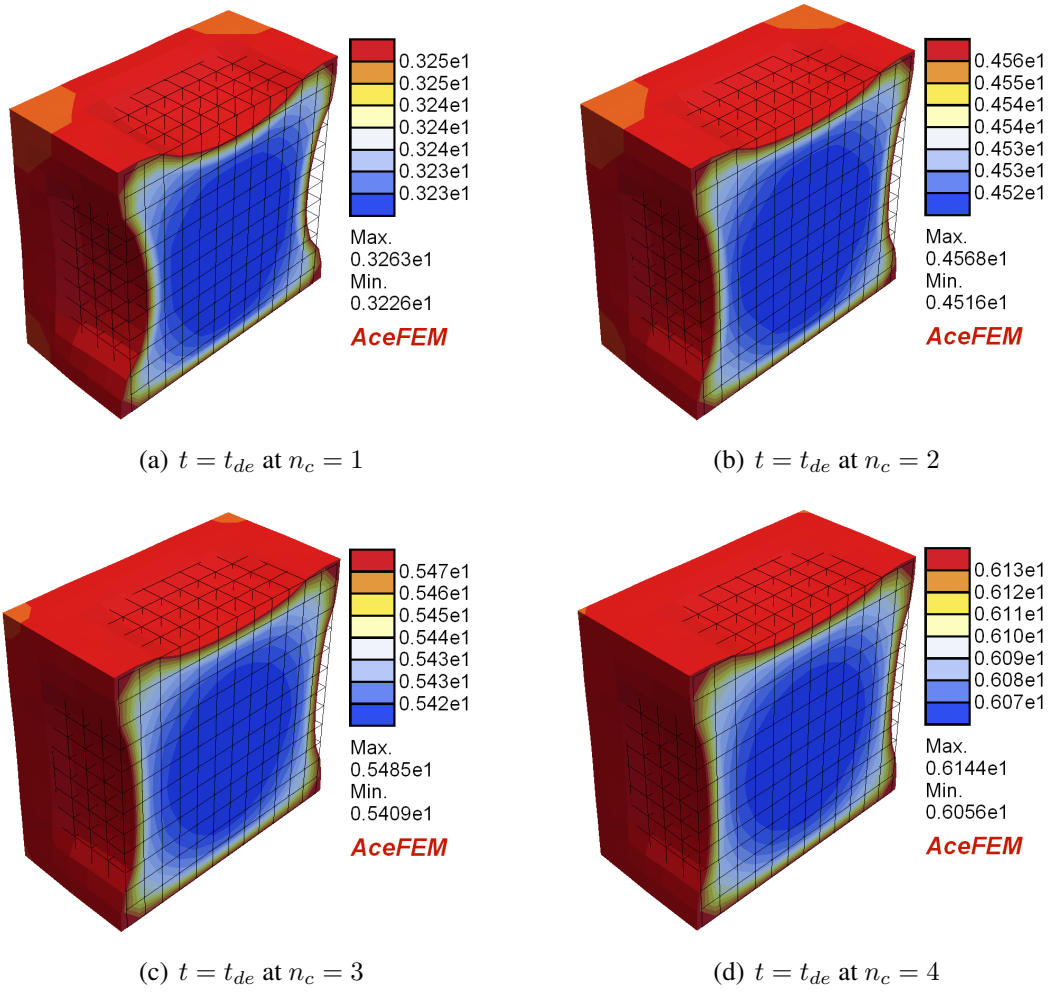

(a) $t = t_{de}$ at $n_c = 1$

(b) $t = t_{de}$ at $n_c = 2$

(c) $t = t_{de}$ at $n_c = 3$

(d) $t = t_{de}$ at $n_c = 4$

Figure 5.24: Chemo-mechanical in the hydrogel after the first (a), second (d), third (e) and fourth (f) desorption phase: polymer shear modulus G_p normalized with respect to the reference value G_p^0 (b). Simulation settings correspond to the reference case study: $\mu_f^{bath} = \bar{\mu}_f$, $\tilde{C}_c = 1\%$ (w/v) and $q = 40$ Mpa. The undeformed mesh (in the reference configuration) is reported in each image.

5.3 Buckling of hydrogel tubes

The next example is introduced based on the experiment conducted by LEE ET AL. (2012) on hydrogel tubes. The experiment is composed of cylindrical hydrogel tubes with mechanically constrained one end; meanwhile, the other end is in contact with fluid for swelling and possibly buckling. By changing the tubes' geometry such as wall thickness, radius, and heights, LEE ET AL. (2012) found different formations of buckled patterns on the swollen ends of the hydrogel tubes. The mentioned experimentally-observed buckled patterns can be modelled by introducing the first geometry which is a cylindrical tube, as shown in Fig. 5.25, with $\{h_c,\, R_c,\, t_c\} = \{1.2,\, 4.45,\, 0.283\}$ mm, similar to those reported in the paper of LEE ET AL. (2012). The second geometry is defined by adopting $\{h_c,\, R_c,\, t_c\} = \{2.4,\, 4.45,\, 0.143\}$ mm. These two geometries are introduced to obtain different buckling responses. Geometries are chosen such to respect $\pi h_c((R_c + t_c)^2 - R_c^2) = V_o$, with V_o defined from the as-prepared state.

Addressing the absorption-desorption kinetics (see Section 5.1), the duration of each cycle is determined as $\tau_d = h_c^2/\bar{D}_f$, resulting in ca. $\tau_d = 0.8$ hours. For each cycle $n_c = 1, \ldots, 4$, the time-varying boundary conditions in Eq. (5.1) are applied on the outer surface S_1 at $Z = h_c$ (see Fig. 5.25). On the other surfaces (i.e., $\{S_2, S_3, S_4\} = \partial\mathcal{B}_o \setminus S_1$), a constant chemical potential (μ_f^{air}) and a null calcium flux are enforced at any time. A minimal set of boundary conditions are applied for the mechanical constraint to prevent the rigid body motions. Further, the bottom surface at $Z = 0$ is constrained similarly to the experimental work of LEE ET AL. (2012).

The computational framework is discretized by utilizing a structured mesh of H1 elements with a total number of degrees of freedom equal to 11520. A schematic representation of the numerical case study is shown in Fig. 5.25. When it is not differently specified, the reference simulation values are selected as $\mu_f^{bath} = \bar{\mu}_f$, which is the bath fluid chemical potential equal to the reference fluid one; a concentration $\tilde{C}_c = 1\%$ (w/v) of calcium chloride in the solution. For initiating the buckling, all nodes on the front face of the cylindrical tube are given a small random geometric imperfection with the order of 10^{-2} mm in height h_c dimension.

5.3.1 Impact of calcium chloride $CaCl_2$ solution on buckling

As shown in Fig. 5.26, the local volume change J and the gelation degree α for the first geometrical variation $\{h_c,\, R_c,\, t_c\} = \{1.2,\, 4.45,\, 0.29\}$ mm for the first and fourth absorption cycle with $\mu_f^{bath} = \bar{\mu}_f$, $\tilde{C}_c = 1\%$ (w/v) are described. Meanwhile, Fig. 5.27 illustrates the local volume change J and the gelation degree α for the second geometrical variation $\{h_c,\, R_c,\, t_c\} = \{2.4,\, 4.45,\, 0.14\}$ mm for the first and fourth absorption cycle considering $\mu_f^{bath} = \bar{\mu}_f$, $\tilde{C}_c = 1\%$ (w/v). After the first absorption phase (i.e. $n_c = 1$), the shapes in Figs. 5.26(a,c) with the first geometry results in buckled hydrogel tube and in Figs. 5.27(a,c) with the second geometry results in axisymmetrically swollen hydrogel tube. Those shapes resemble the observed experiments by LEE ET AL. (2012), recovering the evidence that buckling depends on geometrical factors. However, buckling depends also on the crosslinking kinetics which affects gel stiffness, and in turn swelling stretch. The effect of crosslinking on buckling is demonstrated by numerical simulations, as reported in Figs. 5.26(b,d) which

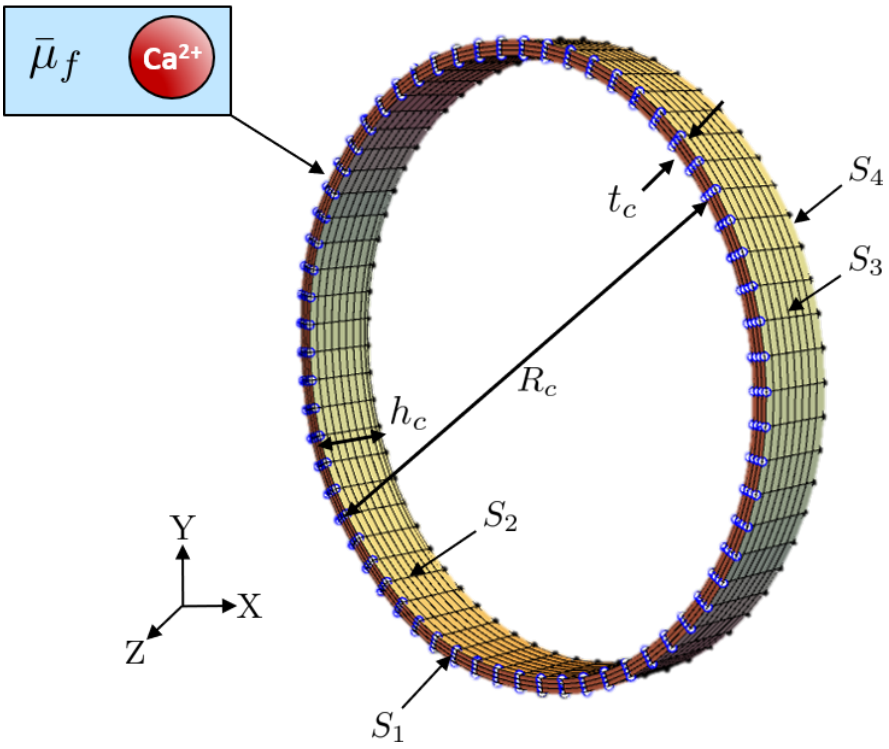

Figure 5.25: Numerical simulations set-up: isometric view of the cylindrical tube, mesh details, boundary conditions schematic. Four absorption-desorption cycles are considered. In each cycle, the hydrogel tube is immersed in a bath of calcium chloride $CaCl_2$ solution during the absorption phase, undergoing swelling-crosslinking mechanisms, and removed from the bath during the desorption process. *As-prepared* initial conditions, as detailed in Table 5.1, are considered.

show that, after four cycle of absorption-desorption with $\tilde{C}_c = 1\%$ (w/v) calcium chloride concentration, the buckling pattern for the first geometry is reduced. Further, Figs. 5.27(b,d) depicts the effect of calcium chloride concentration $\tilde{C}_c = 1\%$ (w/v) on the decreased local volume J for the second geometry. These simulations results demonstrates the capability of developed computational model in investigating complex nonlinear elastic phenomena of gel structure as a result of coupled chemo-mechanical mechanisms.

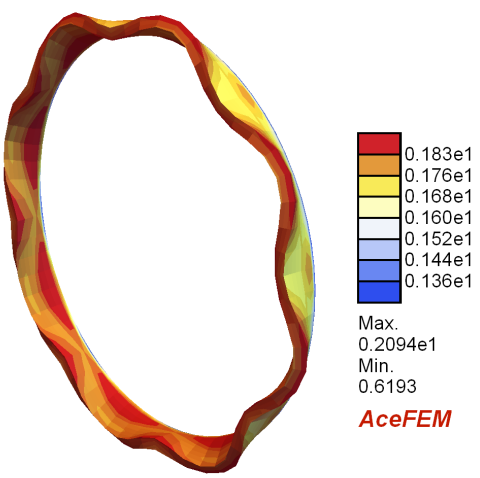

(a) $t = t_{ab}$ at $n_c = 1$

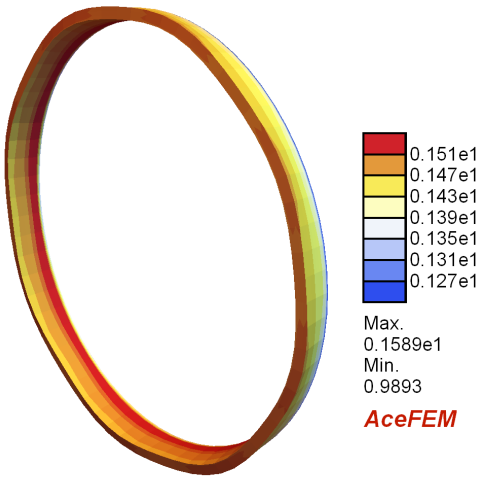

(b) $t = t_{ab}$ at $n_c = 4$

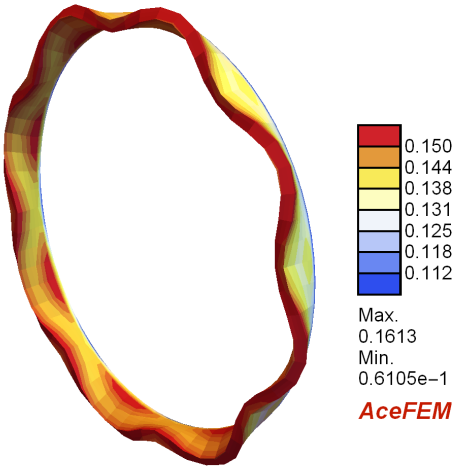

(c) $t = t_{ab}$ at $n_c = 1$

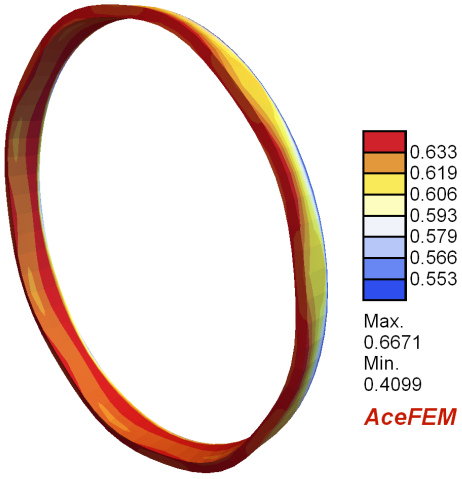

(d) $t = t_{ab}$ at $n_c = 4$

Figure 5.26: Chemo-mechanical response of the hydrogel tube for the first geometry after the first (a,c), and fourth (b,d) absorption phase (i.e. $t = t_{ab}$): Local volume change, i.e. $J = \det\mathbf{F}$ (a,b), and gelation degree α (c,d). Simulation settings correspond to the reference case study: $\{h_c,\ R_c,\ t_c\} = \{1.2,\ 4.45,\ 0.283\}$ mm, $\mu_f^{bath} = \bar{\mu}_f$, $\tilde{C}_c = 1\%$ (w/v).

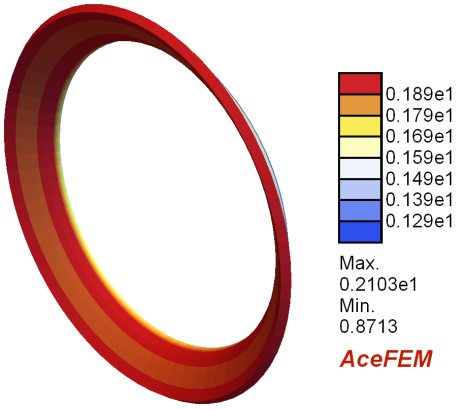

(a) $t = t_{ab}$ at $n_c = 1$

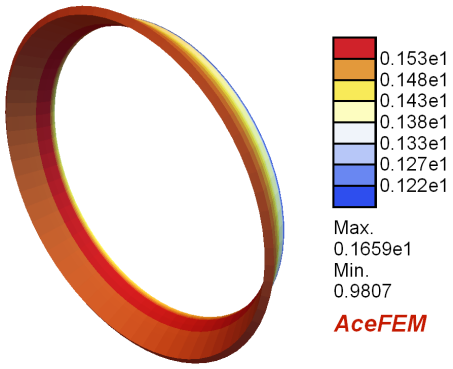

(b) $t = t_{ab}$ at $n_c = 4$

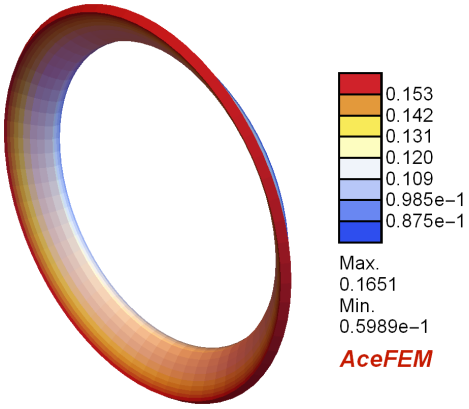

(c) $t = t_{ab}$ at $n_c = 1$

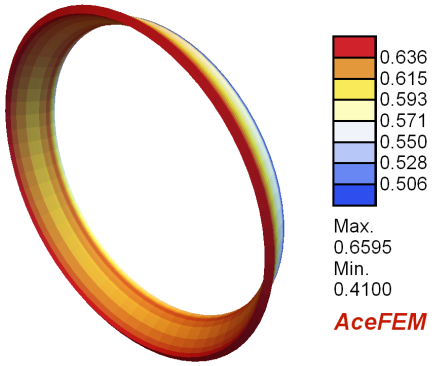

(d) $t = t_{ab}$ at $n_c = 4$

Figure 5.27: Chemo-mechanical response of the hydrogel tube for the second geometry after the first (a,c), and fourth (b,d) absorption phase (i.e. $t = t_{ab}$): Local volume change, i.e. $J = \det\mathbf{F}$ (a,b), and gelation degree α (c,d). Simulation settings correspond to the reference case study: $\{h_c,\ R_c,\ t_c\} = \{2.4,\ 4.45,\ 0.143\}$ mm, $\mu_f^{bath} = \bar{\mu}_f$, $\tilde{C}_c = 1\%$ (w/v).

5.4 Wrinkling of cuboid

In this Section, a hydrogel cuboid structure fixed at two ends is introduced, in which wrinkles appear as a result of mechanical instabilities following swelling (TANAKA ET AL., 1987; GUVENDIREN ET AL., 2010; TOH ET AL., 2015). The cuboid is proposed with a total initial volume of V_o (see Section 5.1), considering two geometries with $\{w_r,\, h_r,\, l_r\} = \{1.252,\, 1.252,\, 6.255\}$ mm and $\{\bar{w}_r,\, \bar{h}_r,\, \bar{l}_r\} = \{0.99,\, 0.99,\, 9.999\}$ mm.
Addressing the absorption-desorption kinetics (see Section 5.1), the duration of each cycle is defined as τ_d which is ca. $\tau_d = 2.5$ hours. Whereas, for each cycle $n_c = 1, \ldots, 4$, the same time-varying boundary conditions from Eq. (5.1) are assigned for the chemical problem on the external surface $\partial\hat{\mathcal{B}}_o = \partial\mathcal{B}_o \setminus \{S_1, S_2\}$, that is the entire boundary apart from the two end surfaces, namely S_1 and S_2 (where null flux boundary conditions are assigned) as shown in Fig 5.28. Regarding the mechanical boundary, rigid body motions are prevented by applying a minimal set of boundary conditions. Similar to the cubic hydrogel problem in Section 5.2, the bottom surface at $Z = 0$ is constrained in the direction identified by $\mathbf{k}$.
A structured mesh of H1 elements has been utilized to discretize the computational domain with a total number of degrees of freedom equal to 11375. A schematic illustration of the case study is shown in Fig. 5.28. The reference simulation values are given as: $\mu_f^{bath} = \bar{\mu}_f$, which is the bath fluid chemical potential equal to the reference fluid one; a concentration $\tilde{C}_c = 2\%$ (w/v) of calcium chloride in the solution.

5.4.1 Influence of $CaCl_2$ solution on wrinkling

The local volume change J for the first geometry $\{w_r,\, h_r,\, l_r\} = \{1.252,\, 1.252,\, 6.255\}$ mm is demonstrated after the first absorption cycle, as shown in Fig. 5.29a, and the fourth absorption cycle, as depicted in Fig. 5.29b, with $\mu_f^{bath} = \bar{\mu}_f$, $\tilde{C}_c = 2\%$ (w/v). Whereas, Fig. 5.30 shows the local volume change J for the second geometry $\{\bar{w}_r,\, \bar{h}_r,\, \bar{l}_r\} = \{1,\, 1,\, 10\}$ mm for the first (Fig. See Fig. 5.30a) and fourth (Fig. See Fig. 5.30b) absorption cycle by applying $\mu_f^{bath} = \bar{\mu}_f$, $\tilde{C}_c = 2\%$ (w/v). After running four cycles of absorption-desorption (i.e. $n_c = 4$) with $\tilde{C}_c = 2\%$ (w/v) calcium chloride concentration, the results in Figs. 5.29(b) for the first geometry depicts reduced wrinkles on top of the hydrogel cuboid. This outcome is similarly observed in Figs. 5.30(b) for the second geometry. Comparing the first geometry in Fig. 5.29a with the second one in Fig. 5.30a, it is noteworthy to mention that the wrinkling effect is deteriorated by increasing the initial length of the cuboid hydrogel confirming previously published evidence (TOOMEY ET AL., 2004; GUVENDIREN ET AL., 2010). Further, Fig.5.31 and Fig.5.32 demonstrate the significant effect of the $CaCl_2$ solution during the absorption-desorption cycles on the polymer shear modulus G_p in Figs.5.31-5.32(a,b), and hence the effect of crosslinking kinetics on the wrinkled patterns. Coupled effects are further highlighted by the highly heterogeneous distribution of the pressure-like coupling term $\hat{p}$ shown in Figs.5.31-5.32(c,d). The illustrated figures, particularly Fig. 5.29a and Fig. 5.30a resemble the observed experimental cases by TANAKA ET AL. (1987); GUVENDIREN ET AL. (2010). Understanding the chemo-mechanical influences on the degree of wrinkles of the hydrogel cuboid elucidates and optimise the creation of the hydrogel-based products in biomedical engineering.

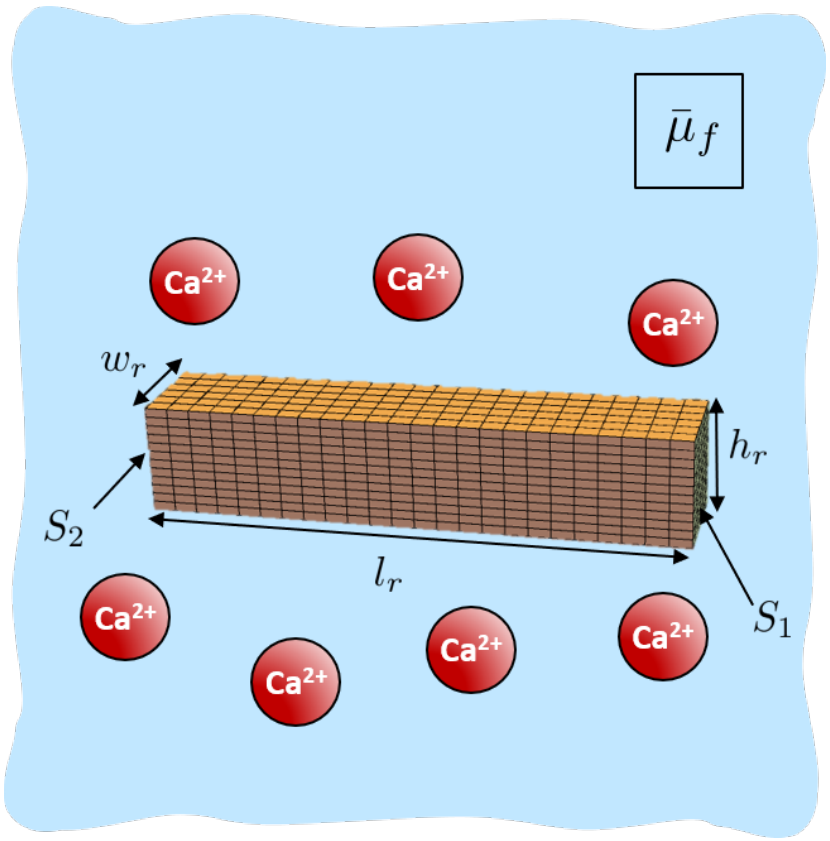

Figure 5.28: Schematic of the numerical simulations set-up: isometric viewpoint of the cuboid specimen with $\{w_r,\ h_r,\ l_r\}$ representing {width, height, length}, respectively, along with mesh details and boundary conditions. Four absorption-desorption cycles are considered: the hydrogel is immersed in a bath of calcium chloride $CaCl_2$ solution during the absorption phase undergoing swelling-crosslinking mechanisms, and removed from the bath during the desorption process. *As-prepared* initial conditions, as detailed given values in Table 5.1, are taken into consideration.

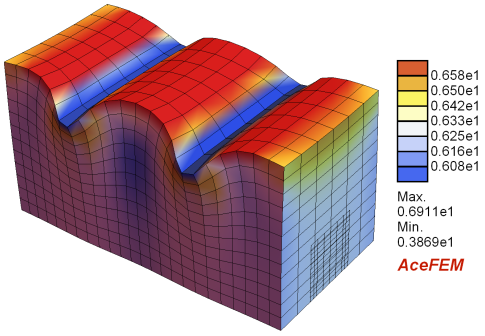

(a) $t = t_{ab}$ at $n_c = 1$

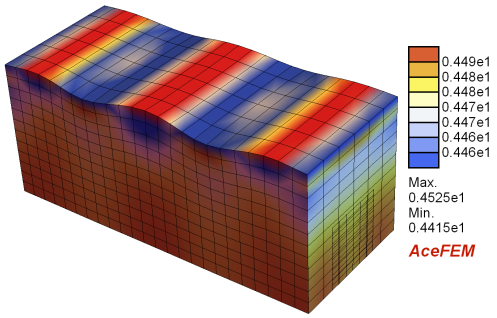

(b) $t = t_{ab}$ at $n_c = 4$

Figure 5.29: Local volume change, i.e. $J = \det\mathbf{F}$ for the first geometry $\{w_r,\, h_r,\, l_r\} = \{1.252,\, 1.252,\, 6.255\}$ mm of the cuboid hydrogel after the first (a) and fourth (b) absorption phase. Simulation settings associated to the reference case study: $\mu_f^{bath} = \bar{\mu}_f$, $\tilde{C}_c = 2\%$ (w/v). The undeformed mesh (in the reference configuration) is reported in each image.

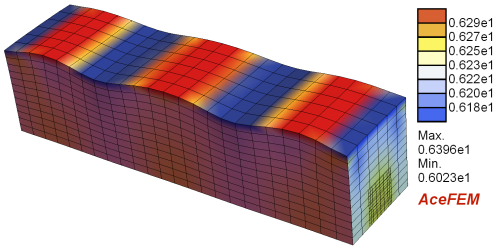

(a) $t = t_{ab}$ at $n_c = 1$

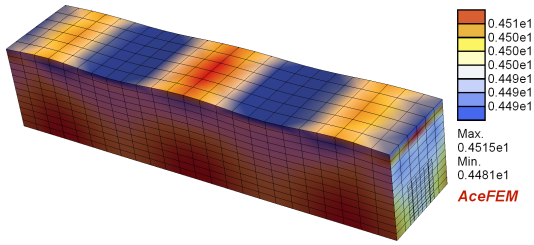

(b) $t = t_{ab}$ at $n_c = 4$

Figure 5.30: Local volume change, i.e. $J = \det\mathbf{F}$ for the second geometry of $\{\bar{w}_r,\, \bar{h}_r,\, \bar{l}_r\} = \{0.99,\, 0.99,\, 9.999\}$ mm of the cuboid hydrogel after the first (a) and fourth (b) absorption phase. Simulation settings associated to the reference case study: $\mu_f^{bath} = \bar{\mu}_f$, $\tilde{C}_c = 2\%$ (w/v). The undeformed mesh (in the reference configuration) is reported in each image.

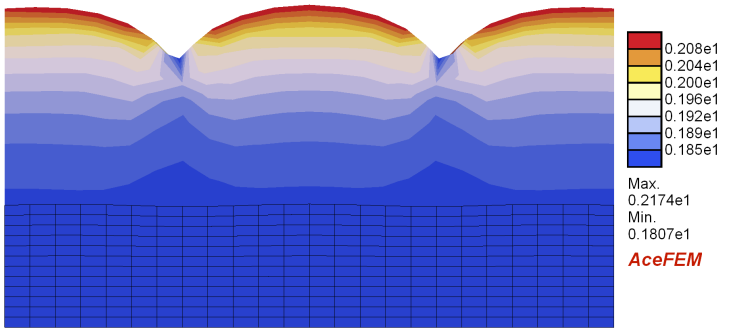

(a) $t = t_{ab}$ at $n_c = 1$

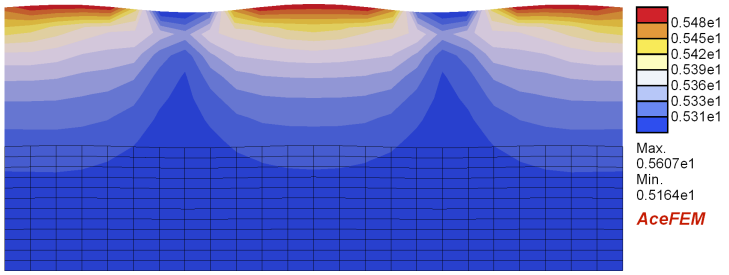

(b) $t = t_{ab}$ at $n_c = 4$

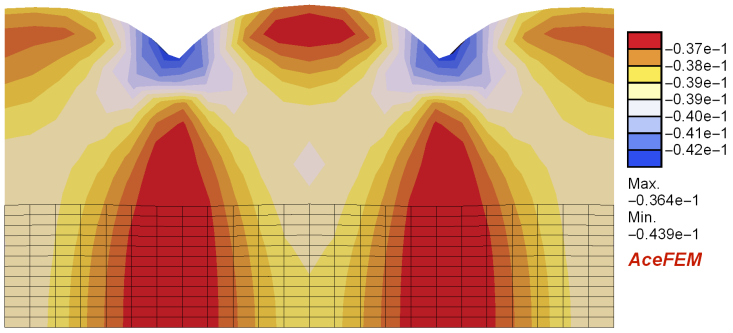

(c) $t = t_{ab}$ at $n_c = 1$

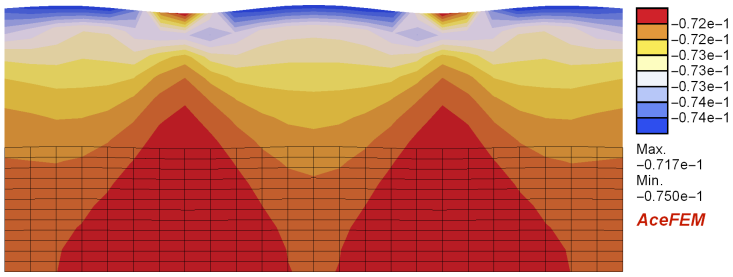

(d) $t = t_{ab}$ at $n_c = 4$

Figure 5.31: Chemo-mechanical coupled effects in the hydrogel cuboid for the first geometry $\{w_r,\, h_r,\, l_r\} = \{1.252,\, 1.252,\, 6.255\}$ mm after the first (a,c), and fourth (b,d) absorption phase (i.e. $t = t_{ab}$): Polymer shear modulus G_p normalized to the reference value G_p^0 (a,b), and pressure-like coupling term $\hat{p}$ (c,d). Simulation set-ups represent the reference case study: $\mu_f^{bath} = \bar{\mu}_f$, $\tilde{C}_c = 2\%$ (w/v). The undeformed mesh (in the reference configuration) is shown in each figure.

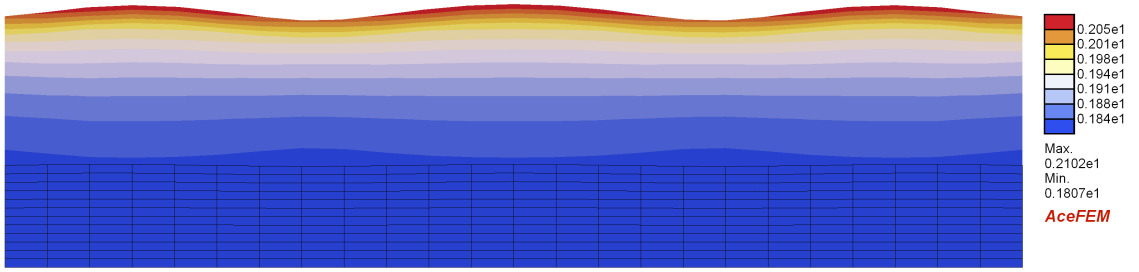

(a) $t = t_{ab}$ at $n_c = 1$

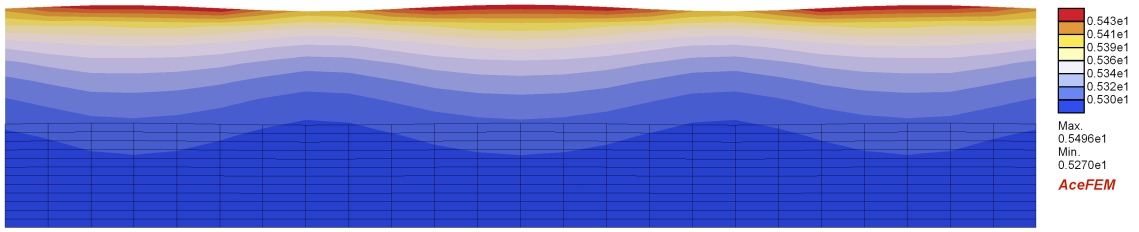

(b) $t = t_{ab}$ at $n_c = 4$

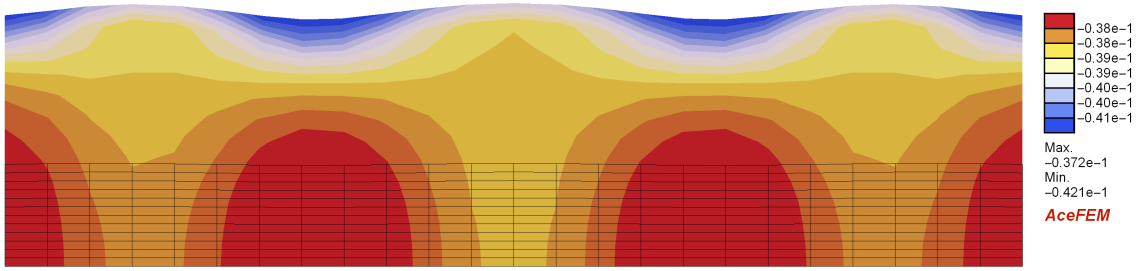

(c) $t = t_{ab}$ at $n_c = 1$

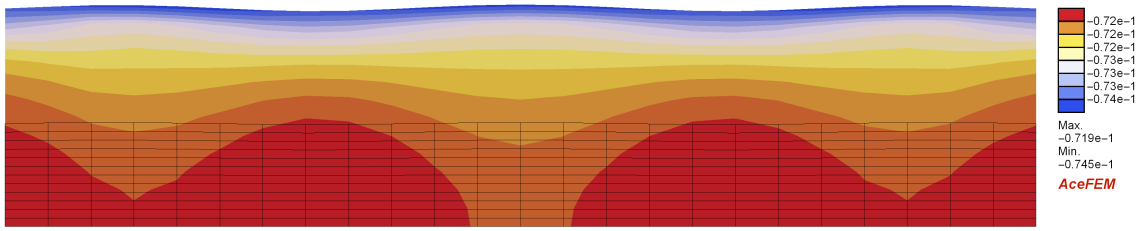

(d) $t = t_{ab}$ at $n_c = 4$

Figure 5.32: Chemo-mechanical coupled effects in the hydrogel cuboid for the second geometry $\{\bar{w}_r,\ \bar{h}_r,\ \bar{l}_r\} = \{0.99,\ 0.99,\ 9.999\}$ mm after the first (a,c), and fourth (b,d) absorption phase (i.e. $t = t_{ab}$): Polymer shear modulus G_p normalized to the reference value G_p^0 (a,b), and pressure-like coupling term $\hat{p}$ (c,d). Simulation set-ups represent the reference case study: $\mu_f^{bath} = \bar{\mu}_f$, $\tilde{C}_c = 2\%$ (w/v). The undeformed mesh (in the reference configuration) is illustrated in each image.

5.5 Bending of a polymeric bilayer bar

The present section considers the experiment conducted by YOON ET AL. (2010) on bending of a bilayer hydrogel bar. Similar experiments have been performed by HOLMES ET AL. (2011); PANDEY & HOLMES (2013). In the experimental setting here considered, a thin layer of a swellable and crosslinkable hydrogel bar is attached to a non-swellable elastomeric bar that is not reacting with the crosslinker, allowing the hydrogel to swell, which results in large bending of the bilayer bar.
The hydrogel bar (see Fig. 5.33) is characterized by $\{w_b,\, h_b,\, l_b\} = \{1,\, 0.49,\, 20\}$ mm, such that the total volume of the hydrogel bar is equal to the initial volume $w_b\, h_b\, l_b \approx V_o$ from the as-prepaid state (see Section 3.9). The non-swellabe elastomeric gel is correspondingly defined with same geometry but modeled with a neo-Hookean hyperelastic constitutive law. As regards the absorption-desorption kinetics (see Section 5.1) the duration of each cycle results ca. $\tau_d = 2.5$ hours. An additional relevant time-point $t_{ab}^{1/4} = (n_c - 1)\tau_d + \tau_d/8$ is proposed at the quartile of the absorption phase. A point in the middle-bottom part of the non-swellable bar is fixed to prevent rigid body motion in (X, Y, Z) considered in the reference configuration.
The numerical model's discretization is implemented with a structured mesh of H1 elements with a total number of degrees of freedom equal to 19565. It is noteworthy to mention that an extension on element technology by implementing an improved EAS (i.e., Enhanced Assumed Strain) brick element for finite deformation in this work, can result in a well-behaved locking and hour-glassing free element formulation (KORELC ET AL., 2010). A schematic representation of the numerical case study is shown in Fig. 5.33. If not differently specified, the reference simulation settings are chosen as $\mu_f^{bath} = \bar{\mu}_f$, that is the bath fluid chemical potential equal to the reference fluid one; a concentration $\tilde{C}_c = 1\%$ (w/v) of calcium chloride in the solution.

5.5.1 $CaCl_2$ effect on the bending of the bilayer bar

The steep local volume change J of the polymeric bilayer bar composed of swellabe hydrogel and non-swellabe elastomeric bars is illustrated in Fig. 5.34 during the first cycle $n_c = 1$ for the time range of the quartile absorption phase $t = t_{ab}^{1/4}$(Fig. 5.34a) at the middle of the absorption phase $t = t_{ab}^{1/2}$ (Fig. 5.34b) at the end of the absorption phase $t = t_{ab}$ (Fig. 5.34c) and over the fourth cycle $n_c = 4$ at the end of the absorption phase $t = t_{ab}$(Fig. 5.34d). Further, Figs. 5.35 (a,b) present the distribution of the crosslinking degree at the end of the first absorption phase which is less than the one at the end of the fourth cycle, respectively. These results determine that the bending of the bilayer bar in Fig. 5.34d is lessen after four cycles $n_c = 4$ compare to Fig. 5.34c due to the effect of crosslinking which increases the shear modulus $G_p(\alpha)$ in the hydrogel bar. These observations are in agreement with the conducted experiment by ZHAO ET AL. (2019).

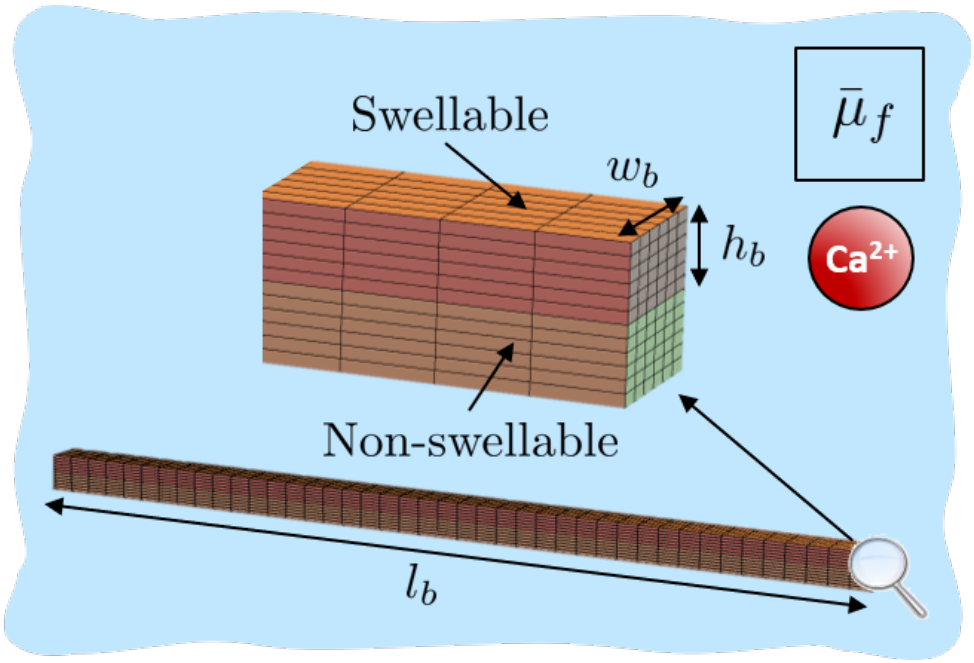

Figure 5.33: Schematic representation of the computational domain: isometric viewpoint of the polymeric bilayer bar including swellabe hydrogel and non-swellabe elastomeric bars with $\{w_r,\ h_r,\ l_r\}$ representing their {width, height, length}, respectively, along with mesh details and boundary conditions. Four absorption-desorption cycles are applied: the hydrogel is immersed in a bath of calcium chloride $CaCl_2$ solution over the absorption phase undergoing swelling-crosslinking mechanisms, and removed from the bath over the desorption process. *As-prepared* initial conditions are considered from the prescribed values in Table 5.1.

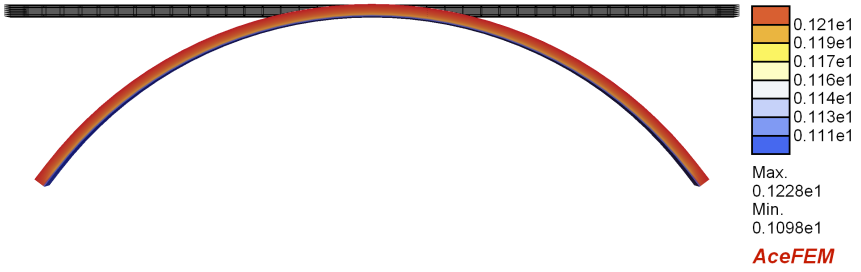

(a) $t = t_{ab}^{1/4}$ at $n_c = 1$

(b) $t = t_{ab}^{1/2}$ at $n_c = 1$

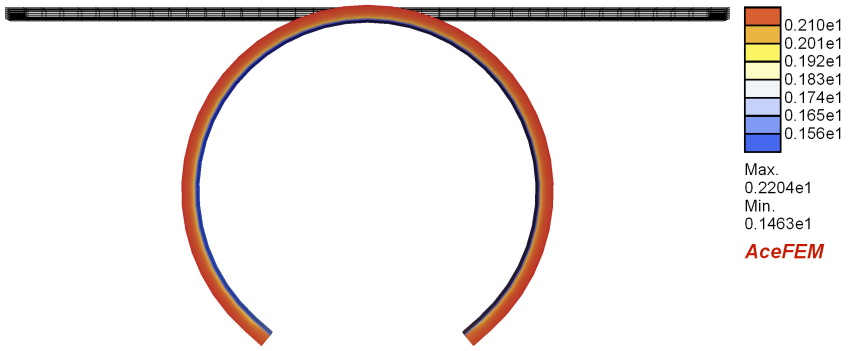

(c) $t = t_{ab}$ at $n_c = 1$

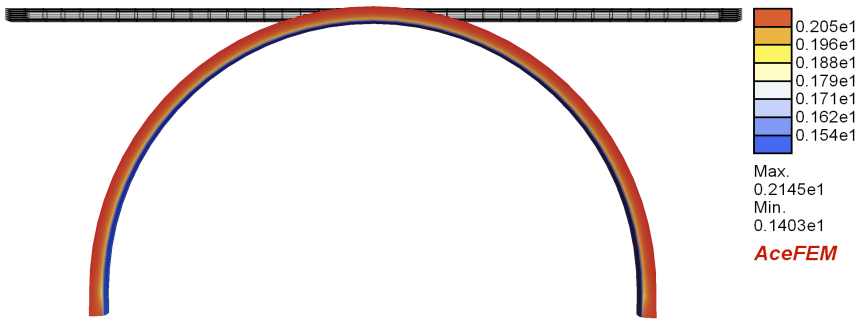

(d) $t = t_{ab}$ at $n_c = 4$

Figure 5.34: Local volume change, i.e. $J = \det\mathbf{F}$ in the hydrogel bar during the first cycle $n_c = 1$ at the quartile of the absorption phase (a) at the middle of the absorption phase (b) at the end of the absorption phase (c) and during the fourth cycle $n_c = 4$ at at the end of the absorption phase (d). Simulation configurations assigned to the reference case study: $\mu_f^{bath} = \bar{\mu}_f$, $\tilde{C}_c = 1\%$ (w/v). The undeformed mesh (in the reference configuration) is showed in each image.

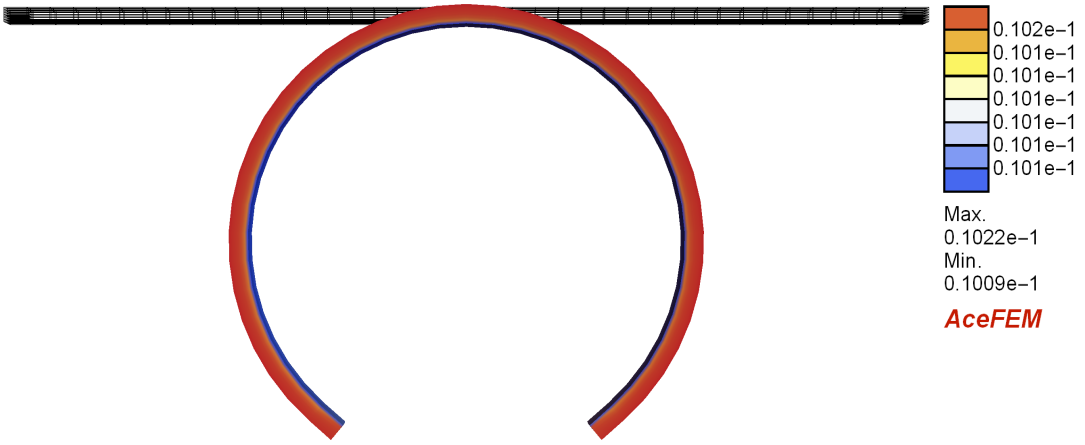

(a) $t = t_{ab}$ at $n_c = 1$

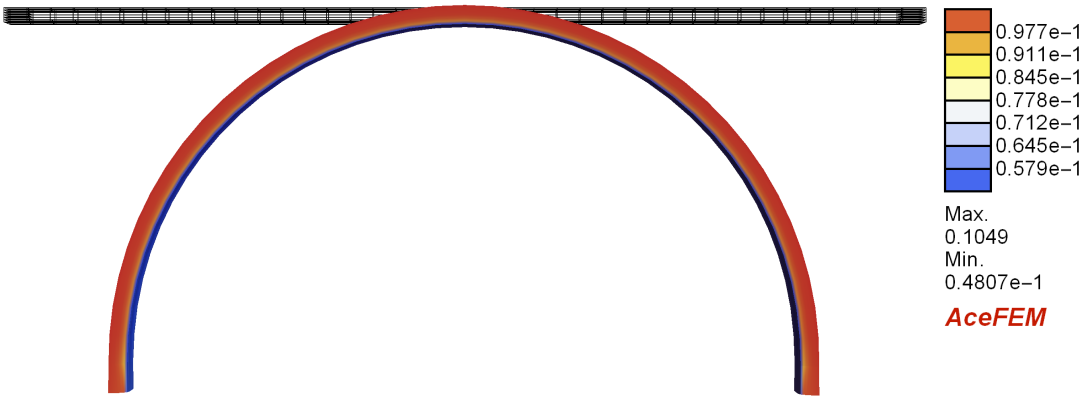

(b) $t = t_{ab}$ at $n_c = 4$

Figure 5.35: Gelation degree α in the hydrogel bar over the first cycle $n_c = 1$ at the end of the absorption phase (a) and over the fourth cycle $n_c = 4$ at the end of the absorption phase (b). Simulation set-up associated with the reference case study: $\mu_f^{bath} = \bar{\mu}_f$, $\tilde{C}_c = 1\%$ (w/v). The undeformed mesh (in the reference configuration) is demonstrated in each image.

5.6 Spherical gel confined swelling

In this example, the focus is on spherical hydrogel confined swelling. BERTRAND ET AL. (2016) has conducted research on dynamics of spherical gels during swelling and drying, whereas the study has not included the mechanical constraint. Introducing a spherical gel, as shown in Fig. 5.36 with a total initial volume of $V_o = J_o \bar{V}_p$ (see Section 3.9) and the diameter of $\hat{D}_0 = 2(\frac{3V_o}{4\pi})^{1/3}$, here resulting $\hat{D}_0 \approx 2.66$ mm and the gap between the two constraint plates $H = 4$ mm as shown in Fig. 5.28, which are arranged in line with the coordinate axes $(\mathbf{i}, \mathbf{j}, \mathbf{k})$ characterized in (X, Y, Z) in the reference configuration.
As regards absorption-desorption kinetics (see Section 5.1), the duration of the cycle is denoted as τ_d and chosen in accordance with the characteristic time scale of fluid diffusion in the hydrogel, which is $\tau_d = \hat{D}_0^2/\bar{D}_f$, here calculated as ca. $\tau_d = 4$ hours. Rigid body motions of the gel sphere are prevented by fixing the gel's center in all directions. Swelling confinement is introduced by considering two fixed constraining plates, as shown in Fig. 5.36, and the contact is treated by means of an augmented Lagrangian formulation based contact element added both on gel surface and plates.
The computational case study is discretized with a structured mesh of H1 elements with total degrees of freedom of 34295. A representation of the numerical domain is given in Fig. 5.36. If not differently characterized, the reference simulation settings are considered as $\mu_f^{bath} = \bar{\mu}_f$, that is the bath fluid chemical potential equal to the reference fluid one; a concentration $\tilde{C}_c = 1\%$ (w/v) of calcium chloride in the solution.

5.6.1 Constrained chemo-mechanical effect

The local volume change J of the spherical gel under the mechanical constraint (i.e. two plates on top and bottom) is shown in Fig. 5.37 for the intervals of the middle of the absorption phase $t = t_{ab}^{1/2}$ in Fig. 5.37(a), the end of the absorption cycle $t = t_{ab}$ in Fig. 5.37(b), the middle of the desorption phase $t = t_{de}^{1/2}$ in Fig.5.37(c) and at the end of the desorption phase t_{de} in Fig.5.37(d). As reported in Fig. 5.38, the polymer shear modulus G_p, that is normalized in regard to the reference value G_p^0, is presented for the time range at the middle of the absorption phase $t = t_{ab}^{1/2}$ in Fig.5.38(a), at the end of the absorption cycle $t = t_{ab}$ in Fig. 5.38(b), the middle of the desorption phase $t = t_{de}^{1/2}$ in Fig.5.38(c) and at the end of the desorption phase $t = t_{de}$ in Fig. 5.38(d). Hence, it is notable to compare Fig. 5.38a at $t = t_{ab}$ with Fig.5.38d at $t = t_{de}$, which show the effect of the mechanical constraints, resulting in a significant reduction in shear modulus G_p in compare to the sides of the spherical hydrogel after the growth by means of 34% (i.e., ca. G_p = 1.6 G_p^0 versus G_p = 2.6 G_p^0). Further, the pressure-like chemo-mechanical coupling term $\hat{p}$, mechanical quantity directly affecting chemical reactions, is depicted at the middle of the absorption phase at the middle of the absorption phase $t = t_{ab}^{1/2}$ in Fig. 5.39(a), at the end of the absorption cycle $t = t_{ab}$ in Fig.5.39(b), the middle of the desorption phase $t = t_{de}^{1/2}$ in Fig. 5.39(c) and at the end of the desorption phase $t = t_{de}$ in Fig. 5.39(d). This example confirms the robustness of the developed computational framework. The coupled chemo-mechanical formulation is considered here together with a nonlinear unilateral constraint, not showing divergence issues.

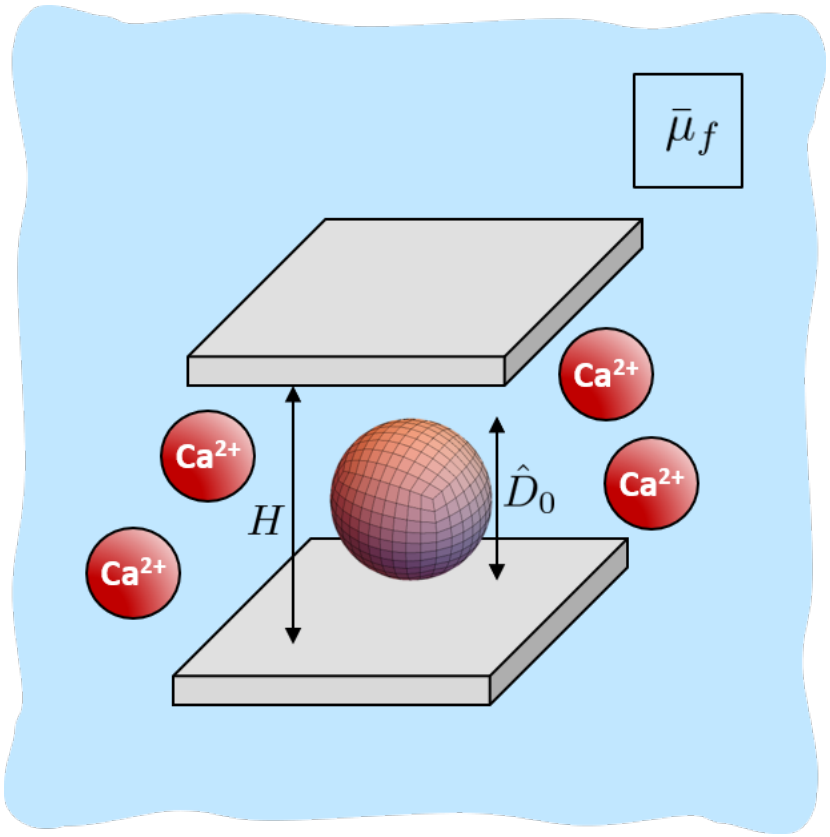

Figure 5.36: Schematic of the computational set-up: the spherical hydrogel specimen with the specified diameter $\hat{D}_0$ discretized with H1 elements, assigned boundary conditions and two constraining plates with the gap distance of H. One absorption-desorption cycle is applied: the hydrogel is immersed in a bath of calcium chloride $CaCl_2$ solution during the absorption procedure undergoing swelling-crosslinking mechanisms, and removed from the bath during the desorption phase. *As-prepared* initial conditions along with the given values in Table 5.1 are adopted.

Accordingly, the developed *in silico* tool can reproduce challenging settings, opening to the analysis of advanced industrial applications.

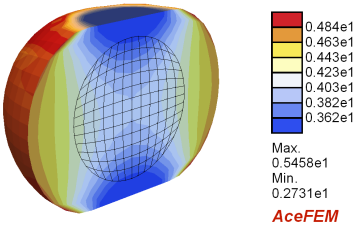

(a) $t = t_{ab}^{1/2}$ at $n_c = 1$

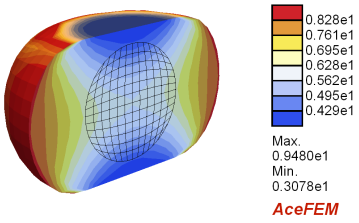

(b) $t = t_{ab}$ at $n_c = 1$

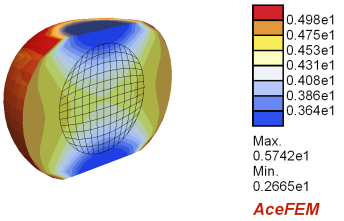

(c) $t = t_{de}^{1/2}$ at $n_c = 1$

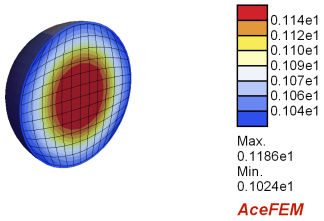

(d) $t = t_{de}$ at $n_c = 1$

Figure 5.37: Change of the Local volume, i.e. $J = \det\mathbf{F}$ of the spherical hydrogel at the middle of the absorption phase (a), at the end of the absorption cycle (b), at the middle of the desorption phase (c) and at the end of the desorption phase (d). Simulation settings associated with the reference example: $\mu_f^{bath} = \bar{\mu}_f$, $\tilde{C}_c = 1\%$ (w/v). The undeformed mesh (from the reference configuration) is shown in each image.

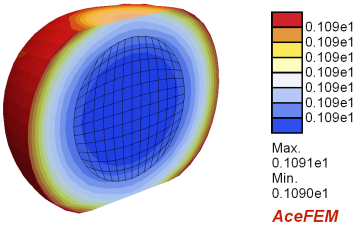

(a) $t = t_{ab}^{1/2}$ at $n_c = 1$

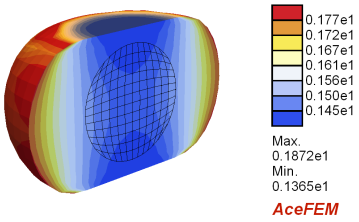

(b) $t = t_{ab}$ at $n_c = 1$

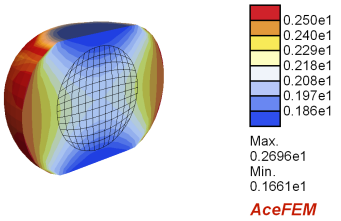

(c) $t = t_{de}^{1/2}$ at $n_c = 1$

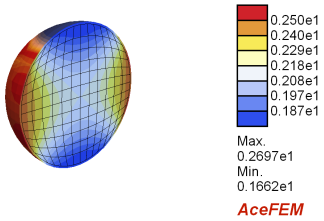

(d) $t = t_{de}$ at $n_c = 1$

Figure 5.38: Polymer shear modulus G_p (normalized in regard to the reference value G_p^0) computed for the spherical hydrogel at the middle of the absorption phase (a), at the end of the absorption cycle (b), at the middle of the desorption phase (c) and at the end of the desorption phase (d). Simulation settings assigned with the reference case study: $\mu_f^{bath} = \bar{\mu}_f$, $\tilde{C}_c = 1\%$ (w/v). The undeformed mesh (from the reference configuration) is demonstrated in each image.

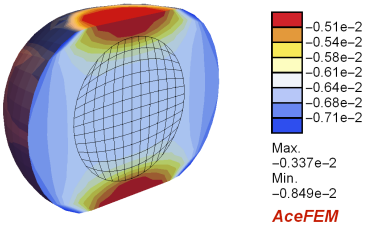

(a) $t = t_{ab}^{1/2}$ at $n_c = 1$

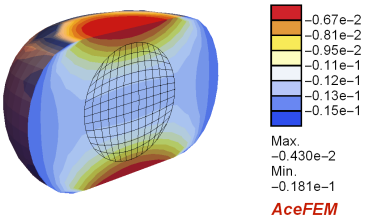

(b) $t = t_{ab}$ at $n_c = 1$

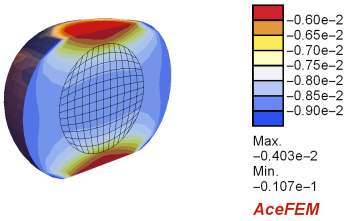

(c) $t = t_{de}^{1/2}$ at $n_c = 1$

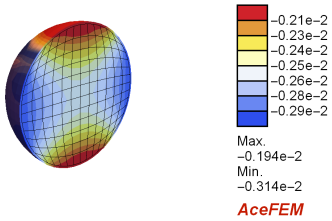

(d) $t = t_{de}$ at $n_c = 1$

Figure 5.39: Mechanical quantity affecting chemical reactions (see Section 3.8): pressure-like coupling term $\hat{p}$ at the middle of the absorption phase (a), at the end of the absorption cycle (b), at the middle of the desorption phase (c) and at the end of the desorption phase (d). Simulation settings correspond to the reference case study: $\mu_f^{bath} = \bar{\mu}_f$, $\tilde{C}_c = 1\%$ (w/v). The undeformed mesh (in the reference configuration) is illustrated in each image.

Chapter 6

Conclusions and outlook

Hydrogels have gained considerable attention in recent years because of their great outlook in a wide range of applications such as bioprinting, drug delivery, and microfluidics (BUCHHOLZ & GRAHAM, 1998; PEPPAS ET AL., 2006; SLAUGHTER ET AL., 2009; BRANNON-PEPPAS & HARLAND, 2012; LI ET AL., 2013). They also maintain a degree of extensibility very similar to natural tissue due to the absorbance of large water content. The hydrogels' capacity to absorb water arises from hydrophilic functional groups connected to the polymeric backbone, while their endurance to dissolution appears from crosslinks between network chains. Several materials, considering natural and synthetic, outfit the definition of hydrogels. Meanwhile, calcium chloride ($CaCl_2$) is one of the most used alginate-based hydrogels' crosslinking agents, which allows for a rapid and straightforward gelation thanks to its release Ca^{2+} cations. Simultaneously, crosslinking by $CaCl_2$ is not a regulated process due to its high solubility in aqueous solutions (COLOSI ET AL., 2016; LEE & MOONEY, 2012; TALEI FRANZESI ET AL., 2006). The crosslinking degree highly depends on alginate and $CaCl_2$ concentration. It is a decisive determinant for controlling hydrogel uniformity and strength: a faster gelation rate is better for cell encapsulation, while a slower gelation rate provides more uniform structures with higher mechanical properties (REZENDE ET AL., 2009; LEE ET AL., 2018; KUO & MA, 2001). Furthermore, crosslinking processes alter the polymeric network's topology, hindering diffusive processes (COLOSI ET AL., 2016; POTTER ET AL., 1994; SALAHSHOOR & RAHBAR, 2014).

A chemo-mechanical model for the swelling behavior of alginate hydrogels in the presence of a crosslinking agent has been developed and presented in this work. The system accounts for shrinking and swelling effects, fluid movements, as well as the reaction kinetics of calcium-induced crosslinking. Crosslinks alter mechanical and diffusive properties in the hydrogel. The model is formulated in large deformations, and it is based on solid thermodynamic arguments, which reveal that internal stresses directly affect the crosslinking kinetics. Two-way coupling between mechanics and chemistry is then obtained.

Values of physical and chemical parameters utilized in this work have been chosen to be in the range of the formation of alginate-Ca^{2+} gels; however, the theoretical equations and the algorithms can be extended to the analysis of other polysaccharide-cation systems.

The model has been implemented in a finite element framework based on a chemo-mechanical monolithic coupling. Besides, convergence studies have been reported to investigate the independency of numerical results on the introduced discretization. Results address

a series of benchmark tests on the absorption-desorption behavior of different hydrogel-based structures immersed in (and removed from) a bath with a calcium chloride solution. In particular, numerical simulations address different test cases of hydrogel specimen in accordance with available experimental observations such as a cubic hydrogel under the free-swelling (Fig. 6.1a) by GÓMEZ (2015), buckling of hydrogel tubes (Fig. 6.1b) by LEE ET AL. (2012), wrinkling of cuboid gels (Fig. 6.1c) by TANAKA ET AL. (1987); GUVENDIREN ET AL. (2010); TOH ET AL. (2015), bending of a polymeric bilayer bar (Fig. 6.2a) by YOON ET AL. (2010), and spherical hydrogel confined swelling (Fig. 6.2b) by BERTRAND ET AL. (2016). The proposed analysis aims to demonstrate the model's capability to elucidate complex coupled mechanisms and the effectiveness of the developed numerical implementation. Among the presented proofs of consistency, it is noteworthy that a schematic representation of the addressed case studies and main evidence is offered in Figs. 6.1 and 6.2. Outcomes are in full agreement with experimental evidence on the absorption-desorption swelling behavior of hydrogels in the presence of a crosslinking agent. Obtained results reproduce the well-known phenomenon that a higher crosslinking degree corresponds to a reduced shrinking (or even syneresis) of hydrogels (e.g. MARTINSEN ET AL., 1989; DRAGET ET AL., 2001; DAVIDOVICH-PINHAS & BIANCO-PELED, 2010; RAMDHAN ET AL., 2019). In particular, experimental results by GÓMEZ (2015) are analogous to the numerical ones presented in Fig. 5.6. To the best of the authors' knowledge, the present works propose for the first time a modeling framework able to provide mechanistic insight on the complex cascade of coupled events leading to these observations.

The proposed study allows defining strategies to conceive highly controlled experimental protocols for identifying the biophysical properties of hydrogel bulk specimens and structures, as well as evaluating the practical impact of coupled mechanisms on the final hydrogel behavior. To reach this goal, an effort has been made to tailor the proposed modeling framework with laboratories set-ups, such as the definition of the *as-prepared* state and the measurement of the gel front propagation rate or the free-swelling capacity. The developed simulation tool can then be effectively employed to identify better crosslinking reaction kinetics parameters accounting for the underlying complex chemo-mechanical coupled effects.

The presented numerical simulations have shown that crosslinking is a phenomenon characterized by a highly heterogeneous distribution of chemo-mechanical quantities within hydrogels. Experimental techniques able to measure such heterogeneities with a sufficient degree of resolution, like the one revealed by the proposed computational framework, do not exist. Therefore, the developed simulation tool can enhance the understanding of the multi-physical behavior of hydrogels' crosslinking processes. Towards this direction, the analysis of the relative importance of different mechanisms could be reached by means of a more consolidated estimate of the value of some model parameters. For instance, only physical ranges can be estimated from available data for the reaction rate K and fluid molar volume Λ (e.g., BRASCHLER ET AL., 2011; DAVIDOVICH-PINHAS & BIANCO-PELED, 2010). In addition, only qualitative evidence is indeed available for the shrinking parameter Γ or the chemo-mechanical modulus κ_α (e.g. DRAGET ET AL., 2001; ANNABI ET AL., 2009). Accordingly, the results of a wide campaign of parametric analyses have been presented in this study. Moreover, the present work might impact the design of optimal crosslinking protocols for hydrogel applications. For instance, the obtained outcomes are crucial when addressing tissue

engineering scaffolds produced employing bioprinting technologies. In fact, heterogeneities in bioprinted scaffold would translate into heterogeneities of the mechano-biological stimulus applied to cells within the gel. The present *in silico* framework can provide a forward step towards the characterization and the optimization of industrial processes.
The proposed study allows defining strategies to conceive experimental procedures for identifying process parameters and evaluating the effective impact of the associated mechanisms on the final hydrogel behaviour. To reach this goal, an effort has been made to tailor the proposed modeling framework with laboratory set-ups, such as the definition of the *as-prepared* state and the measurement of the gel front propagation rate or the free-swelling capacity. The developed simulation tool can be effectively employed to identify better crosslinking reaction kinetics parameters accounting for the underlying complex chemo-mechanical coupled effects.
In perspective, the developed simulation tool might be used to speed-up hydrogel production in laboratories by reducing the need for trial-and-error procedures by means of *in silico* based ones. To this aim, future studies will be performed in collaboration with experimentalists for the better calibration of model parameters, as previously done by authors (HAJIKHANI ET AL., 2019). For instance, the composition of the polymer and the type of fluid (e.g., water or PBS) are known to highly affect hydrogels' behaviour. Additionally, values of model parameter should be adapted to account for these differences remains a major issue. Meanwhile, the employed chemical model can be enriched with a more complex description considering free-alginate diffusion or advanced reaction kinetics. Moreover, the performance of mixed hybrid finite element formulations, featuring an additional independent variable field flux for enforcing local mass conservation, will be investigated (KORELC & WRIGGERS, 2016; YU ET AL., 2019). These mixed formulations have been shown to outperform standard ones in terms of solution convergence robustness and accuracy, especially when swelling problems involve discontinuous interface in permeability, and this characteristic might be advantageous for advanced applications. Besides, an improved EAS (i.e., Enhanced Assumed Strain) brick element can be implemented for preventing locking and hour-glassing in very large deformations for the bending of the beam element (see Sec. 5.5) with incompressibility (KORELC ET AL., 2010). Furthermore, robust mesh-free methods such as the recent Peridynamic Galerkin methods (see e.g. BODE ET AL. (2020b)) can be used for the simulation of processes which are subject to very large deformations. Moreover, the current studied chemical model can be enriched to a more complex model considering free-alginate diffusion (here neglected) or advanced reaction kinetics. Further, the multiphysics theory can be elaborated by including the significant thermal and electrostatic effects. Finally, hydrogels can be composed of mixtures of different polymers such as agarose/collagen along with sodium alginate as bioink for bioprinting (GOPINATHAN & NOH, 2018), alginate-collagen fibril gel composite (Alg/Col gel), alginate-hyaluronic acid-collagen composite hydrogels that are favorable for the culture of chondrocytes (MAHAPATRA ET AL., 2016; JIN & KIM, 2018) and alginate–marine collagen–agarose composite hydrogels for biomimetic 3D cell spheroid formation (SHIN ET AL., 2016). Such mixture of polymers would require a special treatment of the associated poroelastic and crosslinking effects, thus calling for model refinements.

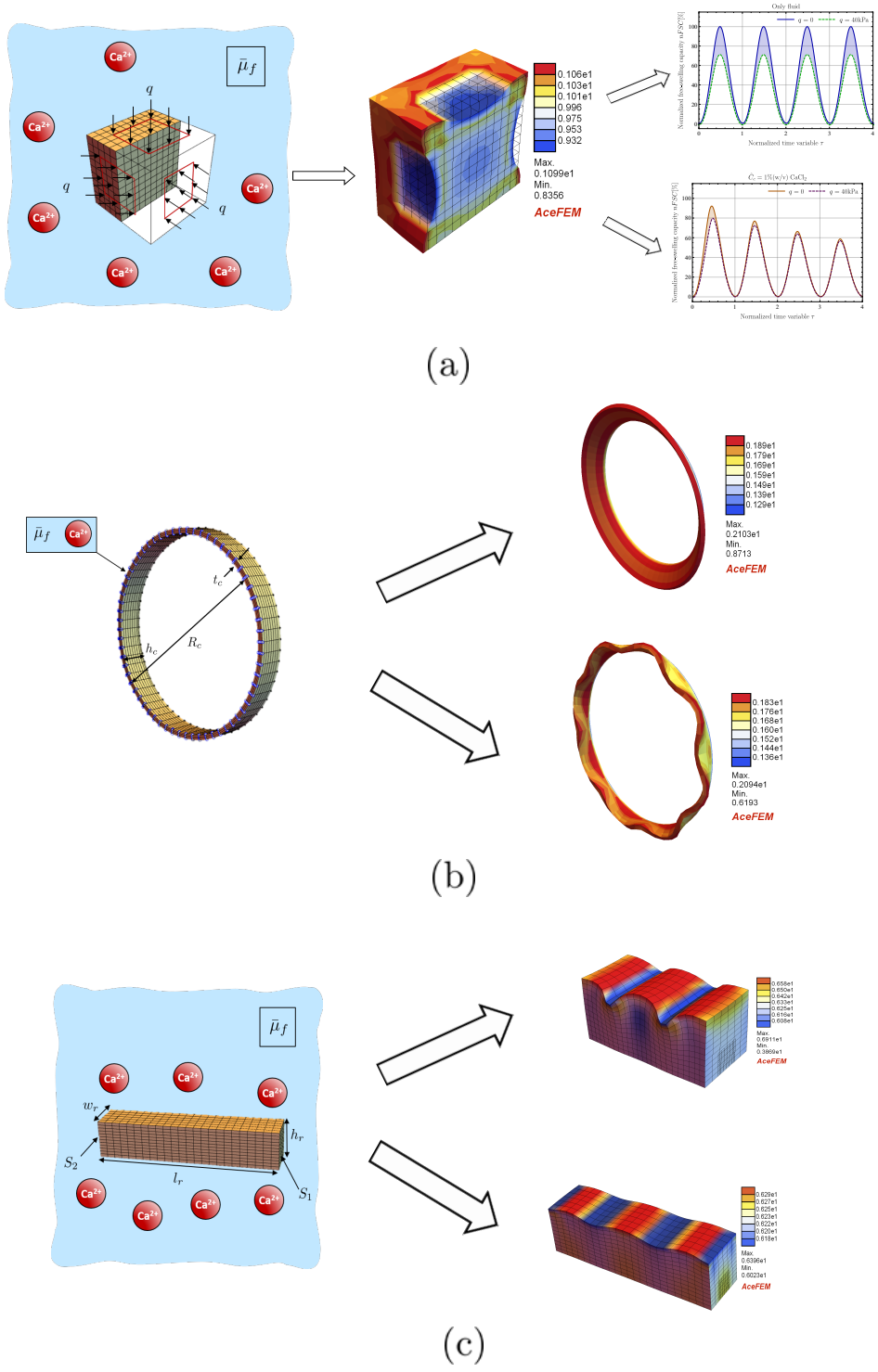

Figure 6.1: Numerical test cases: Free-swelling of cubic hydrogel (a); Buckling of hydrogel tubes (b); Wrinkling of cuboid (c).

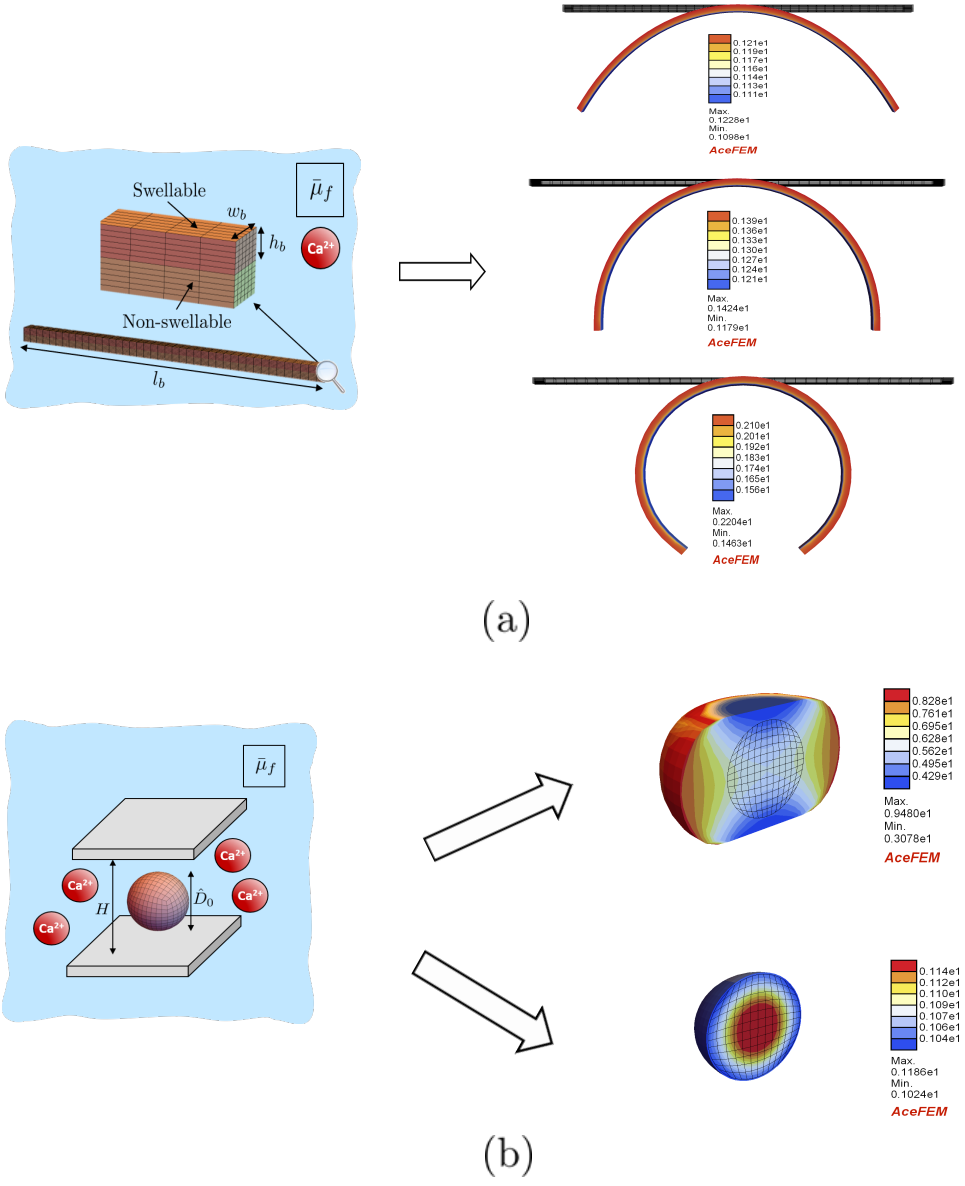

Figure 6.2: Numerical test cases: Bending of a polymeric bilayer bar (a); Spherical gel confined swelling (b).

Bibliography

ABIDIAN M.R. & MARTIN D.C. Multifunctional nanobiomaterials for neural interfaces. *Advanced Functional Materials*, 19 (2009) (4): 573–585.

AGARWAL T., NARAYANA S.G.H., PAL K., PRAMANIK K. ET AL. Calcium alginate-carboxymethyl cellulose beads for colon-targeted drug delivery. *International journal of biological macromolecules*, 75 (2015): 409–417.

AMSDEN B. Solute diffusion within hydrogels. mechanisms and models. *Macromolecules*, 31 (1998) (23): 8382–8395.

ANAND L. A large deformation poroplasticity theory for microporous polymeric materials. *Journal of the Mechanics and Physics of Solids*, 98 (2017): 126–155.

ANNABI N., MITHIEUX S.M., WEISS A.S. & DEHGHANI F. The fabrication of elastin-based hydrogels using high pressure co2. *Biomaterials*, 30 (2009) (1): 1 – 7.

ANTHONSEN M.W., VÅRUM K.M. & SMIDSRØD O. Solution properties of chitosans: conformation and chain stiffness of chitosans with different degrees of n-acetylation. *Carbohydrate Polymers*, 22 (1993) (3): 193–201.

ATALA A. & YOO J.J. *Essentials of 3D biofabrication and translation*. Academic Press, 2015.

AZNAR J.M.G., VALERO C., BORAU C. & GARIJO N. Computational mechano-chemo-biology: a tool for the design of tissue scaffolds. *Biomanufacturing Reviews*, 1 (2016) (1): 2.

BAEK S. & PENCE T.J. Inhomogeneous deformation of elastomer gels in equilibrium under saturated and unsaturated conditions. *Journal of the Mechanics and Physics of Solids*, 59 (2011) (3): 561–582.

BEEBE D.J., MOORE J.S., BAUER J.M., YU Q. ET AL. Functional hydrogel structures for autonomous flow control inside microfluidic channels. *Nature*, 404 (2000) (6778): 588–590.

BELLANDER M., STENBERG B. & PERSSON S. Crosslinking of polybutadiene rubber without any vulcanization agent. *Polymer Engineering & Science*, 38 (1998) (8): 1254–1260.

BELLICH B., BORGOGNA M., COK M. & CESÀRO A. Release properties of hydrogels: water evaporation from alginate gel beads. *Food biophysics*, 6 (2011) (2): 259–266.

BERTRAND T., PEIXINHO J., MUKHOPADHYAY S. & MACMINN C.W. Dynamics of swelling and drying in a spherical gel. *Physical Review Applied*, 6 (2016) (6): 064 010.

BIOT M.A. General theory of three-dimensional consolidation. *Journal of applied physics*, 12 (1941) (2): 155–164.

BODE T., WEISSENFELS C. & WRIGGERS P. Mixed peridynamic formulations for compressible and incompressible finite deformations. *Computational Mechanics*, (2020b): 1–12.

BOUKLAS N. & HUANG R. Swelling kinetics of polymer gels: comparison of linear and nonlinear theories. *Soft Matter*, 8 (2012) (31): 8194–8203.

BOYCE M.C. & ARRUDA E.M. Swelling and mechanical stretching of elastomeric materials. *Mathematics and Mechanics of Solids*, 6 (2001) (6): 641–659.

BRACCINI I. & PÉREZ S. Molecular basis of ca2+-induced gelation in alginates and pectins: the egg-box model revisited. *Biomacromolecules*, 2 (2001) (4): 1089–1096.

BRANNON-PEPPAS L. & HARLAND R.S. *Absorbent polymer technology*. Elsevier, 2012.

BRASCHLER T., VALERO A., COLELLA L., PATAKY K. ET AL. Link between alginate reaction front propagation and general reaction diffusion theory. *Analytical chemistry*, 83 (2011) (6): 2234–2242.

BUCHHOLZ F.L. & GRAHAM A.T. Modern superabsorbent polymer technology. *John Wiley & Sons, Inc, 605 Third Ave, New York, NY 10016, USA, 1998. 279*, (1998).

CACOPARDO L., GUAZZELLI N., NOSSA R., MATTEI G. ET AL. Engineering hydrogel viscoelasticity. *Journal of the Mechanical Behavior of Biomedical Materials*, 89 (2019): 162 – 167.

CARLIER A., SKVORTSOV G.A., HAFEZI F., FERRARIS E. ET AL. Computational model-informed design and bioprinting of cell-patterned constructs for bone tissue engineering. *Biofabrication*, 8 (2016) (2): 025 009.

CHANG C., DUAN B., CAI J. & ZHANG L. Superabsorbent hydrogels based on cellulose for smart swelling and controllable delivery. *European polymer journal*, 46 (2010) (1): 92–100.

CHESTER S.A. & ANAND L. A thermo-mechanically coupled theory for fluid permeation in elastomeric materials: application to thermally responsive gels. *Journal of the Mechanics and Physics of Solids*, 59 (2011) (10): 1978–2006.

CHESTER S.A., DI LEO C.V. & ANAND L. A finite element implementation of a coupled diffusion-deformation theory for elastomeric gels. *International Journal of Solids and Structures*, 52 (2015): 1–18.

COLOSI C., SHIN S.R., MANOHARAN V., MASSA S. ET AL. Microfluidic bioprinting of heterogeneous 3d tissue constructs using low-viscosity bioink. *Advanced materials*, 28 (2016) (4): 677–684.

COSTANTINI M., IDASZEK J., SZÖKE K., JAROSZEWICZ J. ET AL. 3d bioprinting of bm-mscs-loaded ecm biomimetic hydrogels for in vitro neocartilage formation. *Biofabrication*, 8 (2016) (3): 035 002.

CYRON C. & HUMPHREY J. Growth and remodeling of load-bearing biological soft tissues. *Meccanica*, 52 (2017) (3): 645–664.

DABABNEH A.B. & OZBOLAT I.T. Bioprinting technology: a current state-of-the-art review. *Journal of Manufacturing Science and Engineering*, 136 (2014) (6).

DASHEVSKY A. Protein loss by the microencapsulation of an enzyme (lactase) in alginate beads. *International journal of Pharmaceutics*, 161 (1998) (1): 1–5.

DAVIDOVICH-PINHAS M. & BIANCO-PELED H. A quantitative analysis of alginate swelling. *Carbohydrate Polymers*, 79 (2010) (4): 1020–1027.

DE QUEIROZ A.A., PASSOS E.D., DE BRITO ALVES S., SILVA G.S. ET AL. Alginate–poly (vinyl alcohol) core–shell microspheres for lipase immobilization. *Journal of Applied Polymer Science*, 102 (2006) (2): 1553–1560.

DOI M. Gel dynamics. *Journal of the Physical Society of Japan*, 78 (2009) (5): 052 001.

DOLBOW J., FRIED E. & JI H. Chemically induced swelling of hydrogels. *Journal of the Mechanics and Physics of Solids*, 52 (2004) (1): 51–84.

DOUMECHE B., KÜPPERS M., STAPF S., BLÜMICH B. ET AL. New approaches to the visualization, quantification and explanation of acid-induced water loss from ca-alginate hydrogel beads. *Journal of microencapsulation*, 21 (2004) (5): 565–573.

DRAGET K.I., GÅSERØD O., AUNE I., ANDERSEN P.O. ET AL. Effects of molecular weight and elastic segment flexibility on syneresis in ca-alginate gels. *Food Hydrocolloids*, 15 (2001) (4-6): 485–490.

DROZDOV A. & CHRISTIANSEN J.D. Constitutive equations in finite elasticity of swollen elastomers. *International Journal of Solids and Structures*, 50 (2013) (9): 1494–1504.

DRURY J.L., DENNIS R.G. & MOONEY D.J. The tensile properties of alginate hydrogels. *Biomaterials*, 25 (2004) (16): 3187–3199.

DRURY J.L. & MOONEY D.J. Hydrogels for tissue engineering: scaffold design variables and applications. *Biomaterials*, 24 (2003) (24): 4337–4351.

DUAN B., HOCKADAY L.A., KANG K.H. & BUTCHER J.T. 3d bioprinting of heterogeneous aortic valve conduits with alginate/gelatin hydrogels. *Journal of biomedical materials research Part A*, 101 (2013) (5): 1255–1264.

DUARTE CAMPOS D.F., ROHDE M., ROSS M., ANVARI P. ET AL. Corneal bioprinting utilizing collagen-based bioinks and primary human keratocytes. *Journal of Biomedical Materials Research Part A*, 107 (2019) (9): 1945–1953.

DUDA F.P., SOUZA A.C. & FRIED E. A theory for species migration in a finitely strained solid with application to polymer network swelling. *Journal of the Mechanics and Physics of Solids*, 58 (2010) (4): 515–529.

DUEZ J.M., MESTDAGH M., DEMEURE R., GOUDEMANT J.F. ET AL. Nmr studies of calcium-induced alginate gelation. part i—mri tests of gelation models. *Magnetic Resonance in Chemistry*, 38 (2000) (5): 324–330.

FLORY P.J. Thermodynamics of high polymer solutions. *The Journal of chemical physics*, 10 (1942) (1): 51–61.

FLORY P.J. & ERMAN B. Theory of elasticity of polymer networks. 3. *Macromolecules*, 15 (1982) (3): 800–806.

FLORY P.J. & REHNER JR J. Statistical mechanics of cross-linked polymer networks i. rubberlike elasticity. *The journal of chemical physics*, 11 (1943) (11): 512–520.

GALAEV I.Y. & MATTIASSON B. 'smart'polymers and what they could do in biotechnology and medicine. *Trends in biotechnology*, 17 (1999) (8): 335–340.

GIBBS J.W. On the equilibrium of heterogeneous substances. (1978).

GIRIDHAR R.S. & AKANKSHA S.P. Swelling behavior of calcium–ions crosslinked bipolymeric sodium alginate–lignosulphonic acid blends. *International Journal of Polymeric Materials*, 60 (2011) (14): 1123–1129.

GOMBOTZ W.R. & WEE S. Protein release from alginate matrices. *Advanced drug delivery reviews*, 31 (1998) (3): 267–285.

GOMES M., SALGADO A. & REIS R. 'polymer based systems on tissue engineering, replacement and regeneration. *Kluwer, Dordrecht, The Netherlands*, (2002): 221.

GÓMEZ J.S. Characterization and effects of cross-linked potassium polyacrylate as soil amendment. *University of Seville, Seville, Spain*, (2015).

GOPINATHAN J. & NOH I. Recent trends in bioinks for 3d printing. *Biomaterials research*, 22 (2018) (1): 11.

GUNGOR-OZKERIM P.S., INCI I., ZHANG Y.S., KHADEMHOSSEINI A. ET AL. Bioinks for 3d bioprinting: an overview. *Biomaterials science*, 6 (2018) (5): 915–946.

GUPTA M., PANDE A., RAO R.S. & TRIPATHI A. Design pattern detection by normalized cross correlation. In *2010 International Conference on Methods and Models in Computer Science (ICM2CS-2010)*, pages 81–84. IEEE, 2010.

GURTIN M.E., FRIED E. & ANAND L. *The mechanics and thermodynamics of continua*. Cambridge University Press, 2010.

GUVENDIREN M., BURDICK J.A. & YANG S. Kinetic study of swelling-induced surface pattern formation and ordering in hydrogel films with depth-wise crosslinking gradient. *Soft Matter*, 6 (2010) (9): 2044–2049.

HAJIKHANI A., SCOCOZZA F., CONTI M., MARINO M. ET AL. Experimental characterization and computational modeling of hydrogel cross-linking for bioprinting applications. *The International journal of artificial organs*, 42 (2019) (10): 548–557.

HIMPEL G., KUHL E., MENZEL A. & STEINMANN P. Computational modelling of isotropic multiplicative growth. *Comp Mod Eng Sci*, 8 (2005): 119–134.

HOLMES D.P., ROCHÉ M., SINHA T. & STONE H.A. Bending and twisting of soft materials by non-homogenous swelling. *Soft Matter*, 7 (2011) (11): 5188–5193.

HOLZAPFEL A.G. Nonlinear solid mechanics ii. (2000).

HONG W., LIU Z. & SUO Z. Inhomogeneous swelling of a gel in equilibrium with a solvent and mechanical load. *International Journal of Solids and Structures*, 46 (2009) (17): 3282–3289.

HONG W., ZHAO X., ZHOU J. & SUO Z. A theory of coupled diffusion and large deformation in polymeric gels. *Journal of the Mechanics and Physics of Solids*, 56 (2008) (5): 1779–1793.

HUDOBIVNIK B. *Automatic differentiation based solution of strongly coupled problems in engineering*. Ph.D. thesis, University of Ljubljana, Faculty of Civil and Geodetic Engineering (2016).

HUGGINS M.L. Some properties of solutions of long-chain compounds. *The Journal of Physical Chemistry*, 46 (1942) (1): 151–158.

JAGUR-GRODZINSKI J. Polymers for tissue engineering, medical devices, and regenerative medicine. concise general review of recent studies. *Polymers for advanced technologies*, 17 (2006) (6): 395–418.

JAMES A.L., PARÉ P.D., HOGG J.C. ET AL. The mechanics of airway narrowing in asthma. *Am Rev Respir Dis*, 139 (1989) (1): 242–246.

JEONG B., BAE Y.H., LEE D.S. & KIM S.W. Biodegradable block copolymers as injectable drug-delivery systems. *Nature*, 388 (1997) (6645): 860–862.

JIA J., RICHARDS D.J., POLLARD S., TAN Y. ET AL. Engineering alginate as bioink for bioprinting. *Acta biomaterialia*, 10 (2014) (10): 4323–4331.

JIN G.Z. & KIM H.W. Efficacy of collagen and alginate hydrogels for the prevention of rat chondrocyte dedifferentiation. *Journal of tissue engineering*, 9 (2018): 2041731418802 438.

KHALIL S. & SUN W. Bioprinting endothelial cells with alginate for 3d tissue constructs. *Journal of biomechanical engineering*, 131 (2009) (11).

KONG H.J., ALSBERG E., KAIGLER D., LEE K.Y. ET AL. Controlling degradation of hydrogels via the size of crosslinked junctions. *Advanced Materials*, 16 (2004) (21): 1917–1921.

KORELC J., ŠOLINC U. & WRIGGERS P. An improved eas brick element for finite deformation. *Computational mechanics*, 46 (2010) (4): 641–659.

KORELC J. & WRIGGERS P. *Automation ofFinite Element Methods*. Springer, 2016.

KUO C.K. & MA P.X. Ionically crosslinked alginate hydrogels as scaffolds for tissue engineering: Part 1. structure, gelation rate and mechanical properties. *Biomaterials*, 22 (2001) (6): 511–521.

LAROBINA D. & CIPELLETTI L. Hierarchical cross-linking in physical alginate gels: a rheological and dynamic light scattering investigation. *Soft Matter*, 9 (2013) (42): 10 005–10 015.

LEE B.B., BHANDARI B.R. & HOWES T. Gelation of an alginate film via spraying of calcium chloride droplets. *Chemical Engineering Science*, 183 (2018): 1–12.

LEE D.Y., LEE H., KIM Y., YOO S.Y. ET AL. Phage as versatile nanoink for printing 3-d cell-laden scaffolds. *Acta biomaterialia*, 29 (2016): 112–124.

LEE H., ZHANG J., JIANG H. & FANG N.X. Prescribed pattern transformation in swelling gel tubes by elastic instability. *Physical review letters*, 108 (2012) (21): 214 304.

LEE H.J., KIM Y.B., AHN S.H., LEE J.S. ET AL. A new approach for fabricating collagen/ecm-based bioinks using preosteoblasts and human adipose stem cells. *Advanced healthcare materials*, 4 (2015) (9): 1359–1368.

LEE J.M. & YEONG W.Y. Design and printing strategies in 3d bioprinting of cell-hydrogels: A review. *Advanced healthcare materials*, 5 (2016) (22): 2856–2865.

LEE K.Y., BOUHADIR K.H. & MOONEY D.J. Degradation behavior of covalently cross-linked poly (aldehyde guluronate) hydrogels. *Macromolecules*, 33 (2000a) (1): 97–101.

LEE K.Y. & MOONEY D.J. Alginate: properties and biomedical applications. *Progress in polymer science*, 37 (2012) (1): 106–126.

LEE K.Y., ROWLEY J.A., EISELT P., MOY E.M. ET AL. Controlling mechanical and swelling properties of alginate hydrogels independently by cross-linker type and cross-linking density. *Macromolecules*, 33 (2000b) (11): 4291–4294.

LEE W., LEE V., POLIO S., KEEGAN P. ET AL. On-demand three-dimensional freeform fabrication of multi-layered hydrogel scaffold with fluidic channels. *Biotechnology and bioengineering*, 105 (2010) (6): 1178–1186.

LEROUX M.A., GUILAK F. & SETTON L.A. Compressive and shear properties of alginate gel: effects of sodium ions and alginate concentration. *Journal of Biomedical Materials Research: An Official Journal of The Society for Biomaterials, The Japanese Society for Biomaterials, and The Australian Society for Biomaterials and the Korean Society for Biomaterials*, 47 (1999) (1): 46–53.

LI Y., HUANG G., ZHANG X., LI B. ET AL. Magnetic hydrogels and their potential biomedical applications. *Advanced Functional Materials*, 23 (2013) (6): 660–672.

LOEFFEL K. & ANAND L. A chemo-thermo-mechanically coupled theory for elastic–viscoplastic deformation, diffusion, and volumetric swelling due to a chemical reaction. *International Journal of Plasticity*, 27 (2011) (9): 1409–1431.

LOZANO-VAZQUEZ G., LOBATO-CALLEROS C., ESCALONA-BUENDIA H., CHAVEZ G. ET AL. Effect of the weight ratio of alginate-modified tapioca starch on the physicochemical properties and release kinetics of chlorogenic acid containing beads. *Food Hydrocolloids*, 48 (2015): 301–311.

LUCANTONIO A., NARDINOCCHI P. & TERESI L. Transient analysis of swelling-induced large deformations in polymer gels. *Journal of the Mechanics and Physics of Solids*, 61 (2013) (1): 205–218.

MA X., LOZANO-OJALVO D., CHEN H., LOPEZ-FANDIÑO R. ET AL. Effect of high pressure-assisted crosslinking of ovalbumin and egg white by transglutaminase on their potential allergenicity. *Innovative Food Science & Emerging Technologies*, 29 (2015): 143 – 150.

MAGNENET V., SCHIAVI-TRITZ J., HUSELSTEIN C. & RAHOUADJ R. Constitutive equations for ca2+ -alginate gels. *Journal of the Mechanical Behavior of Biomedical Materials*, 5 (2012) (1): 90 – 98.

MAHAPATRA C., JIN G.Z. & KIM H.W. Alginate-hyaluronic acid-collagen composite hydrogel favorable for the culture of chondrocytes and their phenotype maintenance. *Tissue engineering and regenerative medicine*, 13 (2016) (5): 538–546.

MAI T.H.A. ET AL. Biochemical studies on the immobilized lactase in the combined alginate–carboxymethyl cellulose gel. *Biochemical engineering journal*, 74 (2013): 81–87.

MAITRA J. & SHUKLA V.K. Cross-linking in hydrogels - a review. *American Journal of Polymer Science*, 4 (2014) (2): 25–31.

MARIJNISSEN W.J., VAN OSCH G.J., AIGNER J., VAN DER VEEN S.W. ET AL. Alginate as a chondrocyte-delivery substance in combination with a non-woven scaffold for cartilage tissue engineering. *Biomaterials*, 23 (2002) (6): 1511–1517.

MARTINSEN A., SKJÅK-BRÆK G. & SMIDSRØD O. Alginate as immobilization material: I. correlation between chemical and physical properties of alginate gel beads. *Biotechnology and bioengineering*, 33 (1989) (1): 79–89.

MIKKELSEN A. & ELGSAETER A. Density distribution of calcium-induced alginate gels. a numerical study. *Biopolymers: Original Research on Biomolecules*, 36 (1995) (1): 17–41.

MITCHELL J. & BLANSHARD J. Viscoelastic behaviour of alginate gels. *Rheologica Acta*, 13 (1974) (2): 180–184.

MITCHELL J. & BLANSHARD J. Rheological properties of pectate gels. *Journal of Texture Studies*, 7 (1976) (3): 341–351.

MØRCH Y.A., QI M., GUNDERSEN P.O.M., FORMO K. ET AL. Binding and leakage of barium in alginate microbeads. *Journal of Biomedical Materials Research Part A*, 100 (2012) (11): 2939–2947.

MORESI M. & BRUNO M. Characterisation of alginate gels using quasi-static and dynamic methods. *Journal of food engineering*, 82 (2007) (3): 298–309.

MORRIS E.R., REES D.A., THOM D. & BOYD J. Chiroptical and stoichiometric evidence of a specific, primary dimerisation process in alginate gelation. *Carbohydrate research*, 66 (1978) (1): 145–154.

MURPHY S.V. & ATALA A. 3d bioprinting of tissues and organs. *Nature biotechnology*, 32 (2014) (8): 773–785.

NAGHIEH S., KARAMOOZ-RAVARI M.R., SARKER M., KARKI E. ET AL. Influence of crosslinking on the mechanical behavior of 3d printed alginate scaffolds: Experimental and numerical approaches. *Journal of the Mechanical Behavior of Biomedical Materials*, 80 (2018a): 111 – 118.

NAGHIEH S., KARAMOOZ-RAVARI M.R., SARKER M., KARKI E. ET AL. Influence of crosslinking on the mechanical behavior of 3d printed alginate scaffolds: Experimental and numerical approaches. *Journal of the mechanical behavior of biomedical materials*, 80 (2018b): 111–118.

NUNAMAKER E.A., PURCELL E.K. & KIPKE D.R. In vivo stability and biocompatibility of implanted calcium alginate disks. *Journal of Biomedical Materials Research Part A: An Official Journal of The Society for Biomaterials, The Japanese Society for Biomaterials, and The Australian Society for Biomaterials and the Korean Society for Biomaterials*, 83 (2007) (4): 1128–1137.

OERTHER S., LE GALL H., PAYAN E., LAPICQUE F. ET AL. Hyaluronate-alginate gel as a novel biomaterial: Mechanical properties and formation mechanism. *Biotechnology and bioengineering*, 63 (1999) (2): 206–215.

OTTERLEI M., ØSTGAARD K., SKJÅK-BRÆK G., SMIDSRØD O. ET AL. Induction of cytokine production from human monocytes stimulated with alginate. *Journal of Immunotherapy*, 10 (1991) (4): 286–291.

PAL K., BANTHIA A. & MAJUMDAR D. Polymeric hydrogels: characterization and biomedical applications. *Designed monomers and polymers*, 12 (2009) (3): 197–220.

PANDEY A. & HOLMES D.P. Swelling-induced deformations: a materials-defined transition from macroscale to microscale deformations. *Soft Matter*, 9 (2013) (23): 5524–5528.

PEPPAS N.A., HILT J.Z., KHADEMHOSSEINI A. & LANGER R. Hydrogels in biology and medicine: from molecular principles to bionanotechnology. *Advanced materials*, 18 (2006) (11): 1345–1360.

POTTER K., BALCOM B.J., CARPENTER T.A. & HALL L.D. The gelation of sodium alginate with calcium ions studied by magnetic resonance imaging (mri). *Carbohydrate research*, 257 (1994) (1): 117–126.

PUGUAN J.M.C., YU X. & KIM H. Characterization of structure, physico-chemical properties and diffusion behavior of ca-alginate gel beads prepared by different gelation methods. *Journal of colloid and interface science*, 432 (2014): 109–116.

QIU Y. & PARK K. Environment-sensitive hydrogels for drug delivery. *Advanced drug delivery reviews*, 53 (2001) (3): 321–339.

RAMDHAN T., CHING S.H., PRAKASH S. & BHANDARI B. Time dependent gelling properties of cuboid alginate gels made by external gelation method: Effects of alginate-cacl2 solution ratios and ph. *Food Hydrocolloids*, 90 (2019): 232–240.

REDINGTON A.E. & HOWARTH P.H. Airway wall remodelling in asthma. *Thorax*, 52 (1997) (4): 310.

REES D. & SAMUEL J. The structure of alginic acid. part vi. minor features and structural variations. *Journal of the Chemical Society C: Organic*, (1967): 2295–2298.

REZENDE R.A., BÁRTOLO P.J., MENDES A. & FILHO R.M. Rheological behavior of alginate solutions for biomanufacturing. *Journal of applied polymer science*, 113 (2009) (6): 3866–3871.

ROWLEY J.A. & MOONEY D.J. Alginate type and rgd density control myoblast phenotype. *Journal of Biomedical Materials Research: An Official Journal of The Society for Biomaterials, The Japanese Society for Biomaterials, and The Australian Society for Biomaterials and the Korean Society for Biomaterials*, 60 (2002) (2): 217–223.

SAARAI A., KASPARKOVA V., SEDLACEK T. & SÁHA P. On the development and characterisation of crosslinked sodium alginate/gelatine hydrogels. *Journal of the mechanical behavior of biomedical materials*, 18 (2013): 152–166.

SAIN T., LOEFFEL K. & CHESTER S. A thermo–chemo–mechanically coupled constitutive model for curing of glassy polymers. *Journal of the Mechanics and Physics of Solids*, 116 (2018): 267–289.

SALAHSHOOR H. & RAHBAR N. Multi-scale mechanical and transport properties of a hydrogel. *journal of the mechanical behavior of biomedical materials*, 37 (2014): 299–306.

SCHUSTER E., ECKARDT J., HERMANSSON A.M., LARSSON A. ET AL. Microstructural, mechanical and mass transport properties of isotropic and capillary alginate gels. *Soft matter*, 10 (2014) (2): 357–366.

SECCHI E., ROVERSI T., BUZZACCARO S., PIAZZA L. ET AL. Biopolymer gels with "physical" cross-links: gelation kinetics, aging, heterogeneous dynamics, and macroscopic mechanical properties. *Soft Matter*, 9 (2013) (15): 3931–3944.

SHIN S., IKRAM M., SUBHAN F., KANG H.Y. ET AL. Alginate–marine collagen–agarose composite hydrogels as matrices for biomimetic 3d cell spheroid formation. *RSC advances*, 6 (2016) (52): 46 952–46 965.

SKJÁK-BRÆK G., SMIDSRØD O. & LARSEN B. Tailoring of alginates by enzymatic modification in vitro. *International Journal of Biological Macromolecules*, 8 (1986) (6): 330–336.

SLAUGHTER B.V., KHURSHID S.S., FISHER O.Z., KHADEMHOSSEINI A. ET AL. Hydrogels in regenerative medicine. *Advanced materials*, 21 (2009) (32-33): 3307–3329.

SMIDSROD O. Properties of poly (1, 4-hexuronates) in gel state. 2. comparison of gels of different chemical composition. *Acta Chemica Scandinavica*, 26 (1972) (1): 79.

SMIDSRØD O. & HAUG A. Dependence upon uronic acid composition of some ion-exchange properties of alginates. *Acta Chem. Scand*, 22 (1968) (6): 1989–1997.

SMIDSRØD O. & HAUG A. Estimation of the relative stiffness of the molecular chain in polyelectrolytes from measurements of viscosity at different ionic strengths. *Biopolymers: Original Research on Biomolecules*, 10 (1971) (7): 1213–1227.

SMIDSROD O., HAUG A. & WHITTINGTON S.G. The molecular basis for some physical properties of polyuronides. *Acta chem. scand*, 26 (1972) (6).

SOLEIMANI M. Finite strain visco-elastic growth driven by nutrient diffusion: theory, fem implementation and an application to the biofilm growth. *Computational Mechanics*, 64 (2019) (5): 1289–1301.

STOKKE B.T., DRAGET K.I., SMIDSRØD O., YUGUCHI Y. ET AL. Small-angle x-ray scattering and rheological characterization of alginate gels. 1. ca- alginate gels. *Macromolecules*, 33 (2000) (5): 1853–1863.

SUCIU A.N., IWATSUBO T., MATSUDA M. & NISHINO T. A study upon durability of the artificial knee joint with pva hydrogel cartilage. *JSME International Journal Series C Mechanical Systems, Machine Elements and Manufacturing*, 47 (2004) (1): 199–208.

TALEI FRANZESI G., NI B., LING Y. & KHADEMHOSSEINI A. A controlled-release strategy for the generation of cross-linked hydrogel microstructures. *Journal of the American Chemical Society*, 128 (2006) (47): 15 064–15 065.

TANAKA T. & FILLMORE D.J. Kinetics of swelling of gels. *The Journal of Chemical Physics*, 70 (1979) (3): 1214–1218.

TANAKA T., SUN S.T., HIROKAWA Y., KATAYAMA S. ET AL. Mechanical instability of gels at the phase transition. *Nature*, 325 (1987) (6107): 796–798.

THU B., GÅSERØD O., PAUS D., MIKKELSEN A. ET AL. Inhomogeneous alginate gel spheres: An assessment of the polymer gradients by synchrotron radiation-induced x-ray emission, magnetic resonance microimaging, and mathematical modeling. *Biopolymers: Original Research on Biomolecules*, 53 (2000) (1): 60–71.

TOH W., DING Z., YONG NG T. & LIU Z. Wrinkling of a polymeric gel during transient swelling. *Journal of Applied Mechanics*, 82 (2015) (6).

TOKAREV I., GOPISHETTY V., ZHOU J., PITA M. ET AL. Stimuli-responsive hydrogel membranes coupled with biocatalytic processes. *ACS applied materials & interfaces*, 1 (2009) (3): 532–536.

TONPHENG B. & ANDERSSON O. Crosslinking, thermal properties and relaxation behaviour of polyisoprene under high-pressure. *European Polymer Journal*, 44 (2008) (9): 2865 – 2873.

TOOMEY R., FREIDANK D. & RÜHE J. Swelling behavior of thin, surface-attached polymer networks. *Macromolecules*, 37 (2004) (3): 882–887.

VELINGS N.M. & MESTDAGH M.M. Physico-chemical properties of alginate gel beads. *Polymer Gels and Networks*, 3 (1995) (3): 311–330.

VOO W.P., OOI C.W., ISLAM A., TEY B.T. ET AL. Calcium alginate hydrogel beads with high stiffness and extended dissolution behaviour. *European Polymer Journal*, 75 (2016): 343–353.

WANG J. Tracer-diffusions in liquids. iv. selfdiffusion of calcium ion and chloride ion in aqueous calcium chloride solutions-corrections. *Journal of the American Chemical Society*, 75 (1953) (24): 6361–6361.

WANG Z., ABDULLA R., PARKER B., SAMANIPOUR R. ET AL. A simple and high-resolution stereolithography-based 3d bioprinting system using visible light crosslinkable bioinks. *Biofabrication*, 7 (2015) (4): 045 009.

WANG Z.Y., ZHANG Q.Z., KONNO M. & SAITO S. Sol–gel transition of alginate solution by the addition of various divalent cations: 13c-nmr spectroscopic study. *Biopolymers: Original Research on Biomolecules*, 33 (1993) (4): 703–711.

WILLIAMS D., THAYER P., MARTINEZ H., GATENHOLM E. ET AL. A perspective on the physical, mechanical and biological specifications of bioinks and the development of functional tissues in 3d bioprinting. *Bioprinting*, 9 (2018): 19–36.

WRIGGERS P. *Nonlinear finite element methods*. Springer Science & Business Media, 2008.

WU Y., JOSEPH S. & ALURU N.R. Effect of cross-linking on the diffusion of water, ions, and small molecules in hydrogels. *The Journal of Physical Chemistry B*, 113 (2009) (11): 3512–3520.

WÜST S., MÜLLER R. & HOFMANN S. Controlled positioning of cells in biomaterials—approaches towards 3d tissue printing. *Journal of functional biomaterials*, 2 (2011) (3): 119–154.

YAN J., HUANG Y. & CHRISEY D.B. Laser-assisted printing of alginate long tubes and annular constructs. *Biofabrication*, 5 (2012) (1): 015 002.

YAZICI I. & OKAY O. Spatial inhomogeneity in poly (acrylic acid) hydrogels. *Polymer*, 46 (2005) (8): 2595–2602.

YOON J., CAI S., SUO Z. & HAYWARD R.C. Poroelastic swelling kinetics of thin hydrogel layers: comparison of theory and experiment. *Soft Matter*, 6 (2010) (23): 6004–6012.

YU C., MALAKPOOR K. & HUYGHE J. A mixed hybrid finite element framework for the simulation of swelling ionized hydrogels. *Computational Mechanics*, 63 (2019): 835–852.

YU Y., ZHANG Y., MARTIN J.A. & OZBOLAT I.T. Evaluation of cell viability and functionality in vessel-like bioprintable cell-laden tubular channels. *Journal of biomechanical engineering*, 135 (2013) (9).

ZHANG F., WEI M., VISWANATHAN V.V., SWART B. ET AL. 3d printing technologies for electrochemical energy storage. *Nano Energy*, 40 (2017): 418–431.

ZHANG H., ZHANG C., VAZIRI S., KENARANGI F. ET AL. Microfluidic ionic liquid dye laser. *IEEE Photonics Journal*, (2020).

ZHANG J., ZHAO X., SUO Z. & JIANG H. A finite element method for transient analysis of concurrent large deformation and mass transport in gels. *Journal of Applied Physics*, 105 (2009) (9): 093 522.

ZHANG Y., YU Y., AKKOUCH A., DABABNEH A. ET AL. In vitro study of directly bioprinted perfusable vasculature conduits. *Biomaterials science*, 3 (2015a) (1): 134–143.

ZHANG Y.N., AVERY R.K., VALLMAJO-MARTIN Q., ASSMANN A. ET AL. A highly elastic and rapidly crosslinkable elastin-like polypeptide-based hydrogel for biomedical applications. *Advanced functional materials*, 25 (2015b) (30): 4814–4826.

ZHANG Y.S., ARNERI A., BERSINI S., SHIN S.R. ET AL. Bioprinting 3d microfibrous scaffolds for engineering endothelialized myocardium and heart-on-a-chip. *Biomaterials*, 110 (2016): 45–59.

ZHAO G., WANG Z., ZHAO H. & YANG J. Bending force enhancement of sodium alginate-based polymer gel paper actuators. *Cellulose*, 26 (2019) (13-14): 7809–7822.

ZHAO Y. & EICHINGER B. Theoretical interpretation of the swelling of elastomers. *Macromolecules*, 25 (1992) (25): 6996–7002.

ZIENKIEWICZ O.C. & TAYLOR R.L. *The finite element method for solid and structural mechanics*. Elsevier, 2005.

ZIENKIEWICZ O.C., TAYLOR R.L., TAYLOR R.L. & TAYLOR R.L. *The finite element method: solid mechanics*, volume 2. Butterworth-heinemann, 2000.